ABSTRACT

ANALYSIS OF FAR-INFRARED OPTICAL SPECTRA OF MULTIFERROICS

by
Eric C. Standard

The optical spectra of multiferroic crystals $Dy_3Fe_5O_{12}$, $Tb_3Fe_5O_{12}$, and four hexagonal $RMnO_3$ (R = Er, Tm, Yb, Lu) are studied using intense bright synchrotonic light in the infrared spectral range. In regards to the materials analyzed, two rare earth iron garnets and four rare earth manganites in total are examined. These materials have attracted much attention due to their interesting magnetoelectric properties. They could serve as the basis for the next generation of faster and more energy efficient memory and logic devices. To examine these materials, two optical techniques were utilized: transmission spectroscopy and rotating analyzer ellipsometry. Transmission spectroscopy experiments analyze absorption of light passed through a material. Ellipsometry examines the change of polarization state for a reflected beam of light. Work has been done at the Brookhaven National Laboratory - National Synchrotron Light Source. Requisite for this project is a pair of broadband retarders for far-IR spectral range. Several retarders are devised to accomplish this task. They were designed using computer simulations and calculations before they are fabricated. Work towards the development of these retarders is included in this dissertation.

Ferrimagnetic $Dy_3Fe_5O_{12}$ single crystals are studied in the spectral range between 12 and 700 cm^{-1}, and in a wide temperature range between 5 K and 300 K using transmission spectroscopy and rotating analyzer ellipsometry (RAE). It is found that in the temperature range below T_C =16 K for the magnetic ordering of Dy^{3+} spins, a number of ligand field (LF) and Kaplan-Kittel (KK) exchange resonance modes emerge.

Temperature dependences of their frequencies allowed us to estimate the ratio between the Fe–Dy and Dy–Dy exchange constants.

$Tb_3Fe_5O_{12}$ single crystals are studied in the range between 15 and 100 cm^{-1}, in magnetic fields up to 10 T, and for temperatures between 5 and 150 K using only transmission spectroscopy. A number of IR active excitations are attributed to electric-dipole transitions between ligand-field splitting of Tb^{3+}. Anticrossing between the magnetic exchange excitation and the ligand-field transition occurs at the temperature between 60 and 80 K. The corresponding coupling energy for this interaction is 6 cm^{-1}. Temperature-induced softening of the hybrid IR excitation correlates with the increase of the static dielectric constant in $Tb_3Fe_5O_{12}$.

The hexagonal $RMnO_3$ (R = Er, Tm, Yb, Lu) single crystals are studied between 8 and 125 cm^{-1}, in fields up to 9T and for temperatures from 1.5 to 100 K. It is observed that the magnon frequency increases systematically with a decrease of the rare earth ion radius. The magnetic ordering of R ions (R=Er, Tm, Yb) is seen at low temperatures T<3.5 K and in strong external magnetic fields. The observed effects are analyzed taking into account main magnetic interactions in the system including exchange of the Mn^{3+} spins with R^{3+} paramagnetic moments.

ANALYSIS OF FAR-INFRARED OPTICAL SPECTRA OF MULTIFERROICS

by
Eric C. Standard

A Dissertation
Submitted to the Faculty of
New Jersey Institute of Technology
and Rutgers, The State University of New Jersey - Newark
in Partial Fulfillment of the Requirements for the Degree of
Doctor of Philosophy in Applied Physics

Federated Department of Physics

May 2014

APPROVAL PAGE

ANALYSIS OF FAR-INFRARED OPTICAL SPECTRA OF MULTIFERROICS
Eric C. Standard

Dr. Andrei A. Sirenko, Dissertation Advisor — Date
Professor and Department Chair of Applied Physics, NJIT

Dr. Michael Kotelyanskii, Committee Member — Date
Senior Member of Technical Staff, Rudolph Technologies, Inc.

Dr. John F. Federici, Committee Member — Date
Distinguished Professor of Applied Physics, NJIT

Dr. Martin Schaden, Committee Member — Date
Associate Professor of Applied Physics, Rutgers - Newark

Dr. Tao Zhou, Committee Member — Date
Associate Professor of Applied Physics, NJIT

Dr. Ken Ahn, Committee Member — Date
Assistant Professor of Applied Physics, NJIT

BIOGRAPHICAL SKETCH

Author: Eric C. Standard

Degree: Doctor of Philosophy

Date: January 2014

Undergraduate and Graduate Education:

- Doctor of Philosophy in Applied Physics,
  New Jersey Institute of Technology, Newark, NJ, 2014

- Master of Science in Applied Physics,
  New Jersey Institute of Technology, Newark, NJ, 2011

- Bachelor of Arts in Applied Physics,
  Rutgers, The State University of New Jersey - Newark, NJ, 2009

Major: Applied Physics

Presentations and Publications:

T. N. Stanislavchuk, T. D. Kang, P. D. Rogers, E. C. Standard, R. Basistyy, A. M. Kotelyanskii, G. Nita, T. Zhou, G. L. Carr, M. Kotelyanskii, and A. A. Sirenko, "Synchrotron radiation-based far-infrared spectroscopic ellipsometer with full Mueller-matrix capability", Rev. Sci. Instrum. **84**, 023901 (2013).

T. D. Kang, E. C. Standard, P. D. Rogers, K. H. Ahn, and A. A. Sirenko, A. Dubroka, C. Bernhard, S. Park, Y. J. Choi and S.-W. Cheong, "Far-infrared spectra of the magnetic exchange resonances and optical phonons and their connection to magnetic and dielectric properties of $Dy_3Fe_5O_{12}$ garnet", Phys. Rev. B **86**, 144112 (2012).

E. C. Standard, T. Stanislavchuk, A.A. Sirenko, N. Lee and S.-W. Cheong "Magnons and Crystal-field transitions in hexagonal RMnO3 (R = Er, Tm, Yb, Lu) single crystals" Phys. Rev. B **85,** 144422 (2012).

E. C. Standard, T. Stanislavchuk, R. Basistyy, A.A. Sirenko, T.D. Kang, N. Lee and S.-W. Cheong "Magnons and Crystal-field transitions in hexagonal RMnO3" American Physical Society (APS) March Meeting, Boston, Mass. (2012).

P. D. Rogers, Y. J. Choi, E. C. Standard, T. D. Kang, K. H. Ahn, A. Dubroka, P. Marsik, Ch. Wang, C. Bernhard, S. Park, S.-W. Cheong, M. Kotelyanskii, and A. A. Sirenko, "Adjusted oscillator strength matching for hybrid magnetic and electric excitations in $Dy_3Fe_5O_{12}$ garnet", Phys. Rev. B **83**, 174407 (2011).

T. D. Kang, E. Standard, G. L. Carr, T. Zhou, M. Kotelyanskii, and A. A. Sirenko, "Rotatable broadband retarders for far-infrared spectroscopic ellipsometry", Thin Solid Films, **519**, 2698 (2011).

T. D. Kang, E. Standard, K. H. Ahn, and A. A. Sirenko, G. L. Carr, S. Park, Y. J. Choi, M. Ramazanoglu, V. Kiryukhin, and S-W. Cheong, "Coupling between magnon and ligand-field excitations in magnetoelectric $Tb_3Fe_5O_{12}$ garnet", Phys. Rev. B **82**, 014414 (2010).

Ora et Labora

ACKNOWLEDGEMENTS

I would like to thank my advisor Dr. Andrei Sirenko for the supervision and care he has given me through my academic career and research pursuits. Dr. Sirenko has spent many long hours and has been extraordinarily patient in mentoring me in modern solid state physics. I first met Dr. Sirenko while taking his solid state physics class as an undergraduate. I was returning to school after a three year hiatus. I needed a single lab credit to graduate but planned to continue on to graduate school. Therefore, I took Dr. Sirenko's class as an unnecessary elective in order to acclimate back to school. Inexplicably he pulled me aside after class one day and asked my intentions after graduation. I told him I dreamed of getting a doctorate in physics. Since that day, every positive stride I have made towards my doctorate is solely due to his guidance. Mere words fail to express the gratitude I have towards Dr. Sirenko. He made my dreams come true.

I would like to thank Michael Kotelyanskii who lead the project on the theory of ellipsometry and for helping me grow in my career. I would like to thanks Dr. T. D. Kang who was the first post-doc working with our research team. He has served as an great inspiration to me during his time with the ellipsometry project. The second post-doc with the research team is a young man of exceptionable talent and intellectual gifts named Dr. Taras Stanislavchuk. Likewise, I would like to thank him for the encouragement he has given me. Kang and Taras have shown me the devotion that true excellence requires. I would like to thank Dr. G. Larry Carr for his assistance at NSLS. Our beamline would fall apart without Dr. Carr. Larry was a born teacher and used every question as an opportunity to elucidate some esoteric topics of physics.

Deserving of much recognition are N. Lee, S. Park, Y. J. Choi, S.-W. Cheong and the entire Rutgers team for the multiferroic crystals used through this dissertation. Without them there would be no measurements.

I would like to thank my friends and fellow graduate students, some finished and some still studying, at NJIT: Dr. Sean O'Malley, Dr. Paul Rodgers, Kwok (Phil) Lo, and Roman Basistyy. We all shared more than a laboratory in the basement of Tiernan hall, but we shared a love of discovery and an optimism of the future.

There are several teachers at NJIT I would like to thank. Advanced education is a challenging business. NJIT should take enormous pride that they have many instructors who can turn their bland subject into topics of wonder and awe. Thank you so very much Dr. Ken Chin, Dr. Andrew Gerrard, Dr. Libarid Maljian, Dr. Nuggehalli M. Ravindra, Dr. Vitaly Shneidman, and Dr. Haimin Wang.

I would like to thank my family. They are my bedrock of love and support. I would like to thank my father, Ernest; my mother, Kathleen; my stepfather, Jim; and my stepmother, Myong. My father always fostered my interest in science. He never denied me any opportunity or object to aid my curiosity. My mother and stepfather who both love me and have pushed me to succeed, especially my mother who indulged my home science projects when I was a child. My stepmother's food kept me going during the long nights of studying. I would like to thank my brothers, Joseph and Jason, although they perpetually challenge me, they have always believed in me. I would also like to thank the love of my life, Jill.

TABLE OF CONTENTS

TABLE OF CONTENTS
(Continued)

TABLE OF CONTENTS
(Continued)

LIST OF TABLES

LIST OF FIGURES

LIST OF FIGURES
(Continued)

LIST OF FIGURES
(Continued)

LIST OF FIGURES
(Continued)

LIST OF FIGURES
(Continued)

LIST OF FIGURES
(Continued)

LIST OF FIGURES
(Continued)

LIST OF FIGURES
(Continued)

LIST OF FIGURES
(Continued)

LIST OF FIGURES
(Continued)

Figure **Page**

CHAPTER 1

INTRODUCTION

1.1 Introductory Remarks

This dissertation describes optical studies set of rare earth iron garnets ($R_3Fe_5O_{12}$ R= Tb, Dy) and hexagonal rare earth manganites ($R$$MnO_3$ R= Er, Tm, Yb, Lu). Multiferroics are interesting because of strong coupling between their electric and magnetic properties. These material are promising for new technological advancements. The facility at the Brookhaven National Laboratory - National Synchrotron Light Source provides an excellent place to conduct experiments. With its intense bright light source, materials can be probed in a wide range of the infrared spectrum using spectroscopic transmission or ellipsometry techniques.

Spectroscopy is a very useful technique for investigation of various types of materials including multiferroics. Information on the material is encoded in modification of the radiation spectrum due to interaction with the material. The extensive spectral range covered by synchrotron radiation allows us to study electronic, magnetic and lattice properties. Lattice vibrations (i.e., phonons) interact with electromagnetic radiation at far infrared frequencies. Electronic transitions across the energy gap of multiferroics happen in the visible part of the spectrum around 2eV and above. Thus, optical studies in this frequency range provide an important tool for investigating multiferroics.

A synchrotron is a source of high brightness electromagnetic radiation emitted from electrons orbiting around a closed path of a storage ring. It is a very broad band source, extending from the very far infrared to the hard x-ray. Beamline U4IR on the VUV ring at the National Synchrotron Light Source (NSLS) of Brookhaven National Laboratory (BNL) is dedicated to solid-state physics experiments in the spectral range between 10 and 4000 cm^{-1}.

1.2 Organization

The overall structure of this thesis is the following: background (Chapters 2 & 3), experimental methods and sample properties (Chapters 4 & 5), experimental results (Chapters 6 - 8). Specifically, Chapter 2 presents a review of a basic theory of optical properties. It lays down the mathematical frame work of the electromagnetic wave and it's interaction with matter. Polarization is discussed in Chapter 3 with empathize on the Jones and Stokes representation of the polarized state. Chapter 4 summarizes the basic understanding of spectroscopic ellipsometry, synchrotron radiation, and transmission experiments. Chapter 5 is a review of multiferroics, the history of their discovery, theory, and properties. Chapter 6 focuses on the development of the rotatable broadband retarders used in full Mueller matrix ellipsometry. Chapter 7 explores the transmission and ellipsometry data for dysprosium and terbium iron garnets. Finally, Chapter 8 examines at the transmission spectra of hexagonal rare earth manganites ($RMnO_3$ R= Er, Tm, Yb, Lu) and how the magnon frequency changes with the rare earth ionic radius.

In optical studies, different energy units are quite common for the different techniques, frequency ranges, and disciplines. In the infrared spectral region, the most commonly used unit is the wavenumber given by cm^{-1}. It is defined as the frequency in Hz divided by the speed of light in cm/s or the reciprocal of the wavelength in cm.

CHAPTER 2

OPTICS

2.1 Introduction

This chapter will provide a general background of the theory of light. The chapter begins with an introductory discussion of Maxwell's equations. Then equations of plane electromagnetic waves are shown. Fresnel's equations for reflection and transmission are given. Also a brief section on magnetoelectric couplings along with a section of the Lorentz oscillator model. The main purpose of the chapter is to present a basic electromagnetic theory and mathematical background for the remaining chapters.

Due mainly to the talent of James Clerk Maxwell, humanity knows that light is an electromagnetic wave. Light, as people know it, is a small portion of the much larger electromagnetic spectrum. The visible light, which humans see, has wavelength approximately between 400 to 750 nm. Ultraviolet and infrared are the two nearest neighbors to visible light. William Herschel discovered infrared radiation in sunlight. Infrared has wavelengths in the range 750 nm to 1 mm. Victor Schumann was the first to probe the ultraviolet region by using a fluorite lens. Ultraviolet has shorter wavelengths than visible light, generally accepted to be from 10 to 400 nm. Next to infrared spectrum are radio waves. Radio waves can have wavelengths from 1 mm to 100,000 km. Microwaves are radio waves with the range between 1 mm to 1 m. Adjacent to the ultraviolet region are the energetic x-rays and gamma-rays. X-rays have wavelengths 0.01 to 10 nm. Gamma-rays have wavelengths of 0.02 nm or less. [1]

2.2 Maxwell's Equations

Light, as previously stated, is an electromagnetic wave. Its properties are described by a set of four equations, known as Maxwell's equation. Maxwell's theory explains nearly all optical phenomena, except absorption and emission which are covered by quantum mechanics. His equations summarize the four basic laws of classical electrodynamics and can viewed either in free space or in matter with charges and currents:

Free Space	Matter	
$\nabla \cdot \boldsymbol{E} = \frac{\rho}{\varepsilon_0}$	$\nabla \cdot \boldsymbol{D} = \rho_f$	(2.1)
$\nabla \cdot \boldsymbol{B} = 0$	$\nabla \cdot \boldsymbol{B} = 0$	(2.2)
$\nabla \times \boldsymbol{E} = -\frac{\partial \boldsymbol{B}}{\partial t}$	$\nabla \times \boldsymbol{E} = -\frac{\partial \boldsymbol{B}}{\partial t}$	(2.3)
$\nabla \times \boldsymbol{B} = \mu_0 \boldsymbol{J} + \mu_0 \varepsilon_0 \frac{\partial \boldsymbol{E}}{\partial t}$	$\nabla \times \boldsymbol{H} = \boldsymbol{J}_f + \frac{\partial \boldsymbol{D}}{\partial t}$	(2.4)

where $\boldsymbol{E}$ and $\boldsymbol{B}$ are respectively the electric and magnetic field vectors, ρ_f is the free charge density, and $\boldsymbol{J}_f$ is the free current density. Vectors fields $\boldsymbol{D}$ and $\boldsymbol{H}$ are respectively the electric displacement and auxiliary magnetic field. Equations 2.1and 2.2 are the differential forms of Gauss's law for electric and magnetic fields. Equation 2.2 has the implication that magnetic monopoles do not exist. Equation 2.3 is Faraday's induction law. Lastly, Equation 2.4 is Ampere's Law. These equations hold for time varying fields such as the electric and magnetic fields, which constitute an electromagnetic wave. The electromagnetic properties of a medium described by the macroscopic polarization $\boldsymbol{P}$ and magnetization $\boldsymbol{M}$, are linked to vectors $\boldsymbol{E}$, $\boldsymbol{D}$, $\boldsymbol{H}$, and $\boldsymbol{B}$.

$$\boldsymbol{D} = \varepsilon_0 \boldsymbol{E} + \boldsymbol{P} \tag{2.5}$$

$$\boldsymbol{H} = \frac{\boldsymbol{B}}{\mu_0} - \boldsymbol{M} \tag{2.6}$$

Under the influence of external fields, the behavior of non-dispersive, isotropic, continuous matter is simply described by a series of Equations 2.7 - 2.11.

$$\boldsymbol{J} = \sigma \boldsymbol{E} \tag{2.7}$$

$$\boldsymbol{D} = \varepsilon \boldsymbol{E} \tag{2.8}$$

$$\boldsymbol{B} = \mu \boldsymbol{H} \tag{2.9}$$

$$\boldsymbol{P} = \varepsilon_0 \chi_e \boldsymbol{E} \tag{2.10}$$

$$\boldsymbol{M} = \chi_m \boldsymbol{H} \tag{2.11}$$

The electric permittivity (ε_0) and the magnetic permeability (μ_0) of free space are

$$\varepsilon_0 = 8.85 \times 10^{-12} \frac{C^2}{N \cdot m^2} \tag{2.12}$$

$$\mu_0 = 4\pi \times 10^{-7} \frac{N \cdot s^2}{C^2} \tag{2.13}$$

The electric and magnetic susceptibilities are χ_e and χ_m are defined as follows,

$$\varepsilon = \varepsilon_0 (1 + \chi_e) \tag{2.14}$$

$$\mu = \mu_0 (1 + \chi_m) \tag{2.15}$$

The relative permittivity ε_r is also known as the dielectric constant. For non-magnetic materials $\mu_r = 1$. In this case $\mu = \mu_0$.

$$\varepsilon = \varepsilon_r \varepsilon_0 \tag{2.16}$$

$$\mu = \mu_r \mu_0 \tag{2.17}$$

In an isotropic homogenous medium the properties at each point are independent of direction. Therefore, ε, μ, and σ are scalars in such a medium. For anisotropic materials, their values in Equations 2.8 thru 2.11 are replaced by tensors. The four equations can then be used to express anisotropic materials. If the material parameters are

functions of frequency, then it exhibits temporal dispersion, such as $\varepsilon(\omega)$ and $\mu(\omega)$. [2] Anisotropic and magnetoelectric materials require matrix representation. The tensor forms of permittivity and permeability are the following:

$$\hat{\varepsilon} = \begin{pmatrix} \varepsilon_{xx} & \varepsilon_{xy} & \varepsilon_{xz} \\ \varepsilon_{yx} & \varepsilon_{yy} & \varepsilon_{yz} \\ \varepsilon_{zx} & \varepsilon_{zy} & \varepsilon_{zz} \end{pmatrix} \tag{2.18}$$

$$\hat{\mu} = \begin{pmatrix} \mu_{xx} & \mu_{xy} & \mu_{xz} \\ \mu_{yx} & \mu_{yy} & \mu_{yz} \\ \mu_{zx} & \mu_{zy} & \mu_{zz} \end{pmatrix} \tag{2.19}$$

Then in the displacement vector equation $\boldsymbol{D} = \varepsilon_0(1 + \chi_e)\boldsymbol{E}$ the 1 is unit matrix. In keeping with the matrix forms, Equation 2.14 truly represents not a dielectric constant but a dielectric tensor. The dependence of $\boldsymbol{D}$ on $\boldsymbol{E}$ is expressible as a tensor relation

$$\begin{pmatrix} D_x \\ D_y \\ D_z \end{pmatrix} = \begin{pmatrix} \varepsilon_{xx} & \varepsilon_{xy} & \varepsilon_{xz} \\ \varepsilon_{yx} & \varepsilon_{yy} & \varepsilon_{yz} \\ \varepsilon_{zx} & \varepsilon_{zy} & \varepsilon_{zz} \end{pmatrix} \begin{pmatrix} E_x \\ E_y \\ E_z \end{pmatrix} \tag{2.20}$$

The above equations are symmetric and therefore can always be diagonalized. Diagonalization turns the off diagonal elements to zero and reveals the three principal axes. The diagonal elements are called the principal permittivities or permeabilities.

$$\hat{\varepsilon} = \begin{pmatrix} \varepsilon_{xx} & 0 & 0 \\ 0 & \varepsilon_{yy} & 0 \\ 0 & 0 & \varepsilon_{zz} \end{pmatrix} \tag{2.21}$$

$$\hat{\mu} = \begin{pmatrix} \mu_{xx} & 0 & 0 \\ 0 & \mu_{yy} & 0 \\ 0 & 0 & \mu_{zz} \end{pmatrix} \tag{2.22}$$

Further if the material is isotropic the diagonal elements are equal: $\varepsilon_{zz} = \varepsilon_{yy} = \varepsilon_{zz}$ or $\mu_{zz} = \mu_{yy} = \mu_{zz}$. [3]

2.3 Electromagnetic Waves

In the case of propagation through a vacuum, the four Maxwell Equations can be combined to produce the following two equations for the electric and magnetic fields.

$$\nabla^2 \boldsymbol{E} = \varepsilon_0 \mu_0 \frac{\partial^2 \boldsymbol{E}}{\partial t^2} \tag{2.23}$$

$$\nabla^2 \boldsymbol{B} = \varepsilon_0 \mu_0 \frac{\partial^2 \boldsymbol{B}}{\partial t^2} \tag{2.24}$$

These Equations have the same form as the wave equation. Therefore the electric and magnetic fields must oscillate like a wave when in motion. The basic solution for Equations 2.24 and 2.25 is a sinusoidal wave traveling in a rectilinear direction. By direct comparison with the wave equation, the speed of light in a vacuum can be found. It is a fundamental constant with the value $c = 299{,}792{,}458\,\frac{m}{s}$. In a vacuum $v = c$.

$$\frac{1}{v^2} = \varepsilon_0 \mu_0 \tag{2.25}$$

$$v = \frac{1}{\sqrt{\varepsilon_0 \mu_0}} = 2.998 \times 10^8\,\frac{m}{s} \tag{2.26}$$

Light is a three-dimensional electromagnetic wave with many different propagating waveforms. It is easiest to consider a monochromatic plane wave of angular frequency ω. The time dependence can be written in the form $\exp(-i\omega t)$. With this time variation, the field components still satisfy the wave equations. Since Maxwell's equations unify the individual electric and magnetic field into one combined electromagnetic field, only one of these equations needs to be solved. The basic equation which describes a plane electromagnetic wave is,

$$\boldsymbol{E}(\boldsymbol{r}, t) = \boldsymbol{E}_0 e^{-i(\omega t - \boldsymbol{k}\cdot\boldsymbol{r} + \phi_0)} \tag{2.27}$$

In the above Equation 2.28 four components need to be discussed. The maximum amplitude of the wave is $\boldsymbol{E}_0$. The angular frequency is ω. It is related to the ordinary frequency f by the following equation

$$\omega = 2\pi f \tag{2.28}$$

The wave vector $\boldsymbol{k}$ is an important value as it defines the direction of propagation.

$$\boldsymbol{k} = k_x\hat{\boldsymbol{\imath}} + k_y\hat{\boldsymbol{\jmath}} + k_z\hat{\boldsymbol{k}} \tag{2.29}$$

$$k = |\boldsymbol{k}| = \sqrt{k_x^2 + k_y^2 + k_z^2} \tag{2.30}$$

The wave vector is related to the wave length by

$$\lambda = \frac{2\pi}{k} \tag{2.31}$$

Lastly the value $\phi_0$is just the initial phase constant. [2]

2.4 Reflection and Transmission

When light is reflected or transmitted by samples at oblique incidence, the light is classified into p and s-polarized light waves depending on the oscillatory direction of its electric field. Each light wave shows quite different behavior. In p polarization, the electric fields of incident and reflected light waves oscillate within the same plane. The p in this case means parallel to the plane. This particular plane is called the plane of incidence.

The most important equation when considering reflection and transmission is Snell's Law. It governs refraction of light from one medium into another,

$$n_1 \sin\theta_1 = n_2 \sin\theta_2 \tag{2.32}$$

The reflection and transmission are defined as a ratio of their wave amplitudes to the incident wave's amplitude. For normal incidence, both p and s polarizations have the same form of reflection and transmission coefficients:

$$r = \frac{E_r}{E_i} = \frac{n_1 - n_2}{n_1 + n_2}, \tag{2.33}$$

$$t = \frac{E_t}{E_i} = 1 + r = \frac{2n_1}{n_1 + n_2}. \tag{2.34}$$

When the angle of incidence is not normal, then the Fresnel reflection coefficients are the following,

$$r_p = \frac{n_1 \cos(\theta_2) - n_2 \cos(\theta_1)}{n_1 \cos(\theta_2) + n_2 \cos(\theta_1)}, \tag{2.35}$$

$$r_s = \frac{n_1 \cos(\theta_1) - n_2 \cos(\theta_2)}{n_1 \cos(\theta_1) + n_2 \cos(\theta_2)}. \tag{2.36}$$

They can be combined with Snell's equation to produce,

$$r_p = \frac{\sqrt{\left(\frac{n_2}{n_1}\right)^2 - \sin^2\theta} - \left(\frac{n_2}{n_1}\right)^2 \cos\theta}{\sqrt{\left(\frac{n_2}{n_1}\right)^2 - \sin^2\theta} + \left(\frac{n_2}{n_1}\right)^2 \cos\theta}, \tag{2.37}$$

$$r_s = \frac{\cos\theta - \sqrt{\left(\frac{n_2}{n_1}\right)^2 - \sin^2\theta}}{\cos\theta + \sqrt{\left(\frac{n_2}{n_1}\right)^2 - \sin^2\theta}}. \tag{2.38}$$

If light moves from a dense material into a less dense material, there is a maximum angle of incidence after which all light will be reflected. This effect is called total internal reflection. The maximum angle is called the critical angle θ_c and it comes from Snell's equation. Assuming that $n_2 > n_1$ the angle would appear when the refracted ray reached 90°, then the sine function is equal to one and

$$\sin\theta_c = \frac{n_1}{n_2}. \tag{2.39}$$

With this new definition, Equations 2.32 and 2.33 can be rewritten into

$$r_p = \frac{\sqrt{\sin^2\theta_c - \sin^2\theta} - \sin^2\theta_c \cos\theta}{\sqrt{\sin^2\theta_c - \sin^2\theta} + \sin^2\theta_c \cos\theta} \tag{2.40}$$

$$r_s = \frac{\cos\theta - \sqrt{\sin^2\theta_c - \sin^2\theta}}{\cos\theta + \sqrt{\sin^2\theta_c - \sin^2\theta}}. \tag{2.41}$$

At angles of incidence above the critical angle, Equations 2.35 and 2.36 are complex numbers as the quantity under the radical becomes negative. This introduces a phase shift δ between the p and s polarizations.

$$\tan\left(\frac{\delta}{2}\right) = \frac{\sqrt{\sin^2\theta - n^{-2}}}{\sin\theta\tan\theta} \tag{2.42}$$

Here it is assumed that the less optically dense material is air with refractive index equal to one. The refractive index in Equation 2.43 is of the dense material. [3]

Veselago published his monumental work in 1967, "The electrodynamics of substances with simultaneously negative values of ε and μ" [4]. In this seminal work, he prescribed a formula for dealing with materials with positive and negative values of permittivity and permeability. The starting point is Fresnel's equation presented above. Fresnel had made the assumption that $n \to \sqrt{\varepsilon}$ for nonmagnetic materials. Veselago realized that for reflection the index of refraction should be $n(\omega) \to \sqrt{\varepsilon(\omega)/\mu(\omega)}$. Also for transmission the index of refraction needs to be replaced with $n(\omega) \to \sqrt{\varepsilon(\omega)\cdot\mu(\omega)}$. [4]

2.5 Lorentz Model

In solids there are a variety of excitations that add to the dielectric function, and therefore, the material' s optical properties. The contribution are frequency dependent.

$$\varepsilon_r(\omega) = 1 + \chi_{el}(\omega) + \chi_{ph}(\omega) + \chi_{CF}(\omega) \quad 2.43$$

For example the electron contribution to the susceptibility is derived in the following way. $\boldsymbol{P}$ is the polarization of the material. It is a vector, having both directionality and magnitude. It is defined as the dipole moment per unit volume.

$$\boldsymbol{P} = \varepsilon_0 \chi_{el} \boldsymbol{E} = N\boldsymbol{d} = N q_e \boldsymbol{x} \quad 2.44$$

The first part of the above equation is the familiar definition of polarization given in Section 2.2. The next expression contains N, which is the number of dipoles, and the vector $\boldsymbol{d}$, which is the dipole moment per atom. The third expression of polarization is the expanded form of the individual dipole moment. In this way q_e is amount of charge that separated by distance $\boldsymbol{x}$.

From Newton's Second Law, the following can be written.

$$m_e \frac{d^2\boldsymbol{x}}{dt^2} = -m_e \omega_0^2 \boldsymbol{x} - m_e \gamma \frac{d\boldsymbol{x}}{dt} + q_e \boldsymbol{E}_0 e^{-i\omega t} \quad 2.45$$

This equation has the same form as a damped driven oscillator, which has the following solution,

$$\boldsymbol{x} = \frac{q_e}{m_e} \frac{\boldsymbol{E}_0}{(\omega_o^2 - \omega^2 - i\omega\gamma)}. \quad 2.46$$

Comparing this last expression with Equation 2.44 it is seen that the valence electron's contribution to the susceptibility is just

$$\chi_{el}(\omega) = \frac{N q_e^2}{\varepsilon_0 m_e} \frac{1}{(\omega_0^2 - \omega^2 - i\omega\gamma)} = \sum_j \frac{P_j^2}{\omega_0^2 - \omega^2 - i\omega\gamma}. \quad 2.47$$

The dielectric function is generally described as the sum of different oscillators, which can be written as a sigma sum, and the subscript j denotes the j^{th} oscillator. Also P_j is called the oscillator strength or spectral weight. In the far-IR the valence electron contribution to susceptibility is frequency independent and can be often combined with one to form ε_∞, the high frequency dielectric constant. [5]

2.6 Magnetoelectric Phenomena

It had been long thought that a material's magnetic and electric properties were isolated from each other. Lifshitz and Landau were two of the first to theorize how a coupling could exists. There work was done in the 1950's and published in their famous set of textbooks on theoretical physics. [6] Dzyaloshinskii derived the form of linear magnetoelectric coupling in Cr_2O_3. He defined a new set of constitutive relations which include contribution from both electric and magnetic fields.

$$\boldsymbol{D} = \hat{\varepsilon}\boldsymbol{E} + \hat{\alpha}\boldsymbol{H} \tag{2.48}$$

$$\boldsymbol{B} = \hat{\alpha}'\boldsymbol{E} + \hat{\mu}\boldsymbol{H} \tag{2.49}$$

In the Equations 2.44 and 2.45, the variables $\hat{\alpha}$ and $\hat{\alpha}'$ are the magnetoelectric tensor and it's transpose. [7] Berreman developed a 4x4 matrix formalism to obtain numeric and sometimes analytic solutions for the propagation of electromagnetic waves in magnetoelectric materials. The complete description of the wave is made possible using his matrix equation,

$$\begin{pmatrix} 0 & -curl \\ curl & 0 \end{pmatrix}\begin{pmatrix} \boldsymbol{E} \\ \boldsymbol{H} \end{pmatrix} = i\frac{\omega}{c}\begin{pmatrix} \hat{\varepsilon} & \hat{\alpha} \\ \hat{\alpha}' & \mu \end{pmatrix}\begin{pmatrix} \boldsymbol{E} \\ \boldsymbol{H} \end{pmatrix} \tag{2.50}$$

The complexity of the above equation is hidden in its compactness. The curl in the leftmost matrix is really a 3x3 matrix, the two diagonal zeroes are likewise 3x3 matrices

filled with zeroes. Thus, the first matrix really has 6x6 elements. The second matrix on left side of the equal sign has six vertical elements. They are $E_x, E_y, E_z, H_x, H_y, H_z$. Again the seemly 2x2 matrix of the right side truly has 6x6 elements since the permittivity, permeability, and magnetoelectric tensor and its transpose are 3x3 matrices each. Berreman formulized a way to reduce the 6x6 matrix to a 4x4 matrix. His equation for wave propagation is the following,

$$\frac{d\boldsymbol{\Psi}}{dt} = i\frac{\omega}{c}\widetilde{\Delta}\boldsymbol{\Psi} \tag{2.51}$$

The term $\boldsymbol{\Psi}$ contains the transverse electric and auxiliary magnet fields, $\left[E_x, H_y, E_y, -H_x\right]^T$. The eigenvalues and eigenvectors of Berreman's equation lead to the wave vectors and transverse components of propagation. [8]

The Free Energy for the magnetoelectric system is,

$$-F(E,H) = \frac{1}{2}\,\varepsilon_0\varepsilon_{ij}E_iE_j + \frac{1}{2}\mu_0\mu_{ij}H_iH_j + \alpha_{ij}E_iH_j + \frac{1}{2}\,\beta_{ijk}E_iH_jH_k + \frac{1}{2}\,\gamma_{ijk}H_iE_jE_k \tag{2.52}$$

The term α_{ij} is the linear magnetoelectric coupling tensor. The other terms β_{ijk} and γ_{ijk} are for higher order magnetoelectric effects. Taking a derivative of the Free Energy with respect either auxiliary magnetic or electric fields will yield the polarization and magnetization, respectively. The following equation can be derived from Equation 2.48 by forcing the linear terms to be greater than zero. [9]

$$\alpha_{ij}^2 \leq \varepsilon_0\mu_0\varepsilon_{ij}\mu_{ij} \tag{2.48}$$

$$\alpha(\omega)\alpha'(\omega) \leq \varepsilon(\omega)\mu(\omega) \tag{2.49}$$

CHAPTER 3

POLARIZATION

3.1 Historical Background

The history of Man's discovery of polarized light is very interesting. Because humans lack polarization sensitive eyes, the effect was not obvious to people. The earliest observations of polarization effects come from the birefringence of light through crystals, particularly calcite $CaCo_3$. Christiaan Hyugens is considered to have discovered polarized light. He was the first to show that there is an essential difference between the two refracted rays. His experiments involved the passing light through two calcite crystals keeping the first one steady and rotating the second. His findings were published in 1678's *Traite de la lumiére*.

Augustin Fresnel made several major contributions to understanding the polarization phenomena. Fresnel theorized that the waves were transverse waves. This idea conflicted with notion of a fluid ether which was popular at the time. Transverse waves cannot propagate in a gas or a liquid because there is no mechanism for the driving motion perpendicular to the propagation of the wave. In spite of this, Fresnel was able to explain many of the polarization manifestations with his theory. This includes double refraction, chromatic polarization, interference of polarized light, and Malus's cosine-squared law. He wrote about his work in *Mémoire sur la réflexion de la lumiére polarisée* published in 1866. With his equations, he was able to explain not only the phenomena but also acquire numeric results.

George Gabriel Stokes developed a description of polarized light using four numbers. He showed that any polarization state, even unpolarized light, could be described by a four component Stokes vector. He published his formalism in 1852. Henri Poincaré was one of the greatest minds of his time. He left a lasting imprint in many fields of study both scientific and mathematical. In regards to polarization, Poincaré developed the idea that all polarization state could be thought of as points on the surface of a sphere. Circular polarizations inhabit the poles of the sphere. Linear polarization lie entirely on the equator of the Poincaré sphere. The various angles that linear polarization may be rotated correspond to the longitudinal angle of the state on the sphere. Poincaré's work was published in his book *Théorie mathématique da la lumiére* in 1892. During the twentieth century, much of the work on polarization was to develop it as a tool for further investigations in optics and material science. Polarimeters and ellipsometers became common devices to determine the polarization states of light reflected from a sample. To aid in analysis of polarization and optical components, R. Clark Jones developed a new calculus for the treatment of optical systems. He did this with a series of eight papers published between 1941 and 1955. [10]

3.2 Representation of Polarized Light

All light has the characteristic of perpendicular electric and magnetic fields. Since the magnetic field is linked to the electric fields and vice versa, analysis need only consider one. If a beam of light travels in the $\hat{\boldsymbol{z}}$ direction, the electric field can be decomposed in to its x and y components. In a right hand Cartesian system, a plane harmonic wave of

angular frequency ω traveling at speed c in the $\hat{\boldsymbol{z}}$ direction has two field components $E_x(z,t)$ and $E_y(z,t)$:

$$E_x(z,t) = E_{0x}\ \cos\left[\omega t - \vec{k}\cdot\hat{\boldsymbol{z}} + \ \delta_x\right] \tag{3.1}$$

$$E_y(z,t) = E_{0y}\ \cos\left[\omega t - \vec{k}\cdot\hat{\boldsymbol{z}} + \ \delta_y\right] \tag{3.2}$$

where E_{0x}, E_{0y} are the wave amplitudes and δ_x, δ_y are arbitrary phases of the waves. The phase difference between two components can be defined as [11]

$$\delta = \ \delta_x - \delta_y \qquad 0 \le \delta \le 2\pi \tag{3.3}$$

Table 3.1 Electric Fields and Phase Difference for Various Polarization States

Type	Field Condition	Phase Condition
Linear Horizontal Polarization (LHP)	$E_{0y} = 0$	any
Linear Vertical Polarization (LVP)	$E_{0x} = 0$	any
Linear +45° Polarization ($L_{+45°}P$)	$E_{0x} = \ E_{0y} = \ E_0$	$\delta = 0$
Linear -45° Polarization ($L_{-45°}P$)	$E_{0x} = \ E_{0y} = \ E_0$	$\delta = \pi$
Right Circular Polarization (RCP)	$E_{0x} = \ E_{0y} = \ E_0$	$\delta = \frac{\pi}{2}$
Left Circular Polarization (LCP)	$E_{0x} = \ E_{0y} = \ E_0$	$\delta = \frac{3\pi}{2}$

Source: [11]

3.3 Optical Elements

3.3.1 Linear Polarizer

A linear polarizer, also called an analyzer, is a device that creates linear polarized light from an arbitrary input. The linear polarizer removes the orthogonal components of the

incident light. The transmission axis of a linear polarizer is defined with respect to an incoming beam of linear polarized light that is normal to the face of the polarizer. The direction of the transmittance axis is the same as the electric field vector which would allow maximum transmittance of light.

3.3.2 Retarder

A circular retarder is one method to convert linearly polarized light into circularly or elliptically polarized light. It is designed such that a 90° or 270° phase shift occurs as the result of internal reflections. The phase shifts can be calculated using Equation 2.42. Also called Fresnel rhombs these type of circular polarizers have advantages over wave plates. The slow varying rhomb dispersion means that the retardance change as a function of wavelength is small, thereby creating broadband devices with long range stable retardance. [5], [12].

3.4 Jones Matrix

The mathematical description of optical measurements created by R.C. Jones is presented below. Even if many optical components are used in the system, the Jones matrix can be used to express the change of polarization state. The Jones matrix can also be used to express ellipsometric measurements.

The polarization state of light is expressed as the superposition of two waves oscillating parallel to the x and y axes. The Jones vector created by these two oscillating fields is expressed by

$$E(z,t) = \begin{bmatrix} E_{0x}\exp\{i(\omega t + \delta_x - kz)\} \\ E_{0y}\exp\{i(\omega t + \delta_y - kz)\} \end{bmatrix} = \exp\{i(\omega t - kz\} \begin{bmatrix} E_{0x}e^{i\delta_x} \\ E_{0y}e^{i\delta_y} \end{bmatrix} \quad (3.4)$$

For purposes of analysis, the oscillating term may be omitted from the last part. Therefore, all that remains is

$$E(z,t) = \begin{bmatrix} E_{0x}e^{i\delta_x} \\ E_{0y}e^{i\delta_y} \end{bmatrix} = \begin{bmatrix} E_x \\ E_y \end{bmatrix}. \quad (3.5)$$

where

$$E_x = E_{0x}\exp(i\delta_x) = |E_x|\exp(i\delta_x) \quad (3.6)$$

$$E_y = E_{0y}\exp(i\delta_y) = |E_y|\exp(i\delta_y) \quad (3.7)$$

The phase difference δ may be used to rewrite previous equations into

$$E_x = E_{0x}\exp(i(\delta_x - \delta_y)) = |E_x|\exp(-i\delta) \quad (3.8)$$

$$E_y = E_{0y} = |E_y| \quad (3.9)$$

The intensity is defined as

$$I = I_x^2 + I_y^2 = E_{0x}^2 + E_{0y}^2 = |E_x|^2 + |E_y|^2 = E_x E_x^* + E_y E_y^* \quad (3.10)$$

Conventional optical measurements including ellipsometry only take into consideration the relative changes in amplitude and phase. Therefore, the Jones vector is generally expressed with a normalized intensity $I = 1$. The transformation of the Jones vector is described by Jones 2 x 2 matrix $\boldsymbol{J}$:

$$E_{out} = \boldsymbol{J}E_{in} \quad (3.11)$$

or in a matrix form,

$$\begin{bmatrix} E_x \\ E_y \end{bmatrix} = \begin{bmatrix} J_{11} & J_{12} \\ J_{21} & J_{22} \end{bmatrix} \begin{bmatrix} E_{0x} \\ E_{0y} \end{bmatrix} \quad (3.12)$$

See Table 3.3 for examples of the Jones matrix $\boldsymbol{J}$ for optical components. [3], [5]

3.5 Stokes Parameters

Jones' approach to defining polarization states has one shortcoming. It does not have a mathematical representation of unpolarized light. To describe all the features of any polarized state, including unpolarized, the Stokes vector must be used. It is a vector with four components. This is twice the amount of numbers used in Jones vector but the Jones included complex numbers into his description. Stokes using four real numbers to

Table 3.2 Jones Vectors and Stokes Vectors for Various Polarized States

Type	Jones	Stokes
Linear Polarized (Horizontal)	$\begin{bmatrix}1\\0\end{bmatrix}$	$\begin{bmatrix}1\\1\\0\\0\end{bmatrix}$
Linear Polarized (Vertical)	$\begin{bmatrix}0\\1\end{bmatrix}$	$\begin{bmatrix}1\\-1\\0\\0\end{bmatrix}$
Linear Polarized (+45°)	$\frac{1}{\sqrt{2}}\begin{bmatrix}1\\1\end{bmatrix}$	$\begin{bmatrix}1\\0\\1\\0\end{bmatrix}$
Right Circular Polarized	$\frac{1}{\sqrt{2}}\begin{bmatrix}1\\i\end{bmatrix}$	$\begin{bmatrix}1\\0\\0\\1\end{bmatrix}$
Left Circular Polarized	$\frac{1}{\sqrt{2}}\begin{bmatrix}1\\-i\end{bmatrix}$	$\begin{bmatrix}1\\0\\0\\-1\end{bmatrix}$

represent all possible polarizations. Several definitions are listed in Table 3.3. One conventional way to define them come from the following, [2]

$$S_0 = I_x + I_y \tag{3.13}$$

$$S_1 = I_x - I_y \tag{3.14}$$

$$S_2 = I_{+45^\circ} - I_{-45^\circ} \tag{3.15}$$

$$S_3 = I_R - I_L \tag{3.16}$$

The Stokes components are numbered 0, 1, 2 & 3. The zeroth component is the total intensity value. Often to simplify calculations, this is normalized to one. The next three are difference between the x & y linear states, +45° & -45° linear states, and right and left circular states, respectively. There does exist a simple direct conversion relationship between Jones and Stokes vectors,

$$\begin{bmatrix} S_0 \\ S_1 \\ S_2 \\ S_3 \end{bmatrix} = \begin{bmatrix} 1 & 0 & 0 & 1 \\ 1 & 0 & 0 & -1 \\ 0 & 1 & -1 & 0 \\ 0 & i & 1 & 0 \end{bmatrix} \begin{bmatrix} E_x E_x^* \\ E_x E_y^* \\ E_y E_x^* \\ E_y E_y^* \end{bmatrix} \tag{3.17}$$

Note, however, that a back conversion is not that straightforward.

Table 3.3 Various Approaches to Find the Stokes Parameters

	S_0	**S_1**	**S_2**	**S_3**
Light Intensity	$I_x + I_y$	$I_x - I_y$	$I_{+45^\circ} - I_{-45^\circ}$	$I_R - I_l$
Electric Field	$E_x E_x^* + E_y E_y^*$	$E_x E_x^* - E_y E_y^*$	$E_x E_y^* + E_y E_x^*$	$i(E_x E_y^* - E_y E_x^*)$
Electric Field	$E_x E_x^* + E_y E_y^*$	$E_x E_x^* - E_y E_y^*$	$2\ Re\{E_x^* E_y\}$	$2\ Im\{E_x^* E_y\}$
Electric Field	$(E_x^0)^2 + (E_y^0)^2$	$(E_x^0)^2 - (E_y^0)^2$	$2\left(E_x^0\ E_y^0\right)\cos(\delta)$	$-2\left(E_x^0\ E_y^0\right)\sin(\delta)$
(ε, θ)	1	$\cos(2\varepsilon)\cos(2\theta)$	$\cos(2\varepsilon)\sin(2\theta)$	$\sin(2\varepsilon)$
(ψ, δ)	1	$-\cos(2\psi)$	$\sin(2\psi)\cos(2\delta)$	$-\sin(2\psi)\sin(\delta)$

Source: [5], [2]

Just like the Jones vector, the Stokes vector is transformed via a matrix equation similar to Equations 3.11 and 3.12 . It has the form,

$$S_{out} = MS_{in} \tag{3.18}$$

The connection matrix M is called the Mueller matrix and it has 16 elements examples are listed in Tables 3.4.

Table 3.4 Various Jones Matrices and Mueller Matrices for Optical Components

Linear Polarizer Horizontal Transmission [a]	$\begin{pmatrix}1 & 0\\ 0 & 0\end{pmatrix}$	$\frac{1}{2}\begin{bmatrix}1 & 1 & 0 & 0\\ 1 & 1 & 0 & 0\\ 0 & 0 & 0 & 0\\ 0 & 0 & 0 & 0\end{bmatrix}$
Linear Polarizer 45° angle of Transmission [a]	$\frac{1}{2}\begin{pmatrix}1 & 1\\ 1 & 1\end{pmatrix}$	$\frac{1}{2}\begin{bmatrix}1 & 0 & 1 & 0\\ 0 & 0 & 0 & 0\\ 1 & 0 & 1 & 0\\ 0 & 0 & 0 & 0\end{bmatrix}$
Left Circular Polarizer [b]	$\frac{1}{2}\begin{pmatrix}1 & -i\\ i & 1\end{pmatrix}$	$\begin{bmatrix}1 & 0 & 1 & 0\\ 0 & 1 & 0 & 0\\ 0 & 0 & 0 & 1\\ 0 & 0 & -1 & 0\end{bmatrix}$
Right Circular Polarizer [b]	$\frac{1}{2}\begin{pmatrix}1 & i\\ -i & 1\end{pmatrix}$	$\begin{bmatrix}1 & 0 & 0 & 0\\ 0 & 1 & 0 & 0\\ 0 & 0 & 0 & -1\\ 0 & 0 & 1 & 0\end{bmatrix}$
Coordinate Rotation	$\begin{bmatrix}\cos\theta & \sin\theta\\ -\sin\theta & \cos\theta\end{bmatrix}$	$\begin{bmatrix}1 & 0 & 0 & 0\\ 0 & \cos 2\theta & \sin 2\theta & 0\\ 0 & \sin 2\theta & \cos 2\theta & 0\\ 0 & 0 & 0 & 1\end{bmatrix}$
Sample [c]	$\begin{bmatrix}\sin\psi\ \exp(i\Delta) & 0\\ 0 & \cos\psi\end{bmatrix}$	$\begin{bmatrix}1 & -\cos 2\psi & 0 & 0\\ -\cos 2\psi & 1 & 0 & 0\\ 0 & 0 & \sin 2\psi\cos\theta & \sin 2\psi\sin\theta\\ 0 & 0 & -\sin 2\psi\sin\theta & \sin 2\psi\cos\theta\end{bmatrix}$

[a] - with unpolarized input: $S = [1\ 0\ 0\ 0]^T$
[b]- with $LP_{+45°}$ input: $S = [1\ 0\ 1\ 0]^T$
[c]- from $\rho = \tan\psi\ \exp(i\Delta)$ - the fundamental equation of ellipsometry
Source: [5]

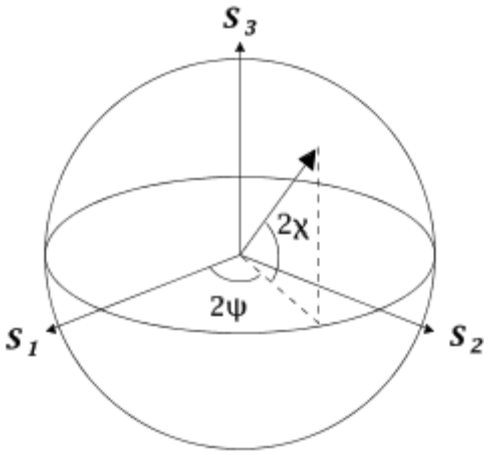

Figure 3.1 The Poincare Sphere - The S_1axis corresponds to horizontal linear polarized light. The S_2 axis is vertical polarized. This picture the pole at S_3 would be right circular light. [124]

3.6 Poincaré Sphere

The Poincaré Sphere is a model for polarized light. By using S_1,S_2,S_3 of the Stokes parameters as coordinates in 3D space, the polarization state can be modeled as a point on a sphere. As is shown in Figure 3.1, the Poincaré Sphere is a model that represents all possible polarizations of light with the exception of unpolarized light. Poincaré Sphere coordinates in terms of the Stokes parameters are as follows:

$$I = S_0 \tag{3.19}$$

$$\rho = \frac{\sqrt{S_1^2 + S_2^2 + S_3^2}}{S_0} \tag{3.20}$$

$$2\psi = \arctan2\left(S_{2,}S_1\right) \tag{3.21}$$

$$2\chi = \arctan\left(\frac{S_3}{\sqrt{S_1^2 + S_2^2}}\right) \tag{3.22}$$

The relations between Poincaré coordinates and spherical coordinates is simply,

$$r = I\rho \tag{3.23}$$

$$\theta = \frac{\pi}{2} - 2\chi \tag{3.24}$$

$$\phi = 2\psi \tag{3.25}$$

Spherical coordinates to Cartesian is just,

$$x = r\,sin(\phi)\,cos(\theta) \tag{3.26}$$

$$y = r\,sin(\phi)\,sin(\theta) \tag{3.27}$$

$$z = r\,cos(\phi) \tag{3.28}$$

It is important to note that in the Cartesian representation of the Stokes Vector, the x, y, and z coordinates directly correspond to S_1, S_2 and S_3. Essentially, they are the same. [5]

CHAPTER 4

EXPERIMENT

Portions of this work have been published in:

- T. N. Stanislavchuk, T. D. Kang, P. D. Rogers, E. C. Standard, R. Basistyy, A. M. Kotelyanskii, G. Nita, T. Zhou, G. L. Carr, M. Kotelyanskii, and A. A. Sirenko, "Synchrotron radiation-based far-infrared spectroscopic ellipsometer with full Mueller-matrix capability", Rev. Sci. Instrum. 84, 023901 (2013)

4.1 Introduction

The experimental setup described here is installed at the U4IR beamline of the National Synchrotron Light Source (NSLS) VUV ring at Brookhaven National Laboratory. Synchrotron radiation is emitted from charges moving at relativistic speeds. It is a very stable, high flux, broadband source. This powerful light source was used in this work to perform transmission and ellipsometric experiments. Transmission experiments were performed using a commercially available cryostat with a magnetic field capability. Basic reflectometry experiments measure the intensity of light before and after reflection. The experiments described in this text measure more than just reflected intensity. The polarization state of the light before and after reflection was also measured. This type of analysis is called ellipsometry. The ellipsometry experiments were done with a device built by a team at NJIT [13].

Far-IR optical experiments utilized three major components: synchrotron radiation, a Fourier transform interferometer, and a bolometer. These three were used in all experimental configurations. Transmission experiments required a cryostat for low

temperatures and a superconducting magnet for generation of the magnetic field. The polarized reflection experiments used an ellipsometer with another cryostat.

The light coming from the synchrotron beamline needed to be transformed into a known polarization state. To do this, a series of polarizing elements were used. Two polarizers and a retarder were needed to generate the polarized light. The first polarizer created the initial polarization which was linear. The second polarizer could be rotated which would shift the light into any linear polarization state. This tandem also can be used as an intensity attenuator. Next, a retarder was used to generate the circular polarization state. The combination of these three polarization elements could create any polarization state on the Poincaré sphere.

4.2 Application of Synchrotron Radiation

Synchrotron radiation (SR) based far-IR spectroscopic ellipsometry is a versatile technique for materials studies, which has been developed at several SR facilities. Funding began in 1984 for the construction of an IR port from one of the existing VUV ports at NSLS. Three years later, the IR beam was first observed [14]. The first ellipsometry experiments at NSLS-BNL, which began in the mid-90s, had been initiated in early 90s at the former Department of Solid State Spectroscopy headed by M. Cardona in the Max-Planck-Institute für Festkörperforschung (MPIFKF) [15]. The first instrument was designed and assembled at MPI-FKF and then installed at NSLS-BNL. The MPI-FKF ellipsometer was equipped with a rotating analyzer and a stationary retarder. The spectroscopic ellipsometry activity at NSLS-BNL reached its peak between 1997 and 2002, as reflected in a number of publications by Bernhard et al. [16] [17] [18] [19]

4.3 Sample Preparation

All crystals have been produced at Rutgers University in the laboratory of Prof. S.-W. Cheong. Bulk crystals were formed by the high temp flux growth technique. The crystals were vaguely round but irregular shapes about 5mm in diameter. The crystal had to be flattened and polished to meet the optical needs of the experimental setup. They were prepared using a commercially available polishing machine manufactured by the Allied High Tech Products Inc. The machine had a variable speed rotating disc. To the disc, adhered a variety of disposable diamond or SiC lapping papers at several different grits ranging from 30 to 3μm. The most commonly used lubricant was water. The final polish and therefore the finest used a 0.05μm non-crystalline colloidal silica lubricant. Samples were flattened and polished to a specific thickness. The necessary thickness was determined by the absorption found in test samples. The average thickness of a prepared sample was 0.2mm. Also the $Dy_3Fe_5O_{12}$ samples were wedged to ~3°. This was done to suppress any interference fringes produced by reflection of the parallel surfaces.

For the transmission experiments, the samples were glued to a copper aperture. The glue was double epoxy mixed with silver powder to ensure absorption around the edges and transmission through the center. The raw data of the intensity was normalized through an empty aperture of equal size to the aperture with the attached sample.

4.4 Bruker IFS 66v/S

The Bruker IFS 66v/S is a vacuum Fourier transform interferometer. The evacuated optics make it ideal for FIR measurements. It has rapid and step-scan options. With proper choice of the beam-splitter, and detector, a large spectral range can be covered.

The stable rapid scan is possible by friction-free air bearings. Beam-splitters are changed and adjusted manually. The vacuum is held ~3 mbar which is enough to eliminate the IR absorption of water and carbon dioxide from the air. There are 3 internal light sources: a mercury arc lamp, a silicon carbide globar, and a tungsten lamp for infrared to visible light. Most importantly the Bruker interferometer can also use input light from the external synchrotron light source. There is an external port through which the modulated light was passed to the Oxford Spectromag or the ellipsometer. Using a mylar beam splitter and a very sensitive bolometer, a spectrum down to ~20 cm^{-1} can be obtained.

The NSLS experimental floor contains many sources of low frequency noise mostly from various mechanical pumps. Even the self-contained helium refrigeration unit attached to the ellipsometer produced a low frequency thumping. This persistent noise could cause an error in the data collection by modulating the light at those frequencies. Fortunately, the Bruker 66 is capable of scanning at a fast speed. The unwanted low frequency noise can be pushed below the range of interest by using scan velocity >20 Hz.

4.5 Oxford Spectromag SM4000

The Oxford Spectromag SM4000 is a very important component of the transmission experiments. It is a bath cryostat with a built-in variable temperature facility. A sample is mounted on a rod which is loaded through the top of the cryostat. It is then cooled directly by the cryogen. The sample temperature can be continuously varied between 1.5 and 320 K. The cryostat holds two different cryogenic liquids, helium and nitrogen. It has a 20 L liquid helium reservoir and a 24 L liquid nitrogen reservoir. The liquid nitrogen reservoir cools the radiation shield around the liquid helium reservoir and sample space. This blocks the low temperature sections from room temperature radiation. It also protects helium reservoir from the sample space when the experiment's temperature is elevated. Refill of the liquid nitrogen is accomplished by single button automated system and takes a couple minutes. As long as the nitrogen blanket is maintained, the cryostat can hold enough helium for daily operations. The sample space is 20 mm in diameter. It is supplied the cryogen helium via a needle valve which regulates the stream from the helium reservoir for temperature requirements. The helium reservoir has only two ports. The first is the needle valve. The second is the 9.6 mm opening for a transfer line for manual refill. A check valve is attached to the neck of the second opening. It functions as an exhaust port which prevent atmosphere from entering the chamber.

The sample space requires a continuous LHe current from the liquid helium reservoir for cooling. During low temperature operation, the sample is either in direct contact with helium liquid or gas. This method of direct cooling is much faster than the cold-finger method of the ellipsometer. The bottom of the sample space is equipped with a heater and RhFe temperature sensor. These basic components are necessary for

temperature stability. An Oxford ITC503 automatic temperature controller is used to monitor the helium flow rate and heater power. To facilitate the creation of cryogenic environments, sample space pressure is pumped below 1 atm. The pump is attached to a flange in the neck of the sample chamber. Once the volume is pumped, a temperature as low as 1.5K can be reached. The pressure can be modulated by a manifold control.

The top of the cryostat also has access to wires that lead to the heat exchange and temperature sensor. The emergency relief blow out disc are located on the top along with the other major components. The sample is attached to the bottom end of the insert rod. Many sample holders were constructed. They were made in pairs and many sized apertures. One reference aperture was always needed for a baseline measurements. The other sample holder would have the prepared sample glued to it. After inserting the rod to the appropriate depth, it could rotated slightly to optimize signal the amplitude.

The method of cooling the Spectromag from room temperature to cryogenic levels is given here. The outer vacuum chamber of the cryostat must first be pumped down to between ~10^{-5} Torr. A turbo-molecular pump backed by a rotary pump was used for this. The first cryogenic fluid added is nitrogen but before adding it, it is very important to remove air from the helium reservoir and sample space to reduce the chance of humidity in the air freezing and blocking the needle valve. To remove the air, the needle vale was opened full, then the reservoir was pumped, the chamber is then filled with pure helium gas. This process is repeated several times. After the air has been removed from the sample chamber, the liquid nitrogen is added to its reservoir. Slowly, the precooling process pulls the heat from the inner and empty helium reservoir and sample chamber. This takes about 12 hours. The last thing to add is the liquid helium.

Before adding the liquid helium, the sample chamber is purged with helium gas. The helium reservoir can then be filled from a transfer line connected to a storage dewar. During the beginning of a the helium transfer, a large plume of rapidly venting exhaust gas is relieved through the check valve. It is during this time that the helium reservoir is being cooled to ~4 K for liquid helium to become thermally stable.

4.6 Ellipsometer

NJIT's ellipsometer was installed in 2010 at U4IR beamline of the NSLS VUV-IR electron storage ring. This beamline specializes in the development of new instrumentation for eventual implementation at operating IR beamlines, including for microscopy, high-field magnetospectroscopy, beam stabilization, and ellipsometry. The characteristics of the light at the U4IR beamline define many of the ellipsometer's spectroscopic capabilities. The infrared light, produced as dipole bending magnet radiation, is extracted from the storage ring through an aperture that collects an angular range of 90 mrad vertical by 90 mrad horizontal. The collected beam is transported by an optical system based on a pair of matched ellipsoidal mirrors that produce a 1:1 image of the source at a wedged diamond window. This window isolates the UHV synchrotron environment from the rough vacuum of the spectrometer and other instruments. The 90 mrad extraction and 11 mm diameter aperture of this diamond window perform optimally from the visible to 0.4 mm wavelengths (25 cm^{-1}) in the far-IR. Performance at longer wavelengths drops rapidly due to diffraction losses.

The infrared synchrotron radiation from the diamond window is collimated and transported to the Bruker IFS 66v FT-IR spectrometer. The best available spectral

resolution of the installed spectrometer is 0.3 cm^{-1}. From here, the IR radiation is sent to the ellipsometer. The exceptional brightness of the synchrotron light source exceeds that for a conventional thermal light source (T = 1200 K) by a factor of 1000 for wavelengths longer than 10 μm where the source has diffraction-limited dimensions. [16] This is crucial for throughput-limited techniques such as microscopy and ellipsometry. For microscopy, optics with a large numerical aperture (NA) of about 0.6 can be used to focus light to a spot just a few wavelengths in size. In contrast, ellipsometry requires a well-defined AOI on the sample such that the NA is limited to much smaller values of less than 0.05. Thus, the diffraction-limited spot onto the sample is nearly 50λ and the instrument's throughput is diffraction-limited at 50 cm^{-1} (λ = 200 μm) for even a 10 mm-size sample. The situation becomes even more challenging when a large AOI is needed for good ellipsometric sensitivity to, for example, a strong metallic response of the sample. Preparing large, high quality samples can be challenging, therefore effectively all far-infrared ellipsometry measurements have very low through-put. As demonstrated by Kircher et al., [17], high brightness synchrotron radiation overcomes this throughput limit and allows for relatively quick ellipsometric measurements of the samples with a modest cross section area of a few mm^2. This capability has become increasingly important for researching complex oxides where competing orders drive new physical phenomena (e.g., superconductivity, colossal magneto-resistance, multiferroicity). Understanding these materials can require probing the multi-dimensional parameter space of temperature, external electric field, pressure and orientation (e.g. anisotropic crystals); a potentially impractical measurement task without access to the rapid data collection rates at the synchrotron radiation facilities. For example, using this ellipsometer at U4IR, a

complete measurement of the temperature dependent pseudodielectric function for one sample orientation can be accomplished in less than one day.

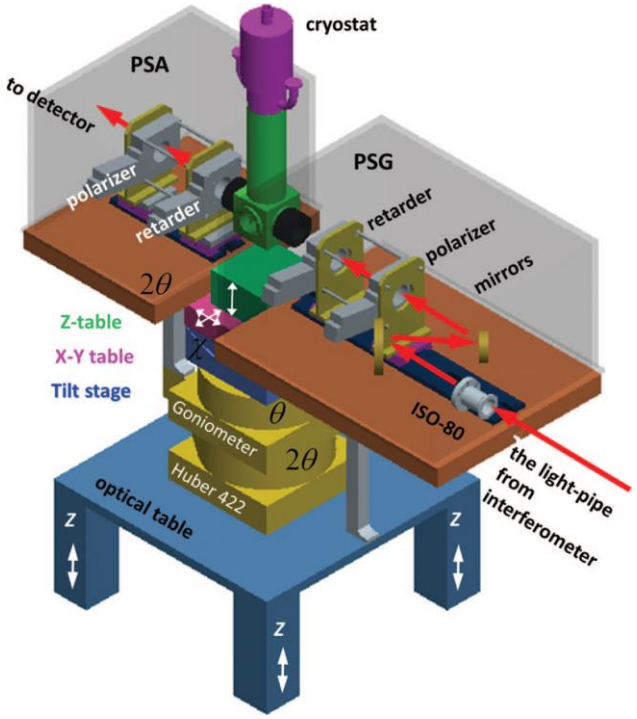

Figure 4.1 Ellipsometer at U4IR beamline consists of three major components: Polarization state generation (PSG) section, sample stage with an optical cryostat, and polarization state analyzer (PSA) section. Straight red arrow shows light propagation direction from the interferometer towards ellipsometer. Sample stage and PSA section can rotate around the same vertical axis to accommodate the ellipsometric measurements at different AOIs. [13]

Figure 4.1 shows a general schematics of Ellipsometer at U4IR beamline, which consists of several major sections: (i) Polarization State Generator (PSG), (ii) Sample Section with a cryostat, θ-2θ, χ, and X-Y-Z motorized translation stages, and (iii) Polarization State Analyzer (PSA). Far -IR and mid-IR synchrotron radiation from the storage ring passes through an FT-IR spectrometer (not shown in Figure 4.1). After that the radiation enters the PSG chamber, which is equipped with the focusing optics and

three motorized rotational stages that hold two linear polarizers and a retarder. The focused radiation with a known state of polarization is reflected from the sample mounted on a cold finger inside an optical cryostat in Sample Section. Then, the reflected light from the sample enters PSA, which is equipped with motorized stages for the optical compensator and a linear polarizer. Finally, the analyzed radiation is focused on a Detector (not shown in Figure 4.1) with a parabolic mirror. The detector is connected to the FT-IR spectrometer. The ellipsometric spectra are measured one after another for fixed position of optical polarizers and retarders. Each ellipsometric spectrum can be viewed as a regular reflectivity measurement with a known state of polarization for incoming and reflected radiation.

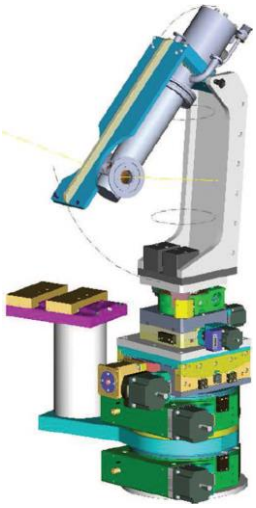

Figure 4.2 Schematics of the sample stage and the close-cycle cryostat assembly. From the bottom to the top, this assembly consists of (i) 2θ-circle with a holder for the PSA chamber, (ii) θ-circle that supports the following, (iii) χ angle adjustment stage with the travel range of ±7◦, (iv) XYZ stage, and (v) a close-cycle cryostat that is shown in the sample-loading position. [13]

Studies of the phase transitions in strongly correlated materials and multiferroics usually require low temperatures for the sample. For that purpose, the Sample Stage of

the Ellipsometers can accommodate one of the two cryostats, a LHe-flow from OXFORD or a closed-cycle one from ARS, which can be used interchangeably for the sample cooling down to LHe temperatures. Both cryostats belong to the "cold-finger" type with the sample positioned in high vacuum. The sample is mounted on a 4 mm-diameter holder and is surrounded by two cold copper shields with holes for the light access. By design, no cold optical windows are used in the cryostats. The sample temperature is measured with Si-diode sensors connected to one of the OXFORD or Lakeshore temperature controllers, which are integrated into the Labview-based Experiment Control program. The closed-cycle system allows sample temperature variation between 6 and 450 K. This system does not require LHe and the cooling power is provided with a He gas compressor. The initial cooling time from 300 K to 6 K is about 3 hours. Figure 4.2 shows the closed-cycle cryostat in the sample loading position on top of the XYZ- 2-circle-goniometer assembly. This design allows for the sample exchange time to be less than 10 min excluding, of course, the warm-up, pump-down, and cool-down time intervals. One of the disadvantages of the closed-cycle system is related to mechanical vibrations that are transmitted from the compressor to the bolometer trough the metal parts of Ellipsometer. These vibrations result in a significant noise on the bolometer in the low-frequency range that can be detrimental for ellipsometric measurements of weak signals. An effective solution to this problem includes a combination of both (i) a high scanning speed of the Bruker spectrometer above 80 kHz and (ii) application of an external highpass electronic filter between the bolometer output and the detector input for the FT-IR spectrometer. If both of the above applied, the ellipsometry spectra can be measured in the broad frequency range above 50 cm^{-1} with unnoticeable disturbance from

the He compressor. The continuous LHe flow system allows for the cold-finger temperature variation between 4 K and 300 K. The cooling power is provided with a LHe flow through a transfer line. The initial cooling time from 300 K to 5K is about 0.5 hour. The LHe consumption is between 5 and 10 liters per experimental day. The LHe flow system is free of vibrations and is preferable for measurements of small samples in the far-IR spectral range below 100 cm^{-1}.

CHAPTER 5

MULTIFERROICS

Multiferroics are a very popular and exciting classification of materials. In multiferroic crystals two or more primary ferroic properties are joined in the same phase. The coupling between ferromagnetism and ferroelectricity, spontaneous ordering which produces magnetization and polarization is of strong interest to current researchers. This coupling is specifically called the magnetoelectric effect. Rare Earth Iron Garnets and Rare Earth Manganites are compounds which both exhibit the magnetoelectric effect.

Portions of this work have been published in:

- T. D. Kang, E. C. Standard, K. H. Ahn, and A. A. Sirenko, G. L. Carr, S. Park, Y. J. Choi, M. Ramazanoglu, V. Kiryukhin, and S-W. Cheong, "Coupling between magnon and ligand-field excitations in magnetoelectric $Tb_3Fe_5O_{12}$ garnet", Phys. Rev. B **82**, 014414 (2010)

- T. D. Kang, E. C. Standard, P. D. Rogers, K. H. Ahn, and A. A. Sirenko, A. Dubroka, C. Bernhard, S. Park, Y. J. Choi and S.-W. Cheong, "Far-infrared spectra of the magnetic exchange resonances and optical phonons and their connection to magnetic and dielectric properties of $Dy_3Fe_5O_{12}$ garnet", Phys. Rev. B **86**, 144112 (2012)

- E. C. Standard, T. Stanislavchuk, A. A. Sirenko, N. Lee, and S. -W. Cheong "Magnons and crystal-Field transitions in hexagonal $R$$MnO_3$ (R = Er, Tm, Yb, Lu) single crystals", Phys. Rev. B **85,** 144422 (2012)

5.1 Introduction

Physicists have long known of a correlation between magnetic and electric fields. Ampere in the 1820's first observed the deflection of a magnetic compass needle by a wire carrying electrical current. The theory of electromagnetism culminated in the 1860's with Maxwell's famous equation. The power of Maxwell's equations cannot be understated. His equations helped ignite a revolution of technological innovation that still burns strong today. A interaction between displacement $\boldsymbol{D}$ and induction $\boldsymbol{B}$ on both the electric field $\boldsymbol{E}$ and auxiliary magnetic field $\boldsymbol{H}$ within a moving object was proved by Wilhelm Röntgen in 1888. Six years later Pierre Curie published a paper of the first discussion of an intrinsic correlation between magnetic and electric properties. In 1926, Peter Debye named this correlation "magnetoelectric" since electromagnetic already had its usage. A major theoretical development came in L. D. Landau and E. M. Lifshitz seminal work on theoretical physics, specifically *Electrodynamics of Continuous Media* in 1957. In their words: "The magnetoelectric effect is odd with respect to time reversal and vanishes in materials without magnetic structure". This brief discussion probably helped Igor Dzyaloshinskii, who in 1959 predicted that the magnetoelectric effect should exist in chromium oxide. His prediction was verified a year later by D. N. Astrov who showed magnetization dependent on electric fields. The following year V J. Folen et al. observed polarization dependent on auxiliary magnetic field. Since these historical development, many researchers have found other magnetoelectric materials with varying causes.

They are two major classification of magnetoelectric type I and type II. Type I is also called "proper". These are generally good ferroelectric the coupling between

ferromagnetism and ferroelectricity is normally weak. This is because the reason for the ordering arises from completely different ions. For the example of oxide perovskites with the general formula ABO_3, magnetism arises from transition metal ions with partially filled *d* orbitals. Ferroelectricity comes from non-magnetic cations being shifted from center of inversion. This shift is called noncentrosymmetricity and when it occurs with cations and anions a dipole moments is induced. The classic example is bismuth ferrite $BiFeO_3$. Iron Fe^{3+} has five 3*d* electron causing the ferromagnetism. Bismuth Bi^{3+} creates a structural distortion from its lone pair of two 6*s* electron. The distortion moves bismuth from is center position thereby inducing polarization.

Type II is also called "improper" or magnetic multiferroic because ferroelectricity comes from the ferromagnetically ordered system. Spiral magnetic alignment or sometimes collinear alignment can cause the polarization. Newham theorized that noncentrosymmetric magnetic ordering could produce the electric polarization. [18]

The Free energy for the magnetoelectric system is given by the following

$$-F(E,H) = \frac{1}{2}\varepsilon_0\varepsilon_{ij}E_iE_j + \frac{1}{2}\mu_0\mu_{ij}H_iH_j + \alpha_{ij}E_iH_j + \frac{1}{2}\beta_{ijk}E_iH_jH_k + \frac{1}{2}\gamma_{ijk}H_iE_jE_k. \quad (5.1)$$

The first two terms on the right hand represent responses of the electric and magnetic fields. They both contain second -rank tensors, $\varepsilon_{ij}(T)$ and $\mu_{ij}(T)$. The linear magnetoelectric coupling is described by the third term $\alpha_{ij}(T)$. Higher order, quadratic, magnetoelectric coefficients are from the third rank $\beta_{ijk}(T)$ and $\gamma_{ijk}(T)$. The magnetoelectric effects can be written in the form of $P_i(H_j)$ and $M_i(E_j)$. By

differentiating F with respect to E_i and setting $E_i = 0$ and performing a similar procedure on H_i, then one gets

$$P_i = -\left.\frac{\partial F}{\partial E_i}\right|_{E_j=0} = \alpha_{ij}H_j + \frac{\beta_{ijk}}{2}H_jH_k \tag{5.2}$$

$$\mu_0 M_i = -\left.\frac{\partial F}{\partial H_i}\right|_{H_j=0} = \alpha_{ji}E_j + \frac{\gamma_{ijk}}{2}E_jE_k \tag{5.3}$$

The magnetoelectric tensor α_{ij} is constrained by the geometric mean of the diagonalized tensors ε_{ii} and μ_{jj}. By forcing the first three terms in Equation 5.1 to be greater than zero, then the following relation can be obtained,

$$\alpha_{ij}^2 \leq \varepsilon_0\mu_0\varepsilon_{ii}\mu_{jj} \tag{5.4}$$

This relation tells us that a multiferroics that already has a large permittivity and permeability, such as ferromagnetic and ferroelectric materials, should have a large linear magnetoelectric effect. The tensor α_{ij} can only be non-zero when the material lacks a center of symmetry and has no time reversal symmetry.

Magnetoelectric coupling can be measured indirectly. This can be done by observing changes in either the magnetization near a ferroelectric transition temperature or the dielectric constant near a magnetic transition temperature. The resulting effects are sometimes called magnetocapacitance or magnetodielectric. Directly observing a magnetic response to an electric field or electrical response to a magnetic field is more challenging but possible. These experiments are done by effecting a sample electrically in a magnetometer.

The data storage application of multiferroics lies in the ability of reversing the magnetization by applying an electric field or vice versa. This magnetoelectric switching effect has been seen in orthorhombic rare earth manganites. Also, hexagonal rare earth

manganites display the linear magnetoelectric effect. An electrically driven magnetic phase transition was detected in $HoMnO_3$. This is an interesting switching mechanism that may offer new approach to magnetoelectric switching. [9]

5.2 Rare Earth Iron Garnets

$Tb_3Fe_5O_{12}$, $Dy_3Fe_5O_{12}$, as well as the other related rare earth iron garnets, are ferrimagnetic materials with huge magnetostriction, which is related to the combination of a strong anisotropy of the crystal field of the R^{3+} ions and to a strong and anisotropic superexchange interaction between R^{3+} and iron. [19] [20] [21] Hur et al. reported on the large magnetoelectric effect in Tb-IG in 2005 using an AC electric field and a perpendicular magnetic field. Paul Rogers et al. saw the same effect in Dy-IG in 2011 using a combination of RAE and transmission experiments.

At room temperature Rare Earth iron garnets are cubic with the space group $Ia3d(O_h^{10})$. The schematics of the crystal and magnetic structure of *R*-IGs can be found, for example, in References [20] and [21]. Below the transition temperature of $T_N \approx 550$ K iron spins are ordered ferrimagnetically in the [1 1 1] direction. The iron Fe^{3+} ions occupy two sites: 16a octahedral sites with the $\bar{3}$ (C_{3i}) symmetry and 24c tetrahedral sites with the $\bar{4}(S_4)$ symmetry. The iron Fe^{3+} spins in these two sites are antiparallel to each other. The Dy^{3+} ions with the ground state ${}^6H_{15/2}$ and Tb^{3+} ions with the ground state ${}^7F_6$ are in the 24d dodecahedral sites with the local orthorhombic symmetry 222(D_2). For both Dy and Tb there are several non-equivalent ions in each unit cell with the same surrounding field, but the axes are inclined to each other. This has the overall effect of producing an

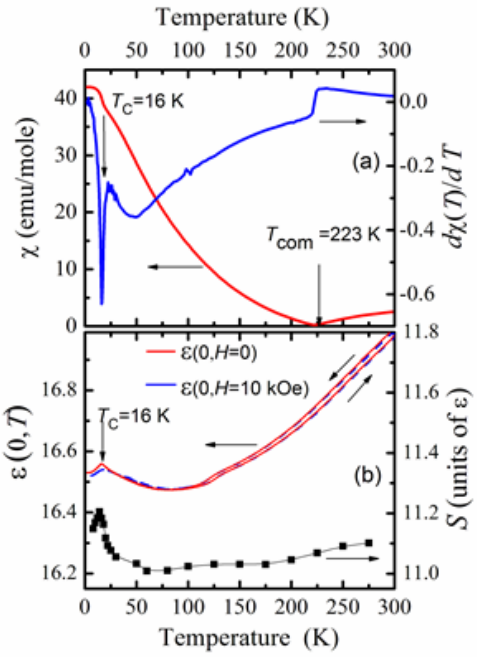

Figure 5.1 (a) Temperature dependence of the static magnetic susceptibility (red curve) and its derivative (blue curve) for $Dy_3Fe_5O_{12}$ single crystal from Reference. 5. FM ordering of Dy^{3+} spins occurs at T_C =16 K. The compensation point for the total Fe and Dy magnetization is marked with a vertical arrow at T_{com} = 223 K. (b) Temperature dependence of the static dielectric constant at H=0 (red) and at H =10 kOe (blue) from Reference. 5. The total oscillator strength $\sum_j^N S_j(T)$ of all optical phonons measured using spectroscopic ellipsometry is shown with black squares. Note that the right and left vertical scales in (b) have an offset of 5.2, which is close to ε_∞ for Dy-IG.

average cubic symmetry. The Rare Earth spins in the dodecahedral sites are antiparallel to iron's net magnetic moment.

Among six possible exchange interactions between spins in three different magnetic subsystems (a, c, and d) only two dominate. [22] [20] The main magnetic superexchange interaction is between the antiparallel Fe spin in the tetrahedral and octahedral sites. Another important interaction is between the antiparallel spins of the Rare-Earth ions and Fe ions in the tetrahedral sites. For $Dy_3Fe_5O_{12}$ at T_{com} =223 K the total magnetization of Dy and Fe sublattices is compensated: M=0. The temperature

dependence of $\chi(T) = M(T)/H$ from Reference [23] is shown in Figure 7.1 where the compensation point at T_{com}=223 K is marked with an arrow.

For $Dy_3Fe_5O_{12}$ below 100 K, a rhombohedral distortion of the cubic cell causes the canting of Dy spins, which is described as a "double umbrella structure". In $Tb_3Fe_5O_{12}$ a rhombohedral distortion of the cubic cell occurs below 150 K. This again comes with the canting of Rare Earth (*R*) moments called the double umbrella structure. The increased magnetic anisotropy below 150K comes from the appearance of noncollinear spins of the Tb moments, which is steadied by the anisotropic exchange interaction between Fe *3d* and Tb *4f* electrons and crystal field anisotropy. The Tb spins sweep out and form a double cone around the [1 1 1] at low temperatures. The anisotropic Tb *4f* electron clouds are coupled to the spin by the spin-orbit interaction, the canting of the Tb spins creates the rhombohedral distortion along the magnetic easy axis. Magnetostriction comes from the spin rotation of the applied H field resulting in a redistribution of the electron clouds and a reorientation of the rhombohedral domain. In short, the induced H-field reorients the rhombohedral domains changing the macroscopic electronic or ionic polarizability which is determined by the dielectric constant. [24] [23]

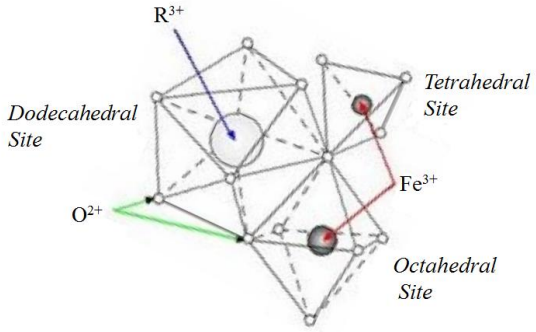

Figure 5.2 The crystal structure of *R*-IG's The 3 trivalent R^{3+} ion are located on the dodecahedral sites. Two of the Fe ions are on octahedral sites, the other three Fe are on tetrahedral sites. In the example of $Dy_3Fe_5O_{12}$, below $T_N \approx 550\,K$ the Fe spins are ordered in a ferrimagnetic structure along [1 1 1] direction. The main magnetic superexchange interaction, is between Fe in two different sites, spins of Fe in octahedral are antiparallel to the tetrahedral. Also, Dy spins are antiparallel to Fe moments in the tetrahedral sites. [126] [127]

The symmetry of Dy^{3+} and Tb^{3+} is lowered from 222(D_2) tetragonal to 2(C_2) monoclinic. Below 50 K, the iron sublattice magnetization does not change appreciably with temperature. However, the Dy sublattice magnetization increases rapidly with the temperature decrease. It is reflected in the change of $\partial\chi(T)/\partial T$ for T<50 K in Figure 5.1. The anomaly in $\partial\chi(T)/\partial T$ at T_C =16 K corresponds to the appearance of the FM ordering for Dy^{3+} spins. [23] This transition was also studied by specific heat and high field magnetization measurements and was associated with the iron spin reorientation from the easy $\langle 111 \rangle$ axis to a low-symmetry angular phase. [25] [26] A slightly lower transition temperature of 14.5 K was reported in Reference [25].

5.3 Rare Earth Manganites

Many members of the rare earth manganite family have multiferroic properties. Hexagonal Rare Earth Manganites have $P6_3cm$ symmetry in which S = 2 Mn^{+3} form

planes of side sharing triangles perpendicular to the *c* axis. The Mn spin interaction is antiferromagnetic. Anisotropy keeps the spins constrained to the basal plane. The MnO_5 planes are separated by layers of the rare earth ions. The ferroelectric order comes from displacement of the rare earth atoms along the *c* axis with cooling below the T_C. [27]

Hexagonal manganites RMnO$_3$ (R= Ho, …Lu, and Sc, Y) exhibit ferroelectric (FE) order with a fairly large remnant polarization at high temperatures with the T_C values in the range between 600 K and 1000 K. [28] [29] The RMnO$_3$ hexagonal structure consists of close-packed layers of MnO_5 bipyramids, which share corners in the a-b planes. Along the c-axis, the layers of MnO_5 are well separated by the R^{3+} ions. A cooperative tilting of the bipyramidal sites below T_C displaces the R^{3+} ions along the c-axis into two non-equivalent 2a and 4b sites. The oxygen ions are also displaced in the a-b plane. Both displacements of R^{3+} ions and oxygen result in the FE polarization. [30] [31] Detailed drawings of the hexagonal RMnO$_3$ crystal structure [the polar space group $P6_3cm$ (C_{6v}^3)] along with more detailed discussion of the ionic displacements in the FE phase can be found in References [32] [30] and [33].

The magnetic structure of hexagonal manganites RMnO$_3$ have been studied in a number of publications. [33] [34] [35] [36] However, the most intriguing part about the magnetic interaction between Mn^{3+} and R^{3+} spins at low temperatures and high magnetic fields is still under debate. [37] [38] The commonly accepted view on the magnetic structure and the corresponding magnetic phase transitions is the following. An antiferromagnetic (AFM) order of the Mn^{3+} spins occurs at much lower temperatures compared to the FE transition. The AFM transition temperature T_N for Mn^{3+} spins is in the range between 70 K and 87 K for R= Y, Ho, Er, Tm, Yb, and Lu depending almost

linearly on r_i. [32] The neighboring spins of the close-packed Mn^{3+} ions are AFM-coupled via the oxygen ions by superexchange interaction, which gives rise to frustration effects of an ideal 120° angle structure with the space group $P6'_3c'm$. The Mn^{3+} spins are ordered perpendicular to the c-axis: $\vec{S}_{\mathrm{Mn}} \perp c$, while at low temperatures spins of R^{3+} ions (R=Ho, Er, Tm, Yb) are oriented along the c axis: $\vec{S}_R \parallel c$. R^{3+} ion spins S_R can interact among themselves and with the Mn^{3+} spins. These interactions result in a complex phase diagram in the temperature-magnetic field parameter space T-H. [38] Among all hexagonal $R\mathrm{MnO_3}$ compounds with $S_R \neq 0$, $\mathrm{HoMnO_3}$ is the most studied material. Its magnetic structure is particularly interesting since it shows two additional phase transitions below T_N. Mn^{3+} spin reorientation occurs at $T_R \approx 40$ K and AFM ordering of Ho^{3+} spins takes place at $T_R \approx 5$ K, as observed in neutron scattering ([39] [40]) and second-harmonic generation optical experiments. [41] [42] [43] [44] The spin reorientation is believed to be related to the S_{Mn} rotation in the a-b plane by 90°, changing the magnetic symmetry from $P6'_3c'm$ to $P6'_3cm'$. At much lower temperatures $T < T_R$, another modification of the Mn spin structure occurs restoring the $P6_3cm$ symmetry. Both low-temperature transitions at T_{SR} and T_R are also accompanied by a complete or partial ordering of the Ho^{3+} spins, which structure is not resolved yet. As mentioned in Reference [37], two possibilities are discussed in literature for the spins of two non-equivalent Ho^{3+} sites: (i) Ho spins on the 4b site develop AFM order below T_{SR} while Ho spins on the 2a site remain PM, and (ii) all Ho spins develop AFM order below T_{SR}. In any case, there is an agreement that the Ho sublattice exhibits long-range AFM order along the c-axis below $T_R \approx 5$ K. [37] Magnetization of the R spins at low

temperatures in other hexagonal manganites with *R*= Er, Tm, Yb has been also studied in References [45] [46]& [47] where Dzyaloshinskii–Moriya (DM) interaction (References [48] [49]) has been proposed as one of the mechanisms for coupling between *R* spins with the partial AFM order along the c-axis and Mn spins that are ordered in the a-b plane.

5.4 Electromagnons

The strong coupling between magnetic and lattice degrees of freedoms in multiferroic materials can give rise to an excitation called an electromagnon. In 2006, Pimenov et al. [50] used terahertz light to stimulate spin waves in perovskite $TbMnO_3$ and $GdMnO_3$. Both materials are examples of a family of multiferroics in which ferroelectricity is induced by magnetic order. The spin waves were excited by the oscillating electric field in the light wave which was proved by using polarized light along all principal crystallographic axes. The excitation was suppressed when the alternating electric component was rotated from $\vec{\boldsymbol{E}} \parallel a$ to $\vec{\boldsymbol{E}} \parallel b$. Yet, the excitation did not change when the alternating magnetic component was changed from $\vec{\boldsymbol{H}} \parallel b$ to $\vec{\boldsymbol{H}} \parallel c$. Their results showed the excitations to be electric-dipole-active in that electric fields activated the electric dipoles, which then affect the magnetic structure. This was unusual because the modes were connected to the magnetic structure but the excitation came from the oscillating electric field. In the end, they discovered a new hybrid spin lattice excitation which exists in multiferroic materials that can be excited by the electric component. [50]

In 2007, Sushkov et al. [51] reported on the observations of electromagnons in RMn_2O_5 and the non-rare earth YMn_2O_5. Their work showed that the spectra of YMn_2O_5

and $TbMn_2O_5$ were very similar. This proved the Mn origin of electromagnons in these compounds. [51] Electromagnons have also been seen in non-multiferroic materials such as hexaferrite $Ba_2Mg_2Fe_{12}O_{22}$. [52] It is now expected that may magnetically ordered system with noncollinear magnetic structure can support electric-dipole-active magnon.

Transmission experiments have been used to determine the complex dielectric constant $\varepsilon = \varepsilon_1 + i\varepsilon_2$. The electromagnon is seen as a magnetic resonance in the dielectric constant spectrum $\varepsilon(\omega)$. The spectra of electromagnons in rare earth multiferroic manganites have been seen in the frequency range 10 cm^{-1} to 30 cm^{-1}. The electromagnon is a mechanism of the magnetoelectric effect within multiferroic manganites. The existence of the electromagnon is not dependent on a rare earth magnetic sublattice. Electromagnons are over damped and not well observed in the collinear incommensurate AFM phase. At lower temperatures they are observed as broad absorption lines only in the spiral incommensurate AFM phase and partly in the paramagnetic phase. The magnetoelectric interaction not only gives rise to electromagnons but also to a static electric polarization in the spiral state. This means that electromagnons must correspond to lattice distortions. [53]

CHAPTER 6

ROTATING BROADBAND RETARDERS

This chapter is the first where the original results are presented. Rotatable retarders have been developed for applications in spectroscopic, full Mueller Matrix ellipsometry in the far-IR spectral range. Several materials, such as silicon, KRS-5, and a commercial polymer plastic (TOPAS) have been utilized to achieve a fully adjustable retardation between 0° and 90°. Experimental characteristics of the rotatable retarders that utilize a three- and four-bounce design are compared with calculations. Also discussed is the current setup at the U4IR beamline of the National Synchrotron Light Source (NSLS) in the Brookhaven National Laboratory (BNL).

Portions of this work have been published in:

- T.D. Kang, E. Standard, G. L. Carr, T. Zhou, M. Kotelyanskii, and A. A. Sirenko, "Rotatable broadband retarders for far-infrared spectroscopic ellipsometry", Thin Solid Films, 519, 2698 (2011)

- T. N. Stanislavchuk, T. D. Kang, P. D Rodgers, E. C. Standard, R. Bastistyy, A. M. Kotelyanskii, G. Nita, T. Zhou, G. L. Carr, M. Kotelyanskii, and A. A. Sirenko, "Synchrotron-radiation based far-infrared spectroscopic ellipsometer with a full Muller matrix capability", Rev. Sci. Instr. (2012)

6.1 Introduction

Broadband optical retarders are required for spectroscopic ellipsometry in its full-Muller-matrix (MM) realization. Performance of the MM ellipsometer depends on the capability to produce substantially linearly-independent Stokes vectors, incident at the measured sample. As has been shown in [54], the errors in the measured MM of the sample are proportional to the condition number of the 4×4 matrix composed of the Stokes vectors

of four polarization states incident at the sample. It can be proven, that it is impossible to cover the Poincaré sphere with linearly-independent Stokes vectors by only changing linear polarization at the input surface of a stationary retarder. As will be illustrated further in this chapter, total coverage of the Poincaré sphere is possible by rotating a tandem of a linear polarizer and a retarder with retardation of 90°. Traditionally, broadband retarders are made of a single triangular prism where the phase retardation between the *s* and *p* polarizations is obtained at the total internal reflection inside the prism. The prism is cut for normal incidence at both the entrance and exit surfaces, thus eliminating any polarization effects at these surfaces. For the internal reflection, the incident angle θ should be greater than the critical angle to avoid intensity losses. By using Fresnel reflection coefficients, the one-bounce retardation δ that occurs from total internal reflection at incident angle θ in a prism material is obtained [55] [56]:

$$\tan\left(\frac{\delta}{2}\right) = \frac{(\sin^2\theta - n^{-2})^{1/2}}{(\sin\theta \tan\theta)} \tag{6.1}$$

Calculations for the maximum retardation provided by a single prism made of different materials are shown in Figure 6.1a. Transparent and isotropic materials are usually used, such as silicon, KRS5, polycrystalline ZnSe, or plastic. One can see that the 90^{o} retardation is not always possible with a single reflection, especially for low-index materials, such as TOPAS plastic. However, a 90° retardation can be obtained with two or more internal reflections. The choice of the retarder material is determined by the spectral range of the measurements. For example, the free-carrier absorption at low frequencies and the weak phonon absorption band at 520 cm^{-1} can affect the performance of a Si retarder. KRS5 can be used only in the frequency range above 400 cm^{-1} due to phonon absorption.

The single-prism (= one internal reflection) design has obvious disadvantage for the broadband spectroscopic MM ellipsometry. To create at least four linearly-independent Stokes vectors on the sample surface, the prism should be rotated, which will ultimately steer the light beam off the optical axis of the ellipsometer. To return the beam back to the optical axis of the ellipsometer, one needs at least two more reflections. However, metal mirrors positioned at high incident angle are not always suitable for this purpose due to dispersion that would result in a strong spectral dependence of retardation even in the far-IR spectral range. Another problem is related to metal mirror contamination that will also change the retardation over time and will require a frequent recalibration of such retarder. To avoid this problem, various designs for rotating retarders relying on the double-Fresnel-rhomb approach have been proposed [57] [58]. However, no commercial solution is known for the far-IR spectral range.

A far-IR spectroscopic ellipsometer with the full MM capability has been recently developed at the U4-IR beamline at NSLS-BNL. Investigated is a possibility to use Si, KRS5, and TOPAS plastic for retarders in the spectral range between 10 and several thousands of cm^{-1}. Note that TOPAS plastic is transparent in both, visible and far-IR spectral ranges, which simplified greatly the alignment process for TOPAS retarders inside the ellipsometric optical system. This chapter focuses on their performance in the most challenging far-IR spectral range between 10 and 100 cm^{-1}.

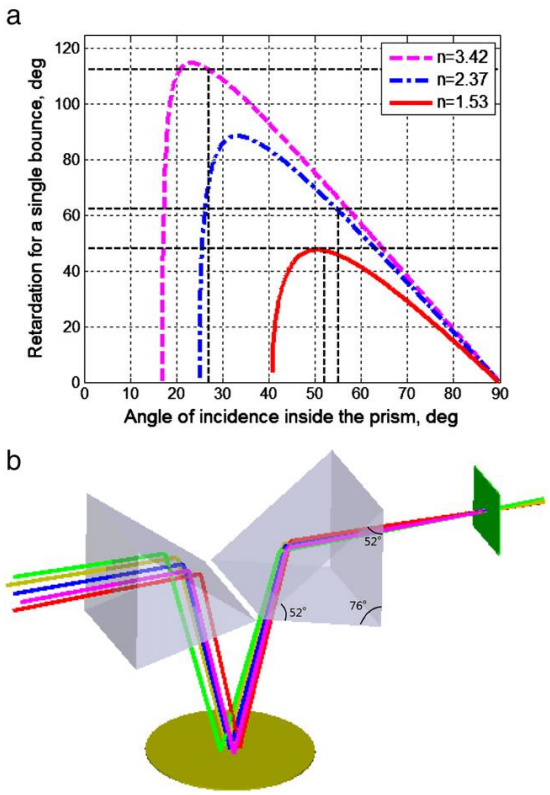

Figure 6.1 (a) The relative phase shift between s and p polarizations for a single bounce at the total internal reflection using far-IR average values of the refractive index of Si: n=3.42, KRS5: n= 2.37, and TOPAS: n = 1.533. (b) TOPAS retarder in a focused beam. The central beam that propagates along the optical axis is shown with blue, the 3,6,9 and 12 o'clock beams are shown with pink, red, brown, and green colors. The sample is shown at the focus point.

6.2 Calculations

One of the designs for the rotating retarder, which was implemented in the U4IR ellipsometer, is shown in Figure 6.1b**.** It consists of two TOPAS prisms and a gold mirror. A small angle of 14° is used for the mirror reflection, therefore the possible retardation at the mirror surface is calculated to be ~180° in the far-IR spectral range. Note that, as for the reflection coefficients in this dissertation, the Nebraska convention [59] is followed by which the Equation 6.1 was derived. The refractive index of TOPAS

is n=1.533 in the far-IR. One bounce results in a ~45° phase shift between s and p input linear polarizations for the prism angle of about 52°. This angle is marked with a dashed vertical line in Figure 6.1a.

Another design for retarders for the far- and mid-IR spectral range is based on the double-Fresnel rhomb. Figure 6.2 shows the ZEMAX model and pictures of Si retarders. Four internal reflections at the angle of 27° keep the input and the output beams on the optical axis and provide the total phase shift of 450° (360°+90°). The dashed vertical line in Figure 6.1a indicates the angle of 27°. Note that if a larger angle of reflection is

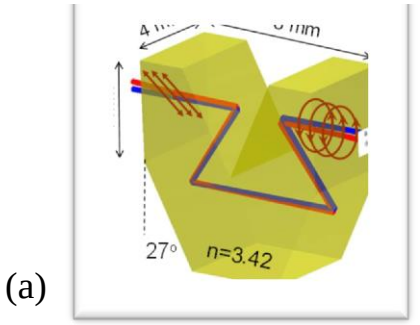

(a)

(b)

Figure. 6.2 (a) Design for a silicon double Fresnel rhomb (4 bounces) as a far infrared phase retarder with approximate dimensions shown in the figure. Theoretical operational range is between 10 and 450 cm-1. Polarizations of the incoming (S_2) and transmitted light (S_3) are shown schematically for the left and right hand sides of the retarder respectively. (b) Retarders made of semi-insulating silicon.

utilized, thus that the total phase shift is 90° or 270°, then the retarder length and, hence, the optical path inside the retarder becomes prohibitively long. A KRS5 retarder for the mid-IR spectral range has been developed utilizing a four-bounce design yielding a total phase shift of 270°.

To create a linearly-independent set of the Stokes vectors on the sample, a tandem of a linear polarizer and a retarder is used in the modern ellipsometer design [60]. The MM for rotating retarder depends on the angle of rotation ϕ with respect to the plane of the input linear polarization. The following expression (Equation 6.2) is a Mueller matrix for the rotated retarder assembly with Δ_c and Ψ_c characterizing the retarder itself [60]

$$\begin{bmatrix} 1 & \cos 2\Psi_c \cos 2\phi & \cos 2\Psi_c \sin 2\phi & 0 \\ \cos 2\Psi_c \cos 2\phi & \cos^2 2\phi + \sin 2\Psi_c \cos\Delta_c \sin^2 2\phi & (1-\sin 2\Psi_c \cos\Delta_c)\sin 2\phi \cos 2\phi & -\sin 2\Psi_c \sin\Delta_c \sin 2\phi \\ \cos 2\Psi_c \sin 2\phi & (1-\sin 2\Psi_c \cos\Delta_c)\sin 2\phi \cos 2\phi & \sin 2\Psi_c \cos\Delta_c \cos^2 2\beta + \sin^2 2\phi & \sin 2\Psi_c \sin\Delta_c \cos 2\phi \\ 0 & \sin 2\Psi_c \sin\Delta_c \sin 2\phi & -\sin 2\Psi_c \sin\Delta_c \cos 2\phi & \sin 2\Psi_c \cos\Delta_c \end{bmatrix}$$

Here $\cos\Delta_C=\Delta_F-\Delta_S$ and $\Psi_C = \tan^{-1}(|t_F|/|t_S|)$ are defined with $t_F=|t_F|\exp(i\Delta_F)$ and $t_S=|t_S|\exp(i\Delta_S)$, which are the transmission coefficients along the fast and slow axis, respectively [61].

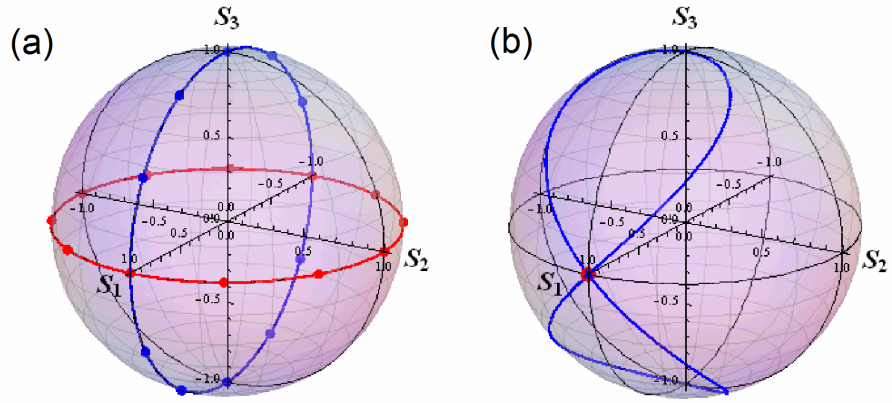

Figure 6.3 (a) Polarization change for a stationary retarder. Input Stokes vectors at the equator are shown with red, the output ones are shown with blue color. Note that any three Stokes vectors are linearly dependent. (b) Polarization change for a rotating retarder. Input Stokes vector is shown with a red solid circle, the output ones are shown with blue color.

If the linear polarization changes at the input of an ideal stationary retarder, the corresponding output Stokes vectors form a circle on the Poincaré Sphere as shown in Figure 6.3(a). Note that all these Stokes vectors are linearly-dependent preventing a full MM analysis of the measured sample. For a tandem of a rotating retarder and a stationary input linear polarizer, the Stokes vectors are shown in Figure 6.3(b). They form a "figure-8", which can produce a number of linearly-independent combinations of 3 Stokes vectors [62]. If a full coverage of the Poincaré sphere is required, both the input linear polarizer and the retarder have to be rotated. Figure 6.4(a) shows results of rotation of an ideal retarder for four positions of an input linear polarizer.

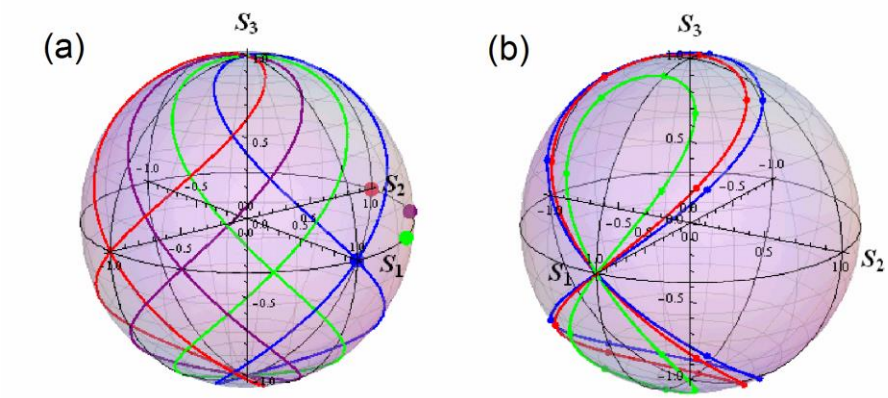

Figure 6.4 (a) Polarization states on the Poincare sphere for four positions of the input linear polarizer: 0° (blue), 15° (green), 30° (purple), and 45° (red). Note that a uniform coverage of the sphere is possible for rotation of the input linear polarizer. (b) The Poincare sphere for polarization changes for a rotating retarder made of two prisms with a fixed angle 52° and three different values of the refractive index: n=1.4 (blue), n=1.533 (red), and n=1.6 (green).

The maximum value of retardation depends on the prism angle and the refractive index of the prism. Dispersion of the prism material in the far-IR spectral range is not strong, especially in the frequency range below the optical phonon absorption. Nevertheless, dispersion can change the maximum value of retardation at different frequencies. This effect is illustrated in Figure 6.4(b), which shows results of calculation for the same prism and three values of the refractive index: n=1.4, n=1.6, and n=1.533, where the latter is the known value for TOPAS in the far-IR, n=1.6 is the refractive index value in the visible, and n=1.4 is chosen for illustration purpose. One can see that in both, the higher-index and the lower-index cases, the maximum retardation value of 90° cannot be achieved for a fixed geometry of the prism. In the lower index case, there is an "overshoot" around the poles of the Poincaré sphere, and in the high-index case,

there is an “undershoot”. Both of each would leave a “hole” around the pole for a random coverage of the Poincaré Sphere.

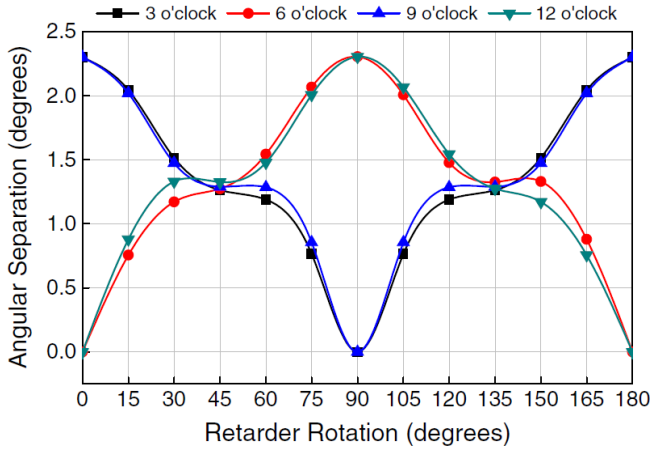

Figure 6.5 The angle separation between the Stokes vectors for the central beam and four focused beams propagating at 3, 6, 9, and 12 o'clock through the prism retarder as shown in Figure 6.1(b).

In a real ellipsometer, the light is usually focused on a sample and the retarder should be placed in a cone of the focused light [Figure 6.1(b)]. To minimize the polarization variation across the light beam, usually a slow focusing is chosen with the *f*-number more than 20. In the NSLS ellipsometer *f*=40, which gives the beam convergence of about ±1.43°. Nevertheless, the retarder will produce a change of polarization across the beam profile. Five beams were analyzed: “12”, “3”, “6”, and “9 o’clock” including the reference beam that passes along the optical axis and is marked with “zero”. The absolute values of the angles between the Stokes vectors that correspond to the central beam and the other four beams are shown in Figure 6.5. For each beam, these values oscillate between zero and 2.3° for complete rotation of the retarder. This corresponds to the variation in the individual components of the generated Stokes vectors δS not exceeding tan(2.3°)≈0.04. Full effect of this systematic error on the accuracy of the

sample Mueller matrix measurements requires analysis of the whole ellipsometer system and also depends of the sample properties.

6.3 Experimental Results

Experimental calibrations for a double-prism TOPAS retarder were carried out at the U4IR beamline at NSLS-BNL. The experimental setup consisted of three wire-grid linear polarizers (P_0, P_1, A) and a single retarder (C) positioned in the following order: P_0, P_1, C, A, respectively. The behavior of the TOPAS retarder used in the NSLS experiments is the following: linearly-polarized radiation (after the wire-grid polarizer) enters the retarder front surface, which is normal to the beam. After the total internal reflection, the beam is directed to the gold mirror. The maximum value of the phase shift after the first internal reflection is ~45°. The gold mirror with a small incident angle practically does not change the retardation. After passing the second prism, the beam is acquiring the total phase shift of up to 90°. The kinematic mount of the small gold mirror provides the opportunity for the beam alignment inside the retarder assembly and enables the straight light propagation through the retarder.

Polarization of the transmitted light was analyzed in the rotating-analyzer configuration for multiple positions of the retarder angle with respect to a fixed value of the P_0 and P_1 polarizers. Putting P_1 parallel to P_0 in order to optimize the linear polarization of the incident beam, and set them to 45°. The $\tan\Psi$ and $\cos\Delta$ values measured on the TOPAS and Si retarders are shown in Figure 6.6 (a) and (b), respectively, along with their fitted values which are described as follows. By using

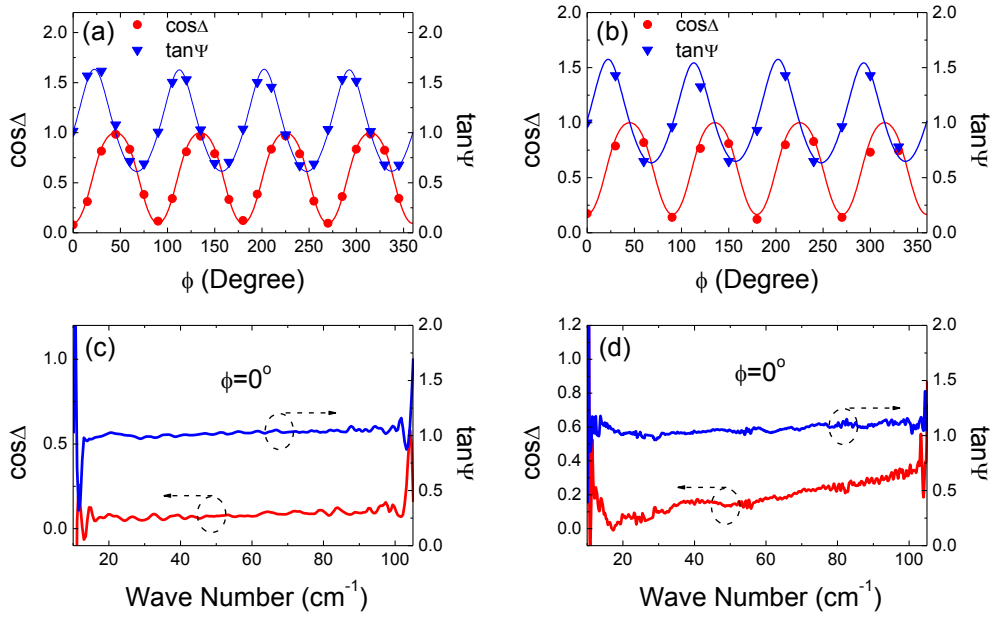

Figure 6.6 Experimental data (circles and triangles) and fit results (solid curves) for cos Δ and tanΨ as a function of the rotation angle ϕ for (a) TOPAS and (b) Si retarders. Spectral dependencies of cosΔ and tanΨ for (c) TOPAS and (d) Si retarder for ϕ=0° Characteristics look nearly ideal for the spectral range between 15 and 100 cm^{-1}.

Equation 6.2 and assuming the ideal polarizers, one can obtain the theoretical tanΨ and cos Δ when P_0=P_1=45°

$$\tan\Psi = \sqrt{\frac{(-2-2\cos 2\Psi_C(\cos 2\phi'+\sin 2\phi')-\sin 4\phi'(1-\cos\Delta_C \sin 2\Psi_c))}{(-2+2\cos 2\Psi_C(\cos 2\phi'-\sin 2\phi')+\sin 4\phi'(1-\cos\Delta_C \sin 2\Psi_c))}} \tag{6.3}$$

$$\cos\Delta = \frac{\cos\Delta_C \cos^2 2\phi' \sin 2\Psi_C + \cos 2\Psi_C \sin 2\phi' + \sin^2 2\phi'}{(1+\cos 2\Psi_C \sin 2\phi')\sqrt{1-\dfrac{\cos^2 2\phi'(\cos 2\Psi_C + (1-\cos\Delta_C \sin 2\Psi_C)\sin^2 2\phi')^2}{(1+\cos 2\Psi_C \sin 2\phi')^2}}} \tag{6.4}$$

where $\phi' = \phi - \phi_0$, the practical angle of the fast axis relative to the zero which is determined by referring to the polarizers' angles and which is off by ϕ_0 from the measured angular position ϕ. As shown in Table 6.1, the obtained the values of Ψ_C

Table 6.1 Parameters for TOPAS and silicon retarders estimated from the measure $\tan\Psi$ and $\cos\Delta$

	TOPAS retarder		silicon retarder	
	value	error bar	value	error bar
Ψ_C	44.90°	±0.27°	44.41°	±0.81°
$\tan\Psi_C$	0.997	±0.009	0.980	±0.028
Δ_C	84.66°	±0.53°	80.27°	±1.42°
$\cos\Delta_C$	0.093	±0.009	0.169	±0.024
ϕ_0	−0.1°	±0.2°	0.1°	±0.7°

($\tan\Psi_C$), Δ_C ($\cos\Delta_C$) and ϕ_0 as well as their error bars for the TOPAS and silicon retarders by fitting the measured $\tan\Psi$ and $\cos\Delta$ simultaneously with Equations 6.3 and 6.4, respectively. Notice in the Figure 6.6b that the Δ_C of the silicon retarder is estimated to be less than its practical value due to the fitting artifact. In this calculation, the experimental values for the attenuation ratio of the linear polarizers, which was measured to be less than 0.01 between 15~100 cm^{-1}, produced an insignificant correction. Otherwise, by using formulas for the rotating analyzer configuration with imperfect polarizers [63], one can simply estimate the change of the Δ_C by 0.01 of the attenuation ratio are about 0.2° for the silicon retarder and less than 0.1° for the TOPAS retarder. The ~0.997 of $\tan\Psi_C$ indicates that the TOPAS retarder is almost perfect with less than 0.5% of the difference of transmission amplitudes along the fast and slow axes, while the silicon retarder has 2% of their difference. The 84.66° of the maximum retardation is very close to 90° which was expected to obtain. According to another calculation for the retardation by using the reflection coefficients of *p* and *s* polarizations [54] separately for the TOPAS prisms and gold mirror, one can obtain about 85.3° of the resultant phase difference which is almost the same as what was obtained practically with this retarder.

Figure 6.6 (b) shows tanΨ and cosΔ for $\phi = 0°$, for which the experimental values of retardation can be obtained close to $90°$ in the frequency range which is determined by the sensitivity of the bolometer: 15 cm^{-1} – 100 cm^{-1}. At lower wave numbers, the diffraction limitations and the total decrease of the synchrotron radiation intensity make the use of the TOPAS retarders difficult. In the higher-frequency range above 100 cm^{-1}, the phonon absorption inside TOPAS results in a decrease of the transmission characteristics. The overall intensity attenuation for a single TOPAS retarder is significant and wavelength-dependent: 1:10 at 20 cm^{-1}, 1:120 at 85 cm^{-1}, which is mostly determined by the absorption due to a long optical path inside the prism material. In spite of that, the reserves of the synchrotron radiation intensity make application of these types of retarders possible for the far-IR ellipsometry.

6.4 Current Operational Setup for Full Mueller Matrix Analysis

In this section, the operation of the entire system are described. The ellipsometer uses two retarders in total. The starting conditions for light focusing are the following: the synchrotron beam is about 40×20 mm^2 and is elongated in vertical direction after exiting the FT-IR spectrometer. A single off-axis parabolic mirror in a combination with two other flat mirrors is used for the light focusing on the sample (see Figure 6.7). This beam is focused with $f\,\# = 20$. Since the light source at U4IR is diffraction-limited in the spectral range below 1000 cm^{-1}, the ellipsometer provides a relatively small spot size of about 3×3 mm^2 at the sample position without intensity-reducing apertures. A high $f\,\# = 20$ is needed to (i) minimize depolarization on the linear polarizers and retarder surfaces and (ii) minimize the uncertainty in the value of AOI. In Section 6.2, it was demonstrated

that if fast focusing with f # <10 is used, then the state of polarization after passing an optical retarder has a significant uncertainty that may result in detrimental errors in MM-SE experiments.

To support the full-Muller matrix analysis of polarization, one needs a possibility

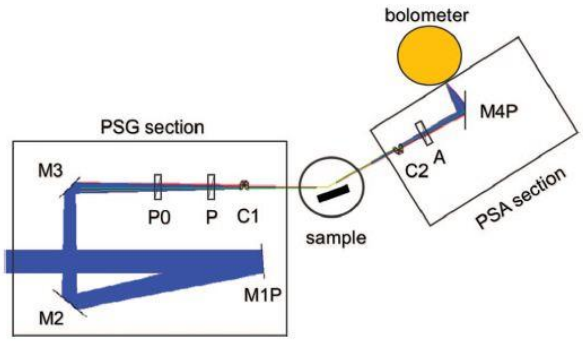

Figure 6.7 Schematics of the light propagation between the PSG and PSA sections of the ellipsometer. PSG section consists of a retarder C1, two linear polarizer, P0 and P, and three mirrors: an off-axis parabola M1P with effective focus length of 1 m and two flat ones, M2 and M3. PSA section consists of a retarder C2, analyzing polarizer A, and a parabolic mirror M4P for light focusing on a bolometer or a CuGe detector.

to obtain several linearly-independent states of polarization using both, rotating linear polarizers and rotating retarders. PSG section, as shown in Figure 6.7, is equipped with two linear polarizers and one retarder. The first linear polarizer P0 is used to attenuate and/or purify the polarization of the synchrotron radiation, which is predominantly polarized in vertical direction. The second linear polarizer P1 creates a linear polarization on the sample in RAE measurements or on the retarder in MM-SE measurements. The retarder R1 converts a linear polarization into an elliptical (or circular) polarization, which is focused on a sample. After reflection from the sample, radiation enters the PSA section. Retarders and polarizers in PSG and PSA are symmetrically positioned with respect to the sample. All linear polarizers have 25 mm clear aperture. Rotation of both,

linear polarizers and retarders is facilitated by HUBER rotational stages. To cover the broad spectral range between 20 and 4000 cm^{-1} three interchangeable sets were used:

1. Free-standing wire-grid linear polarizer from *SPECAC* are used for the frequency range between 20 and 200 cm^{-1}. The extinction ratio is between 1:2000 at low frequencies and 1:800 at high frequencies. This extinction ratio is achieved by using "tandems" in both PSA and PSG stages. Above 200 cm^{-1}, the extinction ratio for the free-standing polarizers decreases well below 1:800 due to diffraction, which is not acceptable for accurate RAE and MM-SE experiments.

2. Wire-grid polarizers on polyethylene substrates from *Tydex* are used for the frequency range between 30 and 700 cm^{-1}. The extinction ratio is also between 1:2000 and 1:800. The high-frequency cut-off is determined by absorption in the polyethylene substrates. Wire-grid linear polarizers from *SPECAC* on KRS5 substrates. The extinction ratio better than 1:800 can be achieved in the frequency range between 450 and 4000 cm^{-}

Broadband rotating retarders for the THz and far-IR spectral ranges are not commercially available. The NJIT team developed several types of rotating retarders based on triangular prisms or double Fresnel rhombs. Results of this development effort were published and repeated in previous sections. Multiple conditions have been met in this design, such as (i) a reasonably high transmission in the operating frequency range and (ii) minimal displacement of the beam caused by the 360° retarder rotation around its optical axis.

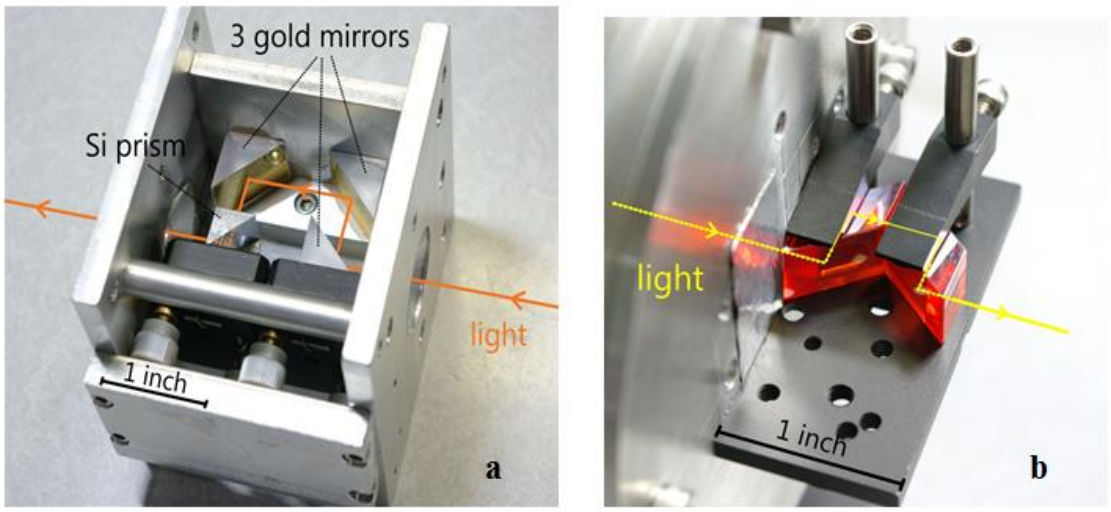

Figure 6.8 (a) rotating retarder based on a single Silicon prism and three gold mirrors (4 bounces). (b) rotating retarder based on two adjacent KRS5 Fresnel rhombs (4 internal bounces). Direction of the light propagation is shown with arrows.

3. Figure 6.8 shows two schematics for the Si prism and KRS5 double Fresnel rhomb retarders. The Si retarder is based on a single 45 degree prism with 15×15 mm^2 acceptance area and three 15×15 mm^2 gold mirrors. The maximum retardation of such retarder, which occurs inside Si due to total internal reflection, is about $\Delta \approx 95°$, which is different from the ideal theoretical value of $\Delta = \pi/4$ for a single 42 degree Si prism. Three gold mirrors practically do not change the retardation and allow to keep the light beam unchanged. Rotation of the retarder around its optical axis by 45 degree allows to change the retardation between $\Delta=0$ for linearly polarized light and $\Delta \approx 95°$ for nearly circular polarized light. The maximum values of $\Delta(\omega)$ and $\Psi(\omega)$ spectra of the Si retarder are shown in Figure 6.9. Note that due to strong multi-phonon absorption in Si prism, the spectral range between 450 and 1200 cm^{-1} is excluded from a broad 20 – 4000 cm^{-1} operational range for this Si retarder. The intensity attenuation factor for Si retarder is about 3 due to reflection and absorption in Si. The high brightness of the synchrotron

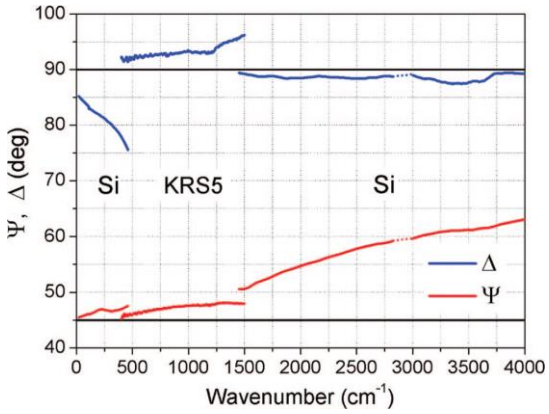

Figure 6.9 Experimental spectra for $\Psi(\omega)$ and $\Delta(\omega)$ of Si and KRS5 retarders measured for the retarder position that corresponds to the maximum value of retardation. Black horizontal lines correspond to the theoretical values for $\Psi(\omega)$ and $\Delta(\omega)$ for an ideal retarder. The narrow spectral range around 3000 cm^{-1} is shown with dotted lines due to strong absorption in the Mylar windows.

radiation is high enough to compensate these losses. In the previous sections, experimental data for an alternative design of Si retarders based on Si double Fresnel rhomb was used. In spite of its more elegant and compact design, this type of Si retarders is not implemented for MM-SE measurements due to unacceptably high displacement of the transmitted light upon the retarder rotation. Such retarder design would require either very high precision for the surface polishing or a split into two separate rhombs to facilitate their independent alignment. Note that the prism design of the Si retarder provides a much better performance compared to the TOPAS retarder described in prior sections.

To cover the spectral window between 450 and 1200 cm^{-1}, retarders based on two KRS5 Fresnel rhombs were implemented. The split design allows for the independent alignment of two rhombs that is crucial for keeping the direction of the transmitted beam unchanged upon rotation of the retarder around its optical axis. KRS5 retarders pass more than 50% of light. Among disadvantages of the KRS5 retarder is a strong dispersion of

$\Delta(\omega)$ above 900 cm^{-1}. In the near future, the current KRS5 retarders will be replaced with ZnSe or Ge rhombs that should be free from internal defects that cause a strong dispersion $\Delta(\omega)$ in KRS5.

6.5 Conclusion

To realize a full-Mueller-matrix spectroscopic ellipsometer in the IR spectral range, rotatable broadband retarders made of TOPAS plastic, Si, and KRS-5 were designed and developed based on their known or measured refractive index. The retarders made of the TOPAS plastic and Si were characterized using the rotating analyzer ellipsometry in the far-IR spectral range between 10 and 105 cm^{-1}. The characteristics of the retarders were estimated by comparing with the theoretical calculation, and then observing them working in the spectral range along with their rotations. A new far-IR Ellipsometer with a full MM capability which employs rotatable broadband retarders has been designed and installed at U4IR beamline at NSLS-BNL. The current design of the setup was discussed. A few other design features which differentiate this instrument from other far-IR ellipsometers are:

1. A broad spectral range of the instrument between 20 and 4000 cm^{-1} is facilitated by the properties of the of the synchrotron radiation (SR), which is used as a light source at U4IR beamline, NSLS-BNL, and is provided by the use of the interchangeable sets of optical polarizers, retarders, spectrometer beam splitters, and detectors. The high brightness of the synchrotron source, especially in the frequency range below 100 cm^{-1}, is crucial for the studies of relatively small crystals with an in-plane cross section area of a few mm^2.

2. The spot-size of about 3×3 mm^2 at the sample position for the slowly focused SR with f # = 20 is facilitated by the use of parabolic mirrors. Since the light source at U4IR is diffraction-limited in the spectral range below 1000 cm^{-1}, the ellipsometer provides a relatively small spot size of the focused radiation without intensity-reducing apertures.

3. The setup is equipped with several sets of rotating retarders and compensators for a broad frequency range including the far-IR that enables a full Muller matrix analysis or the samples.

CHAPTER 7

RARE-EARTH IRON GARNETS

The spectra of far-infrared transmission in $Tb_3Fe_5O_{12}$ magnetoelectric single crystals have been studied in the range between 15 and 100 cm^{-1}, in magnetic fields up to 10 T, and for temperatures between 5 and 150 K. Far-infrared spectra of ferrimagnetic $Dy_3Fe_5O_{12}$ single crystals have been studied in the spectral range between 12 and 700 cm^{-1} and in a wide temperature range between 5 K and 300 K using transmission spectroscopy and rotating analyzer ellipsometry. In $Tb_3Fe_5O_{12}$, some of the observed infrared-active excitations are attributed to electric-dipole transitions between ligand-field split states of Tb^{3+} ions. The possibility for hybrid excitations of magnons and ligand-field states and their possible connection to the magnetoelectric effect in $Tb_3Fe_5O_{12}$ is discussed. In $Dy_3Fe_5O_{12}$ the temperature range below T_C =16 K for the magnetic ordering of Dy^{3+} spins, a number of ligand field (LF) and Kaplan-Kittel (KK) exchange resonance modes have been found. Temperature dependences of their frequencies allowed us to estimate the ratio between the Fe–Dy and Dy–Dy exchange constants.

Portions of this work have been published in:

- T. D. Kang, E. C. Standard, K. H. Ahn, and A. A. Sirenko, G. L. Carr, S. Park, Y. J. Choi, M. Ramazanoglu, V. Kiryukhin, and S-W. Cheong, "Coupling between magnon and ligand-field excitations in magnetoelectric $Tb_3Fe_5O_{12}$ garnet", Phys. Rev. B **82**, 014414 (2010).

- T. D. Kang, E. C. Standard, P. D. Rogers, K. H. Ahn, and A. A. Sirenko, A. Dubroka, C. Bernhard, S. Park, Y. J. Choi and S.-W. Cheong, "Far-infrared spectra of the magnetic exchange resonances and optical phonons and their connection to magnetic and dielectric properties of $Dy_3Fe_5O_{12}$ garnet", Phys. Rev. B **86**, 144112 (2012).

7.1 Introduction

Magneto-optical effects, ferrimagnetic structure of the Fe spin sublattice, and its relationship to the huge magnetostriction in Rare Earth Iron garnets (*R*-IGs), with the chemical formula $R_3Fe_5O_{12}$, have been in the research focus for decades. [64] An interest in *R*-IGs was renewed after recent discovery of the magnetoelectric and magnetodielectric effects in Tb-IG in surprisingly low magnetic fields of less than 2 kOe. [24] Formation of the local electric polarization induced by the magnetic ordering was also observed in Tb-IG. [65] These reports were followed by far-IR spectroscopic studies of the coupling between magnons and ligand-field excitations in Tb-IG in the temperature range of ~ 70 K. [66]

Tb and Dy are the neighbors in the line of R^{3+} ions and are different by one f electron only. The electron parity change in the $4f$ orbital and different spin and g-factor values between Tb and Dy may result in a significant modification of the low-temperature magnetic and dielectric properties between Dy-IG and Tb-IG. Preliminary results for antiferroelectric (AFE) ordering in Dy-IG that occurs in the same temperature range (T< 16 K) as the ferromagnetic (FM) ordering of Dy^{3+} spins. [23] The latter was not observed in Tb-IG yet, probably due to a significantly lower transition temperature. A magnetodielectric effect revealed itself in Dy-IG at low temperatures as a relatively small increase of the static dielectric constant in a weak magnetic field of ~1 kOe (0.1 T). [23] This particular interest in R-IGs follows the mainstream of the modern studies of magnetoelectric and multiferroic materials. [67] [68] [69] [70] [71] The microscopic nature of the magnetoelectric effects can be better understood through the studies of the optical excitations such as IR active electromagnons and lattice vibrations that are

modified by the spin-lattice interaction. [50] [72] [73] [74] [51] [75] [76] [77] [78] Due to the coincidence of the temperatures for the FM ordering of Dy spins and the AFE lattice ordering in Dy-IG, it was expected that an interesting behavior for the low-frequency optical phonons, which are related to the displacements of the heaviest ions (Dy) and spin-related ligand field (LF) transitions and Kaplan-Kittel (KK) [79] magnetic exchange resonance modes in Dy-IG. The main results of this chapter are (i) the observed correlation between the magnetic field-induced changes of magnetic susceptibility $\chi(0,H)$ with the oscillator strength of the KK modes and (ii) the established *Lyddane-Sachs-Teller (*LST) relation between the static dielectric constant $\varepsilon(0,T)$ and the oscillator strength of the low-frequency optical phonons in the proximity to the AFE phase transition. It will also be shown that the peak in $\varepsilon(0,H)$ at ~1 kOe is not related to the spectra of the LF and KK modes suggesting that the magnetodielectric effect is probably driven by the magnetic-field induced changes in the spectra of the optical phonons due to magnetostriction. Also (iii), presented is a systematic study of the far-IR transmission spectra in $Tb_3Fe_5O_{12}$ in the vicinity of the critical magnetic fields and the transition temperatures. It will be argued that the tuning of the dielectric constant by temperature and magnetic field can be connected to the appearance of the hybrid modes: {magnetic + ligand field electronic excitations of Tb^{3+}}.

Recently, the importance of the low-frequency infrared-active excitations in relationship with the intriguing multiferroic effects has been understood. An electric-dipole excitation called “electromagnon” has been discovered in a number of multiferroics such as *R*-MnO_3 and $TbMn_2O_5$. [50] [51] However, the theoretical picture for electromagnons in multiferroics is still under development. [80] [81] For example, the

Dzyaloshinsky-Moriya (DM) interaction between non-collinear spins that allows coupling between magnons and electric field cannot always explain experimental data for polarization selection rules of electromagnon absorption and it is still not clear how two excitations (magnons and optical phonons) interact while being separated by hundred(s) of cm^{-1} on the energy scale. For rare earth based multiferroics R-Mn_2O_5, it was previously proposed by an alternative explanation. [82] It is based on the contribution of the forced electric-dipole transitions between the 4*f* energy levels of the R^{3+} ions to the static values of the dielectric constant. The exchange interaction between R^{3+} and Mn magnetic moments results in hybrid excitations: ligand field + magnons. Such excitations were experimentally observed in $HoMn_2O_5$. In this scenario, a spontaneous polarization that appears at the temperatures below the ferroelectric phase transition removes R^{3+} from the center of inversion thus enabling the otherwise forbidden electric-dipole optical transitions between the ligand field states of R^{3+}. This scenario will be verified below for another rare earth based magnetoelectric system: $Tb_3Fe_5O_{12}$ garnet.

7.2 Samples and Measurements

The high-temperature flux growth technique was utilized to produce bulk crystals of $Dy_3Fe_5O_{12}$ and $Tb_3Fe_5O_{12}$ [67]. The recent experimental data from Reference [23] for the static magnetic susceptibility $\chi(0,T)$ and dielectric constant $\varepsilon(0,T)$ are shown in Figure. 5.1(a,b). The dielectric constant $\varepsilon(0,T)$ was measured at a single frequency of 44 kHz for a sample with the (0 1 1) plane. Other $Dy_3Fe_5O_{12}$ samples from the same batch with the (0 0 1) and (1 1 1) planes, a cross section area of 5×5 mm^2, and different thickness of 0.19 and 0.50 mm were used for the optical experiments: transmission and rotating

analyzer ellipsometry (RAE). The $Tb_3Fe_5O_{12}$ samples had a typical cross section area of about 4×4 mm^2 and different thickness in the range between 0.3 and 0.6 mm were and used for the light transmission experiments only. The opposite sides of the sample were polished and wedged with a ~3° offset in order to suppress interference fringes. Transmission spectra were measured with the resolution of 0.3 cm^{-1} in the spectral range between 13 and 100 cm^{-1} at the National Synchrotron Light Source, Brookhaven National Laboratory, at the U4IR and U12IR beamlines equipped with a Bruker IR spectrometer, and a LHe-pumped (~1.4 K) bolometer. The spectral resolution of 0.3 cm^{-1} was chosen to be significantly smaller than the typical width of the absorption lines of about 2 cm^{-1}. A magnetic field of up to 100 kOe (10 T) was applied to the sample along the light propagation direction (Faraday configuration) inside of an Oxford optical cryostat. Polarization of the transmitted light was scrambled by the light cone and was not analyzed. For each sample the raw data of transmitted intensity were normalized to transmission through an empty aperture with the size equal to that of the sample. The rotating analyzer ellipsometry (RAE) measurements of the optical phonons were carried out at Fribourg University. The RAE experimental setup is similar to that described in Reference. [83] A conventional Hg lamp was used as a light source. Spectra of optical phonons in Dy-IG have been measured in the temperature range between 8 and 300 K in the spectral range between 70 and 690 cm^{-1} and resolution of 0.7 cm^{-1} using a single value for the angle of incidence (AOI) of 75°. Additional RAE measurements of the same sample have been carried out at room temperature in the energy range between 0.75 eV and 5.9 eV using Woollams spectroscopic ellipsometer at the Center for Functional Nanomaterials, Brookhaven National Laboratory.

7.3 Far-IR Excitations in *R*-IG

Far-IR spectra of magnetic excitations in *R*-IG (*R*= Sm, Gd, Ho, Er, and Yb) have been studied more than 40 years ago by Sievers and Tinkham. [84] [85] Yamomoto et al. studied far-IR spectra for Dy-IG and Tb-IG. [86] It appeared that Dy-IG has the most complex spectrum of the far-IR excitations among all other studied R-IGs. Based on the analysis of transmission in polycrystalline materials it was shown that below 80 cm^{-1} the optical spectra of *R*-IGs are dominated by both R^{3+} single ion electronic transitions and KK modes. Note that in all earlier studies of the far-IR excitations in *R*-IG it was assumed that the optical transitions inside the 4*f* shell are magnetic dipoles, as expected for a free R^{3+} ion or for an R^{3+} ion at the center of inversion. [79] [84] [85] [86]

Synchrotron radiation spectroscopy allows data collection in a broader range of external parameters, such as external magnetic fields and low temperatures. As is shown in this section, the advanced spectroscopic capabilities enable observation of effects that were not detectable in the earlier experiments with polycrystalline *R*-IG samples carried out with a lower spectral resolution. Recent studies of *R*-IG show that at low temperatures the local electric polarization removes the R^{3+} ions from the position at the center-of-inversion. [65] [23] This result is important for interpretation of the selection rules for the optical transitions between the 4*f* electronic levels of Dy^{3+}. In the non-centrosymmetric environment, the so-called "forced electric-dipole" optical transitions are allowed in addition to the conventional magnetic-dipole transitions. [87] The study of the far-IR excitations in Tb-IG researchers observed a coupling between magnons and ligand field electronic excitations of Tb^{3+} and suggested that the tuning of the dielectric constant by temperature and magnetic field can be connected to the appearance of the

hybrid magneto-electric modes. [66] In contrast, in the Dysprosium study, a stronger connection between the static dielectric constant and the spectra of the optical phonons have been found (see Section 7.7). Also, an observation of hybridization between electric- and magnetic-dipole activity for the ligand-field excitations, have been reported [23]. In this chapter previously determined type of the dipole activity for the LF and KK modes from Reference [23] will be relied upon and will focus on the temperature and magnetic field changes of the frequency and oscillator strength for the LF and KK modes in connection with the changes of the static dielectric constant $\varepsilon(0,T,H)$ and magnetic susceptibility $\chi(0,T,H)$.

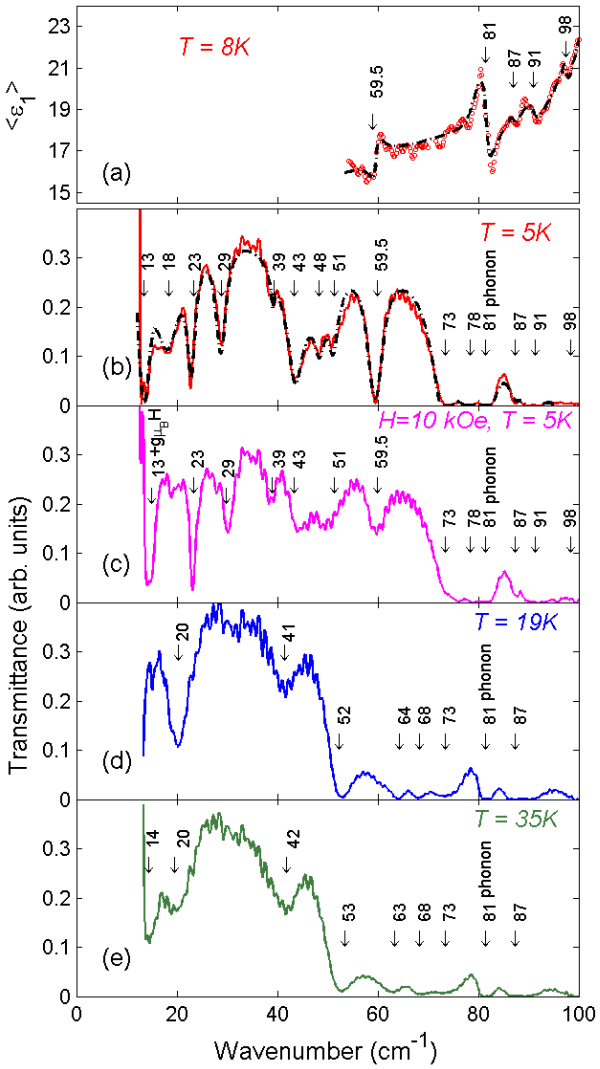

Figure 7.1 (a) Far-IR ellipsometry spectrum for the real part of the pseudo-dielectric function for $Dy_3Fe_5O_{12}$ single crystal that is dominated by the optical phonon at 81 cm^{-1}, a magnetic dipole excitation at 59.5 cm-1, and three hybrid modes at 87, 91, and 98 cm^{-1}. (b) Far-IR transmission spectra for the same sample with the thickness of d=0.50 mm measured in a zero external magnetic field at T = 5 K, (c) T=5 K and H=10 kOe, (d) zero field and T=19 K, and (e) 35 K. The light propagation for transmission spectra is along the [100] direction. Arrows indicate the frequencies of the IR-active absorption lines.

Figure 7.1(a-e) shows far-IR ellipsometry data for the real part of a pseudo-dielectric function $\langle \varepsilon_1 \rangle$ at T = 8 K and several transmittivity spectra measured at T = 5, 19, and 35 K for the Dy-IG sample with the thickness d=0.50 mm. The major oscillator

modes in $\langle \varepsilon_1 \rangle$ and absorption minima, which correspond to the IR-active modes, are marked with arrows in Figure 7.1(a-e). Several spectral modes in the frequency range between 70 and 100 cm^{-1} [see in Figure 7.1(b,c,d,e)] are saturated due to strong absorption in a relatively thick sample with d=0.50 mm. To improve sensitivity of the position of the saturated peaks, the same Dy-IG sample was polished down to the thickness of d=0.19 mm and the transmission measurements were repeated. The corresponding transmission intensity spectra Tr.(T) for T= 4 K and T= 300 K are shown in Figure 7.2(a). All modes that were saturated in Figure 7.1(b) can be clearly seen in Figure 7.2(a). The high temperature spectra Tr.(T) measured for T > 200 K have only one absorption mode that corresponds to lowest frequency optical phonon at 80 cm^{-1}. The contribution of this optical phonon to the room temperature spectrum Tr.(300 K) corresponds to the signal below the blue dashed line in Figure 7.2(a). The room temperature spectrum without the optical phonon contribution was used for normalization of the transmission intensity measured at low temperatures in Figure 7.2(b) and 7.3(b). The corresponding spectra of Tr.(T) / Tr.(300 K) measured at T= 4, 12, 18, and 23 K are shown in Figure 7.2(b). The absorption peaks are marked with arrows. To illustrate the temperature-induced evolution of the transmittivity spectra of the thick sample (d=0.50 mm) and that for the normalized transmission spectra of the thin sample (d=0.19 mm) the two-dimensional (2D) intensity maps in Figure 7.3(a,b) are presented, which were measured with the temperature increments of 1 K. Positions of all absorption peaks measured with both, ellipsometry and transmission techniques, are summarized in Figure 7.3(c).

The lowest frequency IR-active optical phonon at 81 cm^{-1} is visible in the whole measured temperature range in both, ellipsometry [Figure 7.1(a)], transmittivity spectra [Figure 7.1(b,c,d,e)], and normalized transmission spectra in Figure 7.2(a,b). Its properties along with that for all other optical phonons will be discussed in Section 7.6. For relatively high temperatures $T \geq 20$ K, only a few single-ion crystal-field (CF) electronic transitions of Dy^{3+} at about 20, 53, 63, 71 (doublet), and 87 cm^{-1} can be seen in

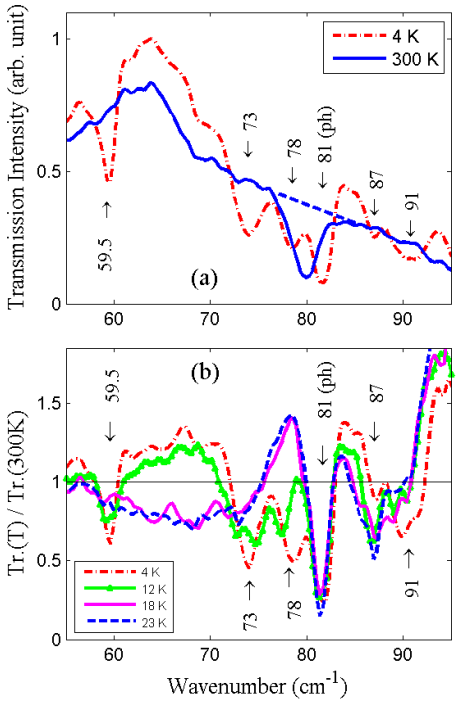

Figure 7.2 (a) Far-IR transmission spectra Tr.(T) for $Dy_3Fe_5O_{12}$ sample with d=0.19 mm measured in a zero external magnetic field at T = 4 K (red) and T=300 K (blue) . Dashed blue line shows the contribution of the optical phonon at 80 cm^{-1} to the transmission intensity at T=300 K. (b) Spectra of the transmission intensity Tr.(T), which were measured at T= 4, 12, 18, and 23 K and normalized by that measured at T=300K: Tr.(T)/ Tr.(300 K). The arrows in (a) and (b) show the position of the LF, CF, and KK absorption lines and the phonon (ph) for T = 4 K. The corresponding transition frequencies in cm^{-1} are shown next to the vertical arrows.

Figure 7.3(a,b), where the corresponding absorption lines are marked as CF1, CF2, CF3, CF4, and CF5. The nearly temperature-independent frequencies of these lines are typical for CF transitions. Similar energies of the CF transitions of Dy were reported for other garnets. For example, in Y-Ga-garnet the lowest crystal-field transitions of Dy impurities are at 20.5, 71, and 117 cm^{-1}. [88] The intensity of the CF absorption lines increases with the temperature decrease and the lines become narrower. This behavior is typical for CF transitions due to the effects of the thermal re-population of the CF levels of Dy^{3+} and interaction between 4*f* electronic states and acoustic phonons. The CF1 line at 20 cm^{-1} [Figure 7.3(a)] becomes very weak for $T > 40\,\mathrm{K}$ due to thermal population of the first excited CF1 level for the temperature range with $k_B T$ exceeding the splitting between the ground and CF1 levels (~20 cm^{-1}). In the temperature range between 16 K and 55 K, the CF4 line at ~71 cm^{-1} splits into two lines at 68, and 73 cm^{-1}, which are separated by about 5 cm^{-1} [see Figure 7.1(d,e) and Figure 7.3(a)]. This splitting is most likely related to the rhombohedral distortion of the garnet lattice that appears in the same temperature range. [89] Section 7.6 discusses similar changes in the spectra of optical phonons, which are induced by the same rhombohedral distortion. The weak and broad absorption line at 42 cm^{-1} appears for T> 20 K and is probably due to the optical transition between the excited CF levels, such as CF1 and CF3. Similar interpretation may be used to explain a relatively weak absorption line at 14 cm^{-1} for T> 20 K. This energy is close to the distance between CF2 (53 cm^{-1}) and one of the CF4 components at 68 cm^{-1}. An additional support for this interpretation of the optical transitions at 14 and 42 cm^{-1} can be found in the magnetic field dependencies of the transmission spectra (see

Section 7.4 for details). The line at 42 cm^{-1} disappears as soon as CF1 and CF2 levels split in the external magnetic field at T=25 K.

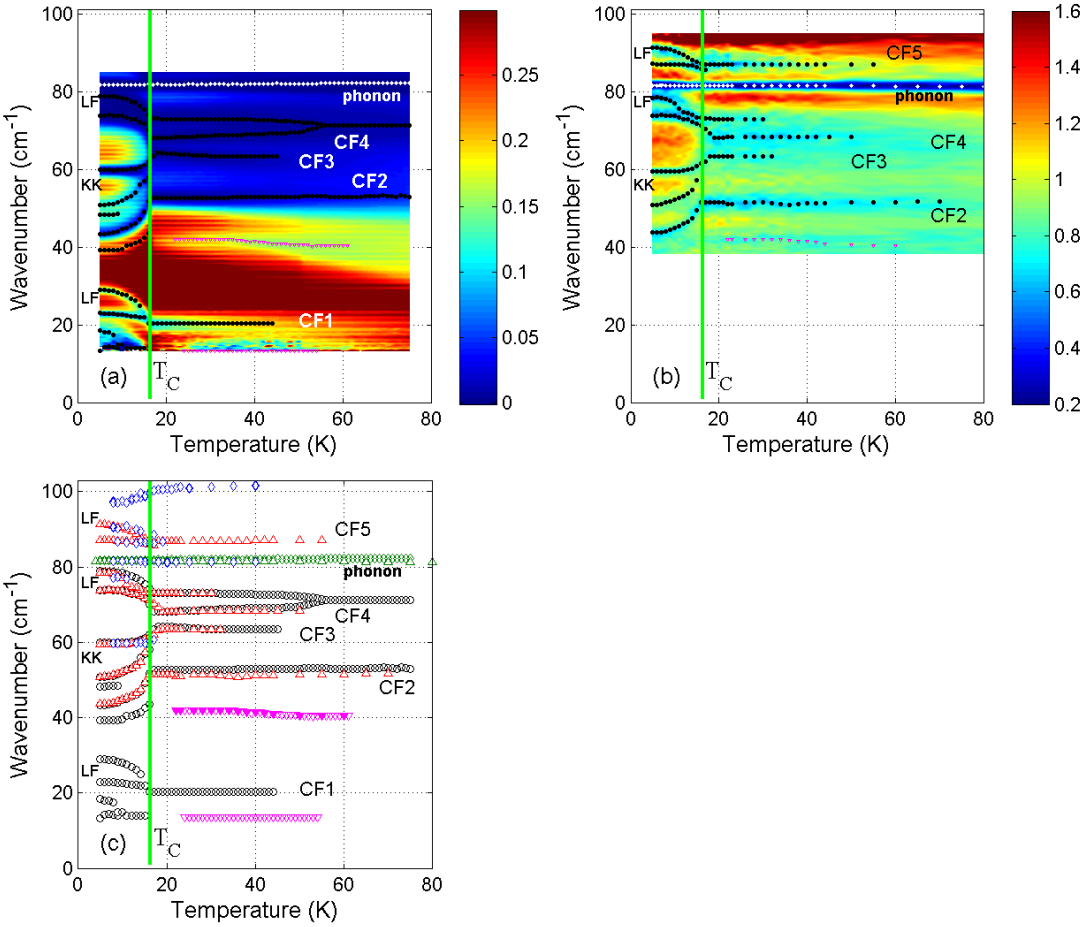

Figure 7.3 (a) Transmittivity map *vs.* temperature and light frequency for $Dy_3Fe_5O_{12}$ sample with the thickness d = 0.50 mm. The transmittivity scale is between 0 and 0.3. (b) Normalized transmission intensity Tr.(T)/Tr.(300 K) *vs.* temperature and light frequency for the same crystal as in (a) polished down to d = 0.19 mm. The normalized Tr.(T)/Tr.(300 K) scale is between 0.2 and 1.6. In both, (a) and (b), the blue (dark) color corresponds to stronger absorption and red (light) color indicates high transmission. The vertical green line represents the phase transition temperature T_C = 16 K. The white dots represent the phonon frequency at 81 cm^{-1}. Positions of the LF, CF, and KK modes are shown with black dots. (c) Frequencies of the LF, KK, and CF modes *vs*. temperature. Data from (a) are represented by black circles, data from (b) are represented by red triangles. The green symbols represent the phonon at 81 cm^{-1}. The magenta triangles at 14 cm^{-1} and 42 cm^{-1} correspond to the optical transitions between the thermally excited CF levels: CF2→CF4 and CF1→CF3. The ellipsometry data for the LF transition and the phonon at 81 cm^{-1} are shown with blue diamonds.

The transmission spectra for the temperature range below the phase transition for the FM order of Dy^{3+} spins at $T_C = 16$ are more complex [see Figure 7.1(b,c), Figure 7.2(a,b), and Figure 7.3(a,b)]. This phase transition is evident by the opening of the transparency window between 50 and 70 cm^{-1} and by a strong shift of several absorption lines away from this spectral range. For identification of the IR absorption lines, terms that are originated from the work by Kittel et al. in Reference [79] will be used. The observed far-IR absorption lines will be attributed either to the so-called Kaplan-Kittel (KK) modes or to LF exchange resonances. In the following discussion of the spectra measured for $T < T_C$, the term LF replaces CF to underline the importance of the strong exchange interaction between the ordered Dy and Fe spins which should be considered in addition to the primarily electrostatic CF interaction.

For T=5 K, a number of the LF exchange resonances, and KK modes appear at 13, 18, 23, 29, 39, 43, 48, 51, 59.5, 73, 78, 87, 91, and 98 cm^{-1} [Figure 7.1(b,c) and Figure 7.2(a,b)]. The transmission spectra as well as the ellipsometry spectra were fitted using a multi-oscillator dielectric model. The results of the fit are shown in Figure 7.1(a,b) along with the experimental spectrum. Temperature dependence of the oscillator frequencies obtained from the fit is shown in Figure 7.3(a,b,c). In a zero magnetic field, the lowest-frequency absorption line at 13 cm^{-1} is very close to the edge of the measurable spectral window. However, this absorption line shifts to higher frequencies in an external magnetic field, which enables its clear identification. Figure 7.1(c) shows such a spectrum measured in a weak magnetic field of 10 kOe, where the peak formerly at 13 cm^{-1} shifts up by about 1.2 cm^{-1}. The complete magnetic field dependence of this absorption peak is shown in Figure 7.4(a,b) and will be discussed in Section 7.4. The

mode at 13 cm^{-1} is interpreted as due to a spin-splitting of the ground state of Dy^{3+} ions. Several other modes at 73, 78, 87, 91, and 98 cm^{-1} are difficult for identification in the transmission spectra for thick sample (d=0.50 mm) due to significant absorption saturation in this spectral range. These peaks are much better resolved in the spectra measured for the thin sample (d=0.19 mm) shown in Figure 7.2(a,b). In addition, the transmission spectra have been compared with the ellipsometry data for the same sample, where the oscillators at 87, 91, and 98 cm^{-1} are seen more clearly in the spectrum for $\langle \varepsilon_1 \rangle$ [Figure 7.1(a)]. The modes at 73 and 78 cm^{-1} have a hybrid, or simultaneous magnetic- and electric-dipole activity, thus becoming quite weak in ellipsometry spectra [see Reference [23] for more details]. The other group of modes at 39, 43, 51, and 59.5 cm^{-1} is in the center of the measured spectral range that allows for a very accurate measurement of their frequencies. The mode at 48 cm^{-1} is very weak disappearing for T>10 K that prevents its further interpretation.

The groups of KK modes at 39, 43, 51, 59.5 cm^{-1} and LF modes at 18, 23, 29, 73, 78, 87, and 91 cm^{-1} are marked in Figure 7.3(a,b). The LF and KK modes can be distinguished based on their opposite temperature dependence: softening of the KK frequency and hardening of the LF frequency upon cooling down from T_C. Below is discussed the main contributions, such as the total magnetization of the ordered Dy spins, to the temperature variation of the KK and LF frequencies and will estimate the parameters of the exchange interaction between Fe and Dy spins.

In a simplified model for a two-spin ferrimagnetic system, like *R*–Fe, an exchange-type KK mode is expected with the frequency Ω_M. Another mode Ω_{LF} corresponds to precession of the Dy moments in the effective field imposed by the iron

magnetization due to the superexchange interaction between Fe and R^{3+} ions. According to References [79] and [85], the zone-center frequencies of these modes can be estimated in the simplified model for two interacting spins:

$$\Omega_{\mathrm{M}}(\mathrm{T}) = \lambda_{\mathrm{Fe-Dy}}\mu_{\mathrm{B}}\left[\mathrm{g_{Dy}M_{Fe}} - \mathrm{g_{Fe}M_{Dy}(T)}\right] \quad (7.1)$$

$$\Omega_{\mathrm{LF}} = \lambda_{\mathrm{Fe-Dy}}\mu_{\mathrm{B}}\mathrm{g_{Dy}M_{Fe}} \quad (7.2)$$

where μ_B is the Bohr magneton ($\mu_B \approx 0.04669$ cm^{-1}/kOe), λ_{Fe-Dy} is the exchange constant between Fe and Dy ions, $g_{Fe} = 2$ and g_{Dy} are the corresponding g-factors, $M_{Dy}(T)$ is the Dy-sublattice magnetization, and M_{Fe} is the combined Fe magnetization for *a* and *c* sites. When temperature decreases below $T_C = 16$ K, the KK modes exhibit softening of the frequency $\Omega_M(T)$ due to increase of the Dy magnetization $M_{Dy}(T)$. Note that $M_{Dy}(T)$ is zero for $T > T_C$ and frequencies of the KK and LF modes should coincide in this case with that for an unperturbed CF transition energy. Figures 7.1(b) and 7.3(a,c) show three KK modes at 39, 43, and 51 cm^{-1}, that can be explained by the presence of two types of Dy spins in the double umbrella structure and by the strongly anisotropic and temperature-dependent superexchange interaction between Dy and Fe ions. The mode at 59.5 cm^{-1} seems to be nearly temperature independent up to ~14 K. However, between 14 and 16 K this mode also increases the frequency by a few cm^{-1}, thus showing a typical KK-type behavior at the phase transition.

The temperature-induced variation of the frequency for the KK modes mode below 16 K is equal to $\Delta\Omega_M(T) = -\lambda_{Fe-Dy} g_{Fe} \mu_B M_{Dy}(T)$, which is proportional to magnetization of Dy spins. The shape of the curves for $\Omega_M(T)$ in Figure 7.3(c)

corresponds to a phase transition with appearance of the long range ordering of Dy spins below $T_C = 16$ K, rather than a gradual change as expected for a paramagnetic (PM) moment in the effective field. The relatively sudden appearance of Dy magnetic phase below 16 K indicates that the Dy–Dy exchange interaction energy is not small compared to that for Fe–Dy exchange, possibly due to the large and anisotropic g-factor of Dy ions g_{Dy}. The literature values of the diagonal g_{Dy} tensor components are {11.07, 1.07, 7.85}, two of which are significantly larger than that for the ${}^6H_{15/2}$ free-ion ($g_{{}^6H_{15/2}}$=4/3). [89] Note that such a difference is common in *R*-IGs, where the *J*-mixing and repopulation of the CF states at low temperature modify the effective g-factor, making it strongly anisotropic.

Three groups of LF modes, centered above 20, 70, and 90 cm^{-1} have a trend that is opposite to that for the KK modes with their frequencies decreasing with the temperature increase between 5 and 16 K. This trend is not typical for single ion transitions in the effective field produced by Fe ions, which predicts a temperature independent behavior for Ω_{LF} in Equation 7.1. Note that the observed $\Omega_{LF}(T)$ is similar to the temperature dependence of the exchange mode previously measured in another *R*-IG: $Er_3Fe_5O_{12}$. [84] As inferred from the shape of $\Omega_{LF}(T)$ in Figure 7.3(c) for several LF modes above 20, 70, and 90 cm^{-1}, their temperature dependence should be also influenced by the Dy–Dy exchange interaction. By representing the exchange interaction between Dy^{3+} ions with the FM exchange constantλ_{Dy-Dy}, Sievers and Tinkham derived the expression for the temperature dependent LF energies. [84]

$$\Omega_{\mathrm{LF}}(\mathrm{T}) = \mathrm{g_{Dy}}\mu_{\mathrm{B}}\left[\lambda_{\mathrm{Fe-Dy}}\mathrm{M_{Fe}} + \lambda_{\mathrm{Dy-Dy}}\mathrm{M_{Dy}}(\mathrm{T})\right] \quad (7.3)$$

which should replace Equation 7.2 for materials with a strong FM exchange constant λ_{Dy-Dy}. The temperature dependent part of the LF mode frequency is $\Delta\Omega_{LF}(T) = \lambda_{Dy-Dy} g_{Dy} \mu_B M_{Dy}(T)$, which has the opposite sign compared to $\Delta\Omega_M(T) = -\lambda_{Fe-Dy} g_{Fe} \mu_B M_{Dy}(T)$ for the KK modes. Although it is known that the exchange constant between iron and rare earth ions is significantly larger than that for Dy–Dy interaction, [89] a relatively large value of g_{Dy} compared to $g_{Fe} = 2$ can make $|\Delta\Omega_{LF}(T)|$ comparable to $|\Delta\Omega_M(T)|$ in Dy-IG. The strong anisotropy of the g-factor tensor for Dy explains why more than one absorption line $\Omega_{LF}(T)$ is observed for each CF energy level above 20, 70, and 90 cm^{-1}. From the comparison between the changes of the LF excitation frequencies $\Delta\Omega_{LF}(5K) = 7$ cm^{-1} and $\Delta\Omega_M(5K) = -10$ cm^{-1} with respect to their values for $T \approx T_C$, one can estimate the ratio of the coupling constant for Dy–Fe and Dy–Dy interactions. Then taking the literature values of $g_{Dy} \approx 11$ and $g_{Fe} = 2$, one obtains $\lambda_{Dy-Dy}/\lambda_{Fe-Dy} = 0.13$. This estimate does not take into account possible Fe spin re-orientation. [25] A more elaborate theoretical model may be needed to include temperature dependence of M_{Fe} below 16 K.

Note, that according to the simplified model for collinear Dy^{3+} and Fe^{3+} spins, which was developed in Reference [79] and [85] for *R*-IGs, the KK and LF exchange-resonance modes are collective excitations of Dy^{3+} and Fe^{3+} spins with spatial dispersion. On one hand, they can be viewed as pure magnons which contribute only to the magnetic permeability $\mu(\omega)$. [85] In Reference [23], shows previously studied the type of the dipole activity of the LF and KK modes experimentally using a combination of several optical techniques: Transmission and Reflectivity at normal incidence, and RAE. It turns out that the KK modes are primarily magnetic dipoles, while the LF modes

have a hybrid, or a simultaneous electric- and magnetic-dipole activity. Thus the LF modes can contribute to both static values of $\varepsilon(0)$ and $\mu(0)$. The electric dipole activity of the LF modes originates primarily from their proximity to the frequencies of the optical phonons the lowest of which is at 81 cm^{-1}. The following section discusses spectra of the KK and LF modes in external magnetic field.

7.4 $Dy_3Fe_5O_{12}$ (Exchange Magnetic Resonances and Optical Phonons)

7.4.1 Strong Magnetic Field

Figure 7.4(a) shows maps of the transmission intensity vs. magnetic field for T= 4.5 K. The frequencies of the phonon, KK and LF modes are shown in Figure 7.4(b). As expected, the lowest optical phonon at 81 cm^{-1} does not change its frequency in the external magnetic field. In contrast, a strong magnetic field H applied along [1 0 0] direction in the Faraday configuration causes an increase of the KK and LF frequencies. In the high-field regime, this effect can be described by the effective g-factors as follows: $\Omega(H) = \Omega(0) + g\mu_B H$, where μ_B is the Bohr magneton ($\mu_B \approx$ 0.04669 cm^{-1}/kOe). The corresponding slope $\partial\Omega(H)/\partial H = g\mu_B$ for the lower-frequency transitions at 13 cm^{-1} is close to $3.5\mu_B$, while for the higher frequency modes the slope is about $6.5\mu_B$ [see Figure 7.4(b)]. One can compare these values to the effective g_{Dy} tensor components for Dy^{3+} in Dy-IG: {g_x=11.07, g_y=1.07, g_z=7.85}, which were measured in the $x-y-z$ coordinate system aligned with respect to the magnetization direction for Fe spins. [89] For this experiment, where H is applied along the [1 0 0] crystallographic direction, the corresponding g-factors have to be recalculated based on these literature values of g_{Dy}.

By applying this coordinate rotation for the g-factor tensor, obtained the modified slope values of $3.6\mu_B$ and $5.7\mu_B$ for magnetic field along [1 0 0]. These numbers are reasonably close to the experimental results in Figure 7.4(b): $3.5\mu_B$ and $6.5\mu_B$.

In the temperature range above the Dy FM phase transition T >16 K, the number

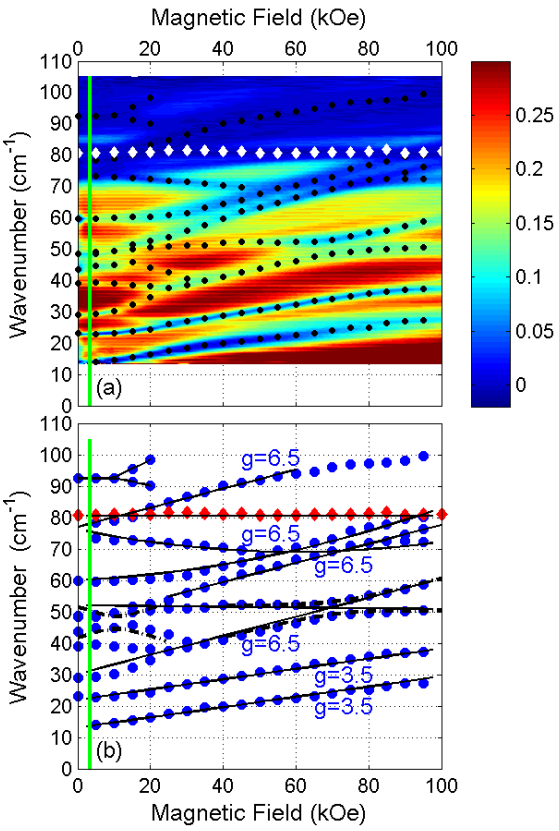

Figure 7.4 (a) Transmission map *vs.* magnetic field and light frequency for $Dy_3Fe_5O_{12}$ at T =4.5 K and H ‖ [100]. The blue (dark) color corresponds to stronger absorption while red (light) color indicates high transmission. The transmission intensity scale is between 0 and 0.3. The green vertical line represents the critical field at H_C = 3.5 kOe. The white diamonds represent the phonon at 81 cm^{-1}. (b) Frequencies of the optical transitions *vs.* magnetic field. The linear slopes are characterized by the *g*-factor values shown next to the lines. The red diamonds represent the phonon at 81 cm^{-1}.

of the IR-active modes decreases compared to that at low temperatures. The corresponding magnetic field dependence of transmission is shown in Figure 7.5(a,b) for

T=25 K. There are two groups of absorption lines in the diagram. At zero magnetic field, one group of lines originates from the CF1 level at 20 cm^{-1}, and another one originates from CF2 level at 53 cm^{-1}. Each group of lines consists of three modes that have the slope values of about zero, $5.5\mu_B$, and $9.5\mu_B$, respectively. Thus, the temperature maps shown in Figure 7.3(a) and the magnetic field maps in Figure 7.4(a) and 7.5(a) can be qualitatively reconciled as follows. At zero magnetic field and high temperature, the low-frequency part of the spectrum is dominated by the CF lines at 20 and 53 cm^{-1}. Each line is a multiplet with the effective g-factor values of about zero, 5.5, and 9.5. Upon zero-field-cooling through the phase transition at $T_C = 16$ K, the CF1 and CF2 modes at 20 cm^{-1} and 53 cm^{-1} split into several LF lines. For example, the low-frequency one at 20 cm^{-1} splits into two modes at 22 and 29 cm^{-1} [see Figure 7.3(a,c)] with g-factors of 3.5 and 6.5, respectively [see Figure 7.4(a,b)]. The effective magnetic field values that cause the corresponding frequency shift by 2 and 9 cm^{-1} are $H_{ef1} = 12$ and $H_{ef2} = 30$ kOe. In turn, these values of the effective magnetic field correspond to the LF contribution to the CF caused by the Dy–Dy ordering below 16 K. Note that due to the strong temperature dependence of g_{Dy}, this estimate is applicable to the low temperatures only.

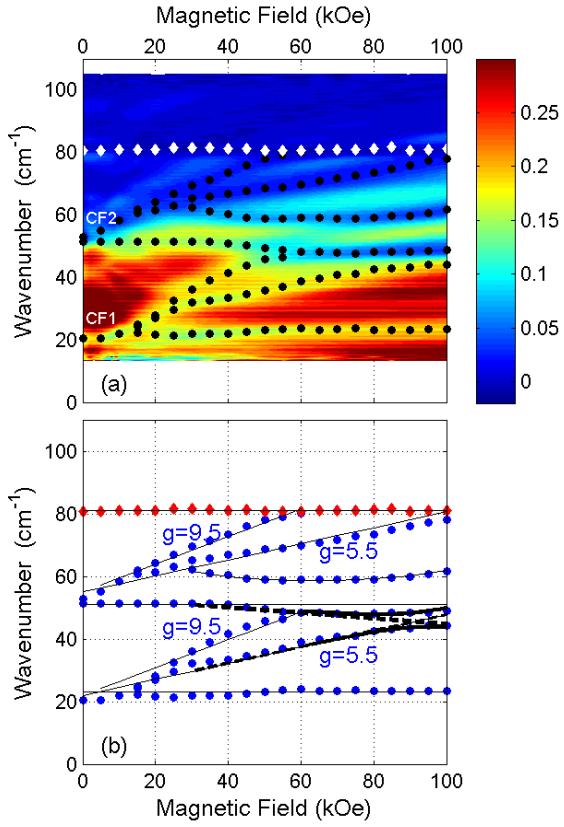

Figure 7.5 (a) Maps of the normalized transmitted intensity *vs.* magnetic field and frequency for $Dy_3Fe_5O_{12}$ at T =25 K and $H \parallel$ [100]. The blue (dark) color corresponds to stronger absorption while red (light) color indicates high transmission. The transmission intensity scale is between 0 and 0.3. The white diamonds represent the phonon at 81 cm^{-1}. (b) Frequencies of the optical transitions *vs.* temperature. The linear slopes are characterized by the g-factor values shown next to the lines.

7.4.2 Weak Magnetic Field

Figure 7.6(a) shows the magnetic field dependence of the quasi-static value of the dielectric constant. Reported recently in Reference [23], $\varepsilon(0, H)$ has a peak at $H = 1$ kOe at T=5 K. For higher magnetic field, $\varepsilon(0, H)$ slowly decreases with H. This dependence is invariant with respect to the sign of external magnetic field. The magnetization curve

which is shown in Figure 7.6(b), has a pronounced step in the same range of magnetic field. The following discusses the connection between $\varepsilon(0,H)$ and the far-IR excitations, i.e., LF and KK modes.

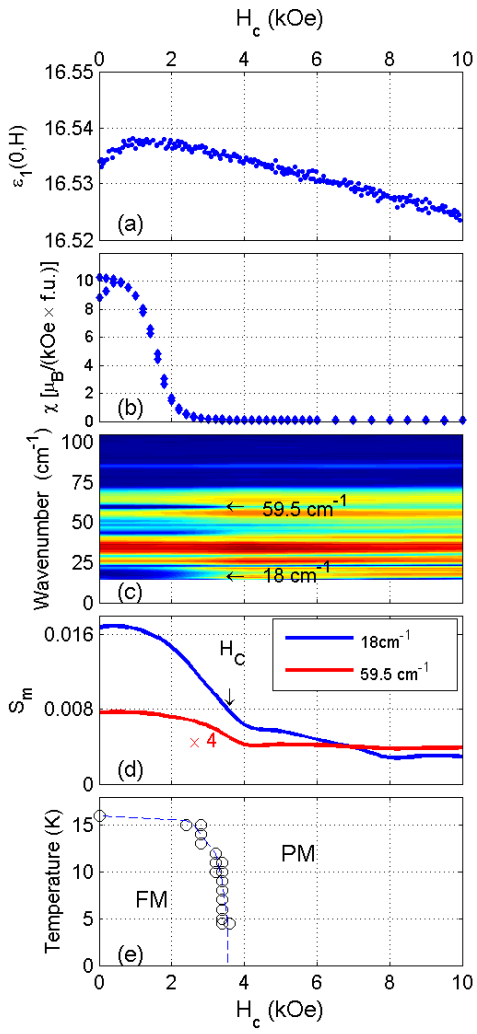

Figure 7.6 (a) Magnetic field dependence of the static dielectric constant at T= 5 K, E || [1 0 0] and H || [0 1 1]. (b) Magnetization curve with a small splitting at low field due to initial magnetization. (c) Transmission map *vs.* magnetic field and light frequency for $Dy_3Fe_5O_{12}$ at T = 4.5 K and H ‖ [100]. The blue (dark) color corresponds to stronger absorption while red (light) color indicates high transmission. The transmission intensity scale is between 0 and 0.3. (d) Oscillator strength *vs.* magnetic field. The critical field is marked with arrow. (e) The FM-PM phase diagram based on the values of the oscillator strength *vs.* T–H.

Figure 7.6(c) shows a transmission intensity map for weak magnetic fields at T=4.5 K. The effective oscillator strength $S_T(H)$ for the LF mode at 18, and KK modes at 43, 51, and 59.5 cm^{-1} decreases strongly when the field exceeds ~3.5 kOe, while the modes at 22, 29, 73, and 78 cm^{-1} remain practically unchanged. Modification of the oscillator strength for the modes at 18 and 59.5 cm^{-1} is shown in Figure 7.6(d), where the value of the critical field $H_C = 3.5$ kOe corresponds to the inflection point for $S_T(H)$. In the vicinity of the phase transition at $T_C = 16$ K, the critical field depends on the sample temperature. The phase diagram that is based on the oscillator strength dependence on the field and temperature, $S_T(T, H)$ is shown in Figure 7.6(e) for the modes at 18 and 59.5 cm^{-1}. The low-left corner is assigned to the FM phase for Dy–Dy spins, while the PM phase is in the upper-right section for high temperatures and high magnetic fields.

In principle, the magnetic-field-induced variation of the oscillator strength $S_T(T, H)$ for the KK and LF modes can contribute to the static values of $\varepsilon(0)$ or $\mu(0)$ depending on the dipole activity of each mode. Reference [23] demonstrated how a combination of the Reflection and Transmission techniques can be used to identify the dipole activity of the IR-active modes. The effective oscillator strength of the modes of the hybrid activity determined from transmission experiments is $S_T \approx \mu_\infty \cdot S_e + \varepsilon_\infty \cdot S_m$, where ε_∞ and μ_∞ are the high-frequency values and $S_{e.m}$ are the true values of the oscillator strength for the electric and magnetic components of the hybrid modes. Naturally, $\mu_\infty \cong 1$, while $\varepsilon_\infty \cong 17$ for Dy-IG in the frequency range below all optical phonons (< 80 cm^{-1}). [23] From the previous studies of Dy-IG, [23] the KK mode at 59.5 cm^{-1} in Figure 7.1(b) is a pure magnetic dipole contributing only to $\chi(0, T)$ shown in Figure 5.1(a). The type of dipole activity for other lower-frequency modes (below 55 cm^{-}

[1]) was not determined in Reference [23] due to their insufficient intensity in the reflectivity experiments. Since the oscillator strength contribution of the modes at 18, 43, and 51 cm^{-1} between $\varepsilon(0)$ and $\mu(0)$ cannot be unambiguously separated, the indirect reasons can be utilized for identification of their dipole activity. On one hand, the $\varepsilon(0,H)$ dependence shown in Figure 7.5(a) does not directly correlate with the oscillator strength of the LF modes at 18, 43, and 51 cm^{-1}. On the other hand, the magnetic field dependence of the sample magnetization, which is presented in Figure 7.5(b) in terms of $\chi(H) = \partial M(H)/\partial H$, correlates well with the magnetic-field induced decrease of the oscillator strength for the modes at 18, 43, 51, and 59.5 cm^{-1}. Thus, one can conclude that the LF mode at 18 and KK modes at 43, and 51 cm^{-1} are predominantly magnetic, the same as the KK mode at 59.5 cm^{-1}. The oscillator strength change for those magnetic modes is shown in Figure 7.6(d) in the units of S_m that are related to the static value of $\mu(0,H)$ as follows: $\mu(0,H) = 1 + \chi(0,H) = 1 + \sum_i^N S_{m,i}(H)$, where summation is taken for N magnetic modes. Thus it is concluded that the oscillator strength changes S_m are associated with the FM-PM phase transition at 3.5 kOe rather than with the AFE behavior for $\varepsilon(0,T)$ in Figure 5.1(b).

Reference [23] demonstrated that the modes at 73, 78, and 91 cm^{-1} are of a hybrid origin, possessing both electric and magnetic dipole activities. However, these modes, which could contribute directly to the change of $\varepsilon(0,H)$ in Figure 7.6(a), did not show any appreciable change of their frequency or their oscillator strength at 1 kOe [see Figure 7.6(c)]. Thus it is concluded that the magnetodielectric effect in Dy-IG is not directly related to any of the measured low-frequency LF or KK modes, but is rather determined by the optical phonons.

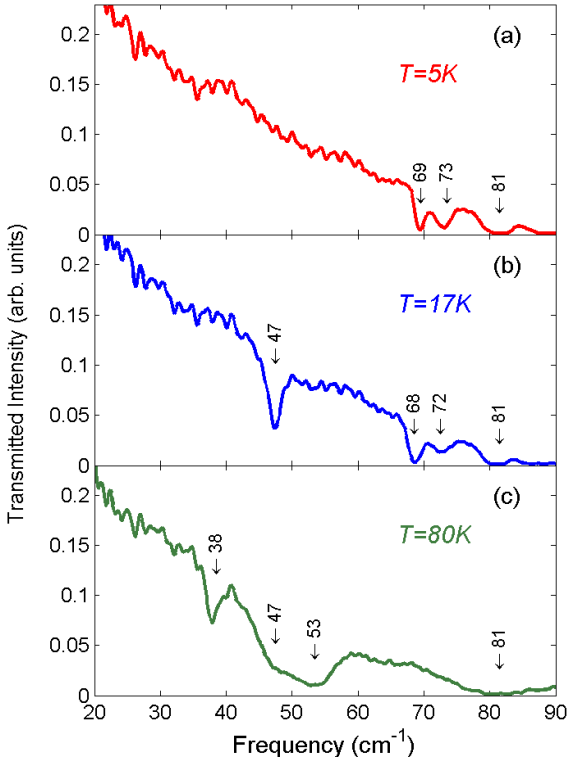

Figure 7.7 Normalized far-IR transmission spectra for $Tb_3Fe_5O_{12}$ single crystal measured in a zero external magnetic field at T = 5, 17, and 80 K: (a), (b), and (c), respectively. The light propagation is along the [1 1 1] direction. Arrows indicate the frequencies of IR-active absorption lines. The weak intensity oscillations between 20 and 35 cm^{-1} are the interference thickness fringes.

7.5 $Tb_3Fe_5O_{12}$ (AFMR and Ligand Field)

7.5.1 Experiments at Zero Magnetic Field

Figure 7.7 shows normalized transmission spectra of $Tb_3Fe_5O_{12}$ measured at T = 5, 17, and 80 K in a zero external magnetic field. The low-temperature absorption lines appear at 69, 73, and 81 cm^{-1}. An additional line at 47 cm^{-1} demonstrated a significant increase of the oscillator strength with the temperature becoming more pronounced for T>12 K. A strong decrease of the transmitted intensity above 90 cm^{-1} is due to the absorption by the

optical phonons. [90] The transmission intensity map [see Figure 7.8(a)] was measured with the temperature increments of 2 K. The frequencies of the three absorption lines at 47, 73, and 81 cm^{-1} show practically no temperature dependence [see Figure 7.8(b)]. In contrast, the fourth line demonstrates a significant softening from 69 to 30 cm^{-1} when temperature increases from 5 and 140 K.

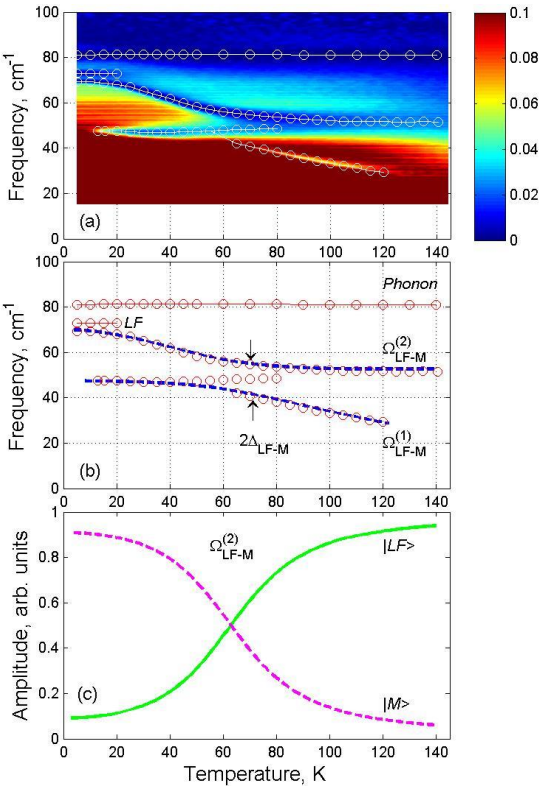

Figure 7.8 (a) Maps of the normalized transmitted intensity *vs.* temperature and frequency for $Tb_3Fe_5O_{12}$. The blue (dark) color corresponds to stronger absorption, red (light) color indicates high transmission. The transmission intensity scale is between 0 and 0.1. (b) Experimental values for the ligand-field (LF) and the hybrid LF-M excitations. The results of the fit using Eq. (2) with the coupling constant $\Delta_{LF\text{-}M}$ = 6 cm^{-1} are shown with blue dashed curves. (c) |LF> and |M> wavefunction amplitudes for the upper energy $\left|\Omega^{(2)}_{LF-M}\right\rangle$ hybrid state.

The assignment process for the observed IR excitations to electric-dipole or magnetic-dipole IR transitions is not straightforward in transmission experiments,

especially without a proper light polarization analysis. Among more reliable optical techniques could be variable-incidence-angle polarized reflectivity and, of course, full-Muller matrix ellipsometry. [91] Note, however, that these techniques were not routinely available for the far-IR spectral range during the time of these experiments. Several indirect evidences, such as temperature and magnetic field dependencies as well as a comparison with the earlier far-IR studies of other rare earth garnet compounds have been used. [84] For example, strong temperature dependence for the frequency of the line, which appears at 69 cm^{-1} (T=5K), is typical for magnetic excitations. [84] [92] In contrast, weak temperature dependence is expected for the frequency of the single ion and crystal-field-type excitations, especially far from the phase transitions. The ligand field spectrum should change significantly if one rare earth ion is substituted by another one in *R*-IG. Indeed, the preliminary IR transmission measurements for a similar compound, $Dy_3Fe_5O_{12}$, show a completely different set of absorption lines at 13, 22, 28, 43, 59, and 75 cm^{-1}. Thus, the lines at 47 and 73 can be attributed to ligand-field (LF) transitions of Tb^{3+} ions in Tb-IG. The energies are determined by the combination of the crystalline electric field and the exchange field produced by iron, both nearly temperature-independent since the Fe sublattice remains completely ordered at low temperatures. Detailed information on the crystal field and exchange interactions in *R*-IG can be found in Reference [93]. The line at 81 cm^{-1} was observed previously in a number of *R*-IG and had been attributed to the lowest-frequency IR-active optical phonon. [84] This interpretation is supported by the typical red shift $\sim(m_R)^{-1/2}$ of the line frequency for *R*-IG compounds for the different mass m_R of the rare-earth ions: from 83 for Sm down to 79 cm^{-1} for Er.

In addition to phonons and crystal-field excitations, far-IR spectra of ferrimagnetic materials can exhibit magnetic excitations related to the spins of iron and rare-earth ions, such as magnons. An acoustic ferrimagnetic mode that corresponds to the strongest superexchange Fe-Fe interaction falls in a very low frequency range. It has been observed in a non-rare-earth Yttrium iron garnet in the magnetic field of 0.32 T at ~0.3 cm^{-1}, [94] which is well below the frequency range for the experiments. The Fe-Tb ferrimagnetic interaction reveals itself in the measured far-IR spectral range. A simplified theory for a *R*-IG with a collinear spin arrangement was developed in Reference [85]. Although this approach is not directly applicable to the case of Tb-IG with the non-collinear spins, it is helpful with understanding of the major trends in the mode behavior with temperature and magnetic field. If one considers only the interaction between the rare earth ion and the combined Fe subsystems, then two optical magnetic modes should appear. One is the Kaplan-Kittel (KK) mode Ω_M, [79] which corresponds to the exchange between two magnetic subsystems. Another one Ω_{LF} corresponds to precession of the rare earth ion moments in the effective field imposed by the iron magnetization. The zone-center energies of these modes are

$$\Omega_{\mathrm{M}}(\mathrm{T}) = \lambda_{\mathrm{ex}}\mu_{\mathrm{B}}[g_{\mathrm{Fe}}\mathrm{M}_{\mathrm{Tb}}(\mathrm{T}) - g_{\mathrm{Tb}}\mathrm{M}_{\mathrm{Fe}}] \tag{7.4}$$

$$\Omega_{\mathrm{LF}} = \lambda_{\mathrm{ex}}\mu_{\mathrm{B}}g_{\mathrm{Tb}}\mathrm{M}_{\mathrm{Fe}} \tag{7.5}$$

where μ_B is the Bohr magneton ($\mu_B \approx 0.4669$ cm^{-1}/T), λ_{ex} is the exchange constant, $g_{Fe,Tb}$ are the corresponding g-factors, M_{Tb} is the Tb sublattice magnetization, and $M_{Fe}$is the combined Fe magnetization. At the zone center ($k \approx 0$) the frequency of the Ω_{LF} mode corresponds to the single ion precession in the magnetic field imposed by Fe on Tb. For an ion with integer J, like Tb, the corresponding energy should be equal to the LF

splitting of the doubly-degenerated ground state of the free rare earth ion. Thus, the line at 47 cm^{-1} [Figure 7.8(a,b)] can be attributed to Ω_{LF} in Equation 7.5. For T<150 K, Tb magnetization $M_{Tb}(T)$ has a strong temperature dependence. [21] In contrast, the iron subsystem magnetization M_{Fe} is almost constant in this temperature range. Accordingly, one can expect that $\Omega_M(T)$ will reflect the change of $M_{Tb}(T)$. Note, that the balance between $g_{Fe}M_{Tb}(T)$ and $g_{Tb}M_{Fe}$ determines the temperature trend in $\Omega_M(T)$. If $g_{Fe}M_R(T) < g_R M_{Fe}$, as in Yb-IG, the KK mode frequency increases with T approaching Ω_{LF} when *R* magnetization disappears. [84] In Tb-IG, $g_{Fe}M_{Tb}(T) > g_{Tb}M_{Fe}$ and, hence, the KK mode frequency should decrease with temperature disappearing at the compensation point. This expectation for $\Omega_M(T)$is supported by the trend in the experimental data shown in Figure 7.7(a,b) for the soft mode between 69 and 30 cm^{-1}. The KK modes have been studied experimentally in a number of *R*-IG compounds *R*=Sm, Ho, Er, Yt (see Reference [84]), but no reports have been done for *R*=Tb and Dy. Among other factors, the oscillator strength for the KK mode depends on the difference $[g_{Tb} - g_{Fe}]^2$ between g-factors for Tb and Fe. [85] [84] This rule has been confirmed for another compound, Gd-IG, where no KK magnon was detected between 10 and 100 cm^{-1} due to a close proximity of g-factors for Gd and Fe: $g_{Gd} \approx g_{Fe} = 2$. The same argument explains why no KK mode was ever detected for the antiferromagnetic interaction between Fe moments in the tetrahedral and octahedral sites in iron garnets using the far-IR experiments.

The low temperature ratio of $\Omega_M/\Omega_{LF} = 69/47 \approx 1.5$ allows us to estimate the g-factor value of Tb using Equations 7.4 and 7.5: $g_{Tb} = g_{Fe}M_{Tb}/[M_{Fe}(1 + \Omega_M/\Omega_{LF})]$.

The experimental values for Tb and the total Fe sublattice magnetizations $M_{Tb} \approx 45\mu_B$/mole and $M_{Fe} \approx 5\mu_B$/mole, [89] [21] and $g_{Fe} = 2$ result in the effective value of $g_{Tb} \approx 7.2$, which is significantly larger than the free-ion value for Tb: $g_0 = 1.5$. Note that such a difference is common in *R*-IG, where the J-mixing and re-population of the crystal-field states at low temperature modify the effective g-factor, making it strongly anisotropic. For example, the experimental values for g_{Dy} ($g_x = 11.07$, $g_y = 1.07$, and $g_z = 7.85$) are significantly larger than the corresponding free-ion value of $g_0 = 4/3$ for Dy in Dy-IG. [89]

Unfortunately, the intensities of the magnetic and LF lines decrease dramatically for temperatures above 140 K, where only the optical phonon at 81 cm^{-1} is visible. This decrease is probably related to the temperature-induced population of the electronic states at 47 and 73 cm^{-1}. Another reason may be related to the disappearance of the rhombohedral distortions for T >150 K that restores the local symmetry of Rare Earth ion thus changing the selection rules for the optical transitions between the LF electronic states of Tb^{3+}.

An accurate theoretical model is required for description of the magnetic mode spectrum. It should take into account (i) the crystal-field splitting of Tb and its symmetry affected by the rhombohedral distortion of the cubic cell, (ii) variation of the anisotropic g_{Tb} due to the temperature-induced population of the crystal-field levels, and (iii) the anisotropic Tb-Fe exchange for all magnetic sub-systems: two different Tb that correspond to the double-umbrella structure, and two Fe in the tetrahedral and octahedral sites. In this case, one could expect an additional splitting of the exchange mode that corresponds to Tb subsystems with the corresponding magnetic moments of $8.18\mu_B$ and

$8.9\mu_B$. [89] In this experiment, such splitting was not clearly detected. A qualitative interpretation of the experimental results can continue to relate the soft mode (69 cm^{-1} at low temperature) to the average KK-type exchange excitation, (or a zone-center magnon), and the hard mode (47 cm^{-1}) as related to the LF excitation.

In the temperature range around 60 K, an anticrossing occurs between two lower-frequency lines indicating a significant hybridization between the exchange magnon and the LF excitation of Tb^{3+} ions. The results of the fit for the temperature dependence of these two hybrid excitations ($\Omega_{LF-M}^{(1)}$ and $\Omega_{LF-M}^{(2)}$) is shown in Figure 7.8(b). The dashed curves are solutions of the LF-M exchange Hamiltonian, which can be written as follows

$$\hat{\mathrm{H}} = \begin{bmatrix} \Omega_{\mathrm{M}} & \Delta_{\mathrm{LF-M}} \\ \Delta_{\mathrm{LF-M}} & \Omega_{\mathrm{LF}} \end{bmatrix} \tag{7.6}$$

in the {|LF>, |M>} basis. Here it is assumed that Ω_{LF} and the coupling constant Δ_{LF-M} are temperature independent, but Ω_M depends on temperatures. The energy eigenvalues of this Hamiltonian are

$$\Omega_{\mathrm{LF-M}}^{(1,2)} = \frac{\Omega_{\mathrm{LF}} + \Omega_{\mathrm{M}}}{2} \pm \sqrt{\left(\frac{\Omega_{\mathrm{LF}} - \Omega_{\mathrm{M}}}{2}\right)^2 + \Delta_{\mathrm{LF-M}}^2} \tag{7.7}$$

and the corresponding eigenstates are

$$\left|\Omega_{\mathrm{LF-M}}^{(2)}\right\rangle = \begin{pmatrix} \cos\theta \\ \sin\theta \end{pmatrix} \tag{7.8}$$

$$\left|\Omega_{\mathrm{LF-M}}^{(1)}\right\rangle = \begin{pmatrix} -\sin\theta \\ \cos\theta \end{pmatrix} \tag{7.9}$$

where $\theta = \tan^{-1}\left(\sqrt{r^2+1} - r\right)$ and $r = (\Omega_{LF} - \Omega_M)/(2\Delta_{LF-M})$. The best fit for the coupling constant value Δ_{LF-M} is 6 cm^{-1}, which is about 10% of the average energy for the hybrid excitations. With the $\Omega_{LF} - \Omega_M$ separation of approximately –20 cm^{-1} and 20 cm^{-1} at T=10 K and 120 K, θ varies between about 75 and 15 degrees. By calculating

$\cos^2(\theta)$ and $\sin^2(\theta)$ versus T, as shown in Figure 7.8(c), it is found that near 5 K the $\left|\Omega_{LF-M}^{(2)}\right\rangle$ state is made of about 93% magnon state and 7% LF state and vice versa for the $\left|\Omega_{LF-M}^{(1)}\right\rangle$ state. This composition is reversed near 120 K. To understand the nature of the LF-M exchange interaction Δ_{LF-M}, special theoretical studies would be required. This interaction is local and it definitely occurs on the rare earth site. On one hand, the magnetic exchange between Fe and Tb sublattices [Equations 7.4 and 7.5] depends on the ground state of Tb ions, which, on the other hand, is affected by the exchange field produced by the Fe ions influencing the LF energies. It is suggested that the specific combination of the KK and LF frequencies, which is determined by the strong Tb magnetization and its g-factor value, makes Tb-IG unique in the line of other *R*-IGs.

For a simple antiferromagnetic system with a cubic symmetry and with collinear spins, both the LF and M modes are pure magnetic dipoles. The corresponding optical transitions should be circularly polarized and their spectral weight should contribute to the static value of $\mu(0,T)$ only. However, the strongly anisotropic Fe-Tb exchange, rhombohedral distortion of the lattice, and a possible DM-type of interaction between non-collinear spins of Tb and Fe, can result in a "forced" electric-dipole activity for the coupled LF and M excitations in Tb-IG. Since Tb is not at the center of inversion in Tb-IG, the electric-dipole oscillator strength of the hybrid mode can originate from the "forced" electric-dipole-active LF excitation. [87] In this case, the LF-M modes can have both the magnetic-dipole and electric-dipole activity. Without a proper analysis of the IR mode polarization, it is hard to decouple the total contribution of the hybrid modes with $\Omega_{LF-M}^{(1,2)}$ energies and $S_{e,m}^{(1,2)}$oscillator strengths between the changes for the static values of the dielectric $\Delta\varepsilon(0,\mathrm{T})$ and magnetic $\Delta\mu(0,\mathrm{T})$ constants:

$$\Delta\varepsilon(0,\mathrm{T}) = \left(\frac{\mathrm{S_e^{(1)}}}{\Omega^{(1)}_{\mathrm{LF-M}}(\mathrm{T})}\right)^2 + \left(\frac{\mathrm{S_e^{(2)}}}{\Omega^{(2)}_{\mathrm{LF-M}}(\mathrm{T})}\right)^2 \tag{7.10}$$

$$\Delta\mu(0,\mathrm{T}) = \left(\frac{\mathrm{S_m^{(1)}}}{\Omega^{(1)}_{\mathrm{LF-M}}(\mathrm{T})}\right)^2 + \left(\frac{\mathrm{S_m^{(2)}}}{\Omega^{(2)}_{\mathrm{LF-M}}(\mathrm{T})}\right)^2 \tag{7.11}$$

Figure 7.9(a,b) shows experimental results for the sum of the right hand parts of Equations 7.10 and 7.11. The experimental data for the combined weight of the hybrid modes $S^{(1)} = S_e^{(1)} + S_m^{(1)}$ and $S^{(2)} = S_e^{(2)} + S_m^{(2)}$ were obtained from the transmission spectra by using a fit to a multiple oscillator model for magnetic and dielectric functions. Strong variation of the oscillator strength for the line at 47 cm^{-1} in the temperature range between 5 and 30 K [see Figure 7.9(a)] is most likely due to the interaction between LF and acoustic excitations. The combined oscillator weight [Figure 7.9(b)] is close to the earlier measurement of the static dielectric constant [Figure 7.9(c)] from Reference [67] and the increase with temperature is reproduced in both dependencies. Note that $\varepsilon(0,T)$ in Figure 7.9(c) was measured for the direction of electric field [1 -1 0] perpendicular to the light propagation direction in this experiments, which is exactly as it should be for a proper comparison between the static and optical measurements.

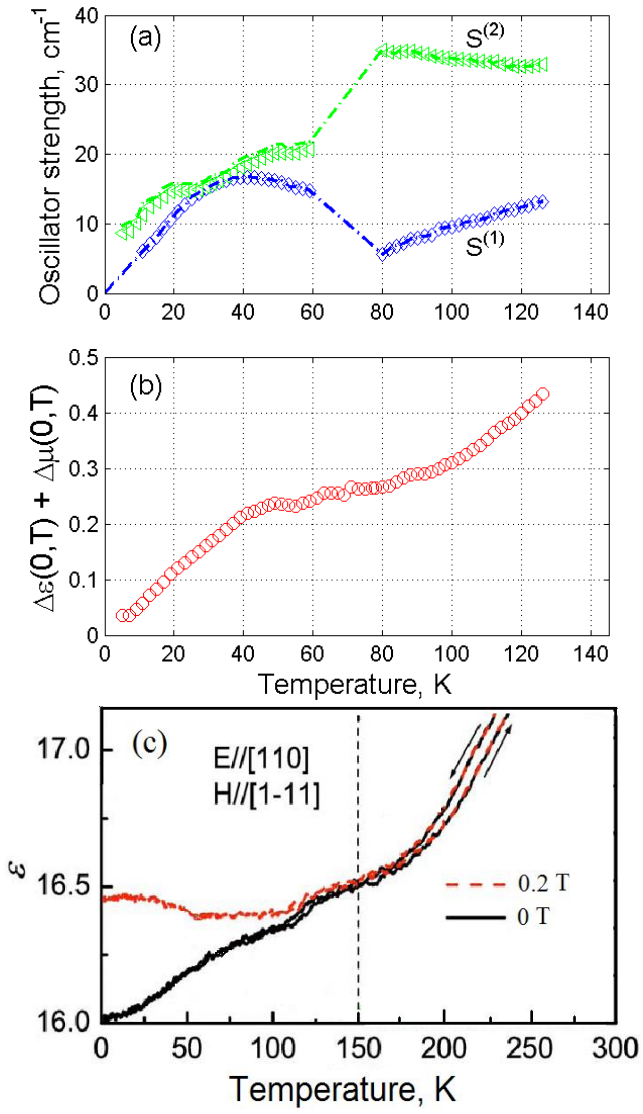

Figure 7.9 (a) Temperature dependence for the oscillator strength for the two hybrid modes with the frequencies $\Omega^{(1)}_{LF-M}$ and $\Omega^{(2)}_{LF-M}$. In the temperature range between 60 and 80 K the modes are strongly coupled and only their sum can be determined. (b) Total contribution of the hybrid modes to the static values of $\varepsilon(0,T)$ and $\mu(0,T)$ calculated from the transmission spectra using Eq. (4). (c) The temperature-induced variation of the static dielectric constant for $Tb_3Fe_5O_{12}$ at zero magnetic field and at the magnetic field of 0.2 T (from Reference [24]).

From the numerical comparison between two curves: $\Delta\varepsilon(0,T) + \Delta\mu(0,T)$ in

Figure 7.9(b) and $\varepsilon(0,T)$ in Figure 7.9(c) one can estimate that the hybrid mode is about (60±30)% electric-dipole active. The error bar takes into account the uncertainty of polarization and normalization errors for transmission measurements. Nevertheless, this comparison allows us to confirm the existence of the ligand-field magnon excitations with a significant electric-dipole activity in Tb-IG. Note that such hybrid LF-M excitation is different from conventional electromagnons in multiferroics that are usually attributed in literature to the interaction between magnons and optical phonons. [51] As it will be shown in the subsequent sections, no interaction was observed between the hybrid modes and the lowest frequency optical phonon.

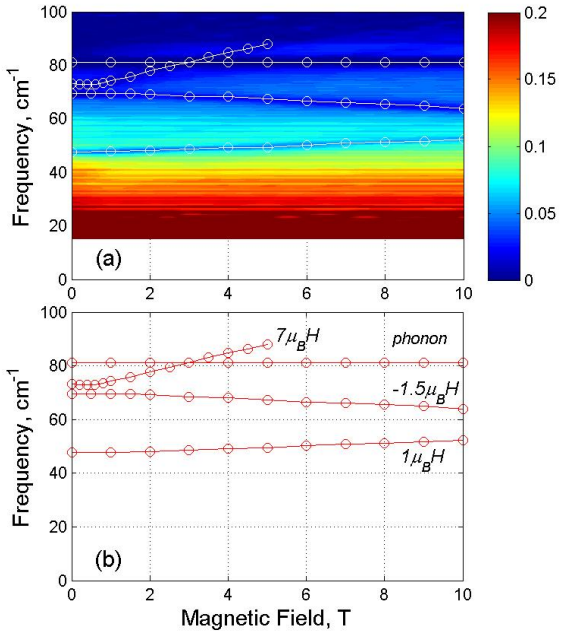

Figure 7.10 (a) Maps of the normalized transmitted intensity *vs.* magnetic field and frequency for $Tb_3Fe_5O_{12}$ at T=15 K and H || [1 1 1]. The blue (dark) color corresponds to stronger absorption, while red (light) color indicates high transmission. The transmission intensity scale is between 0 and 0.2. (b) Variation of the LF, magnon, and phonon excitations in magnetic field H || [1 1 1]. The linear slopes for magnetic field dependence for $\Omega^{(1)}_{LF-M}$, $\Omega^{(2)}_{LF-M}$, and $\Omega^{(3)}_{LF-M}$ excitations are $1\mu_B$, $-1.5\mu_B$, and $7\mu_B$, respectively.

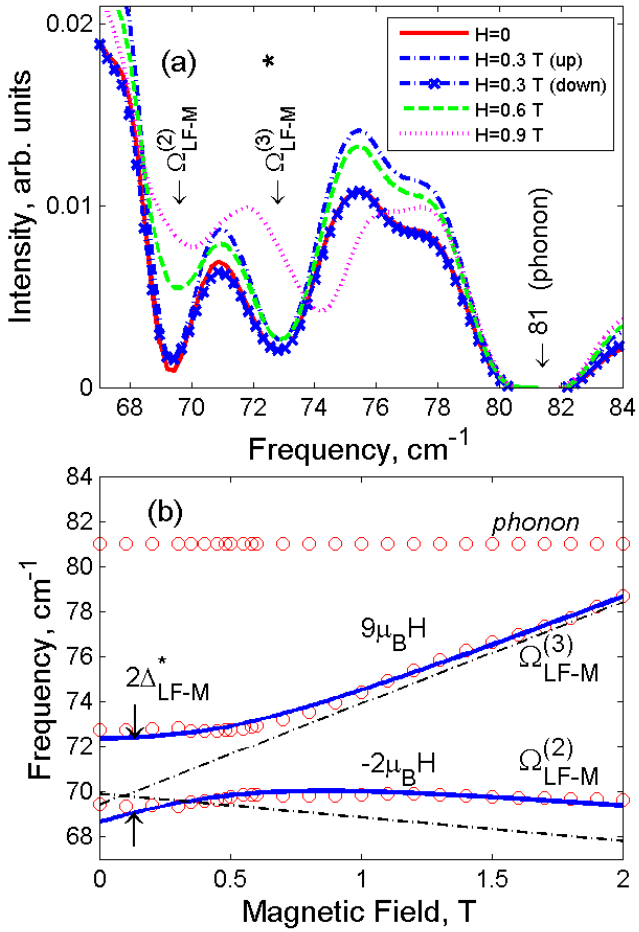

Figure 7.11 (a) Normalized far-IR transmission spectra for $Tb_3Fe_5O_{12}$ single crystal measured at T= 5 K for external magnetic field H = 0, 0.3, 0.6, and 0.9 T. Both, the light propagation and magnetic field are along the [1 0 0] direction. Arrows indicate the frequencies of two hybrid modes: $\Omega^{(2)}_{LF-M}$ and $\Omega^{(3)}_{LF-M}$. (b) Variation of the coupled LF-M excitations $\Omega^{(2)}_{LF-M}$ and $\Omega^{(3)}_{LF-M}$ in magnetic field H || [1 0 0]. Blue solid lines are fits using Eq. (5) for coupled excitations. Dashed lines are strong-field approximations for uncoupled excitations.

7.5.2 Experiments in Magnetic Fields

A strong magnetic field H applied along [1 1 1] direction (Faraday configuration) causes a linear increase of two LF energies. This effect can be described by the effective g-

factors as follows: $\Omega(H) = \Omega(0) + g\mu_B H$, where μ_B is the Bohr magneton ($\mu_B \approx 0.4669$ cm^{-1}/T). The corresponding slopes $\partial\Omega(H)/\partial H = g\mu_B$ for transitions at 47 and 73 cm^{-1} are $1\mu_B$ and $7\mu_B$, respectively [see Figure 7.10(a,b)]. Note that the slope of the magnetic field dependence for the LF line at 73 cm^{-1} corresponds to $g = 7$, which is the same value as was estimated for Tb in the previous Section 7.5.1 [Figure 7.10(b)]. As expected, the lowest-frequency optical phonon at 81 cm^{-1} does not change in magnetic field. Even more, the resonance between the phonon and the LF line at ~3 T has no pronounced anticrossing, which indicates their weak interaction. In strong magnetic fields, there is a significant softening of the hybrid mode $\Omega^{(2)}_{LF-M}$ with the slope of about $-1.5\mu_B$.

The most interesting part of the magnetic field dependence is in the range for H < 0.5 T [see Figure 7.11(a,b)], where the magnetodielectric effect has been previously reported [24]. For both directions of the applied magnetic field: along [1 1 1] and [1 0 0], non-linear behavior is observed for $\Omega^{(2)}_{LF-M}(H)$. A close zoom on this dependence for H || [1 0 0] is shown in Figure 7.10(b). Note that the high-field slope for $\Omega^{(2)}_{LF-M}(H)$ increases for this orientation up to $9\mu_B$ compared to that for H || [1 1 1]: $7\mu_B$. Figure 7.11(b) illustrates that another coupling between the magnon at 69 cm^{-1} and another LF excitation at 73 cm^{-1} (marked with symbol *) occurs at the weak magnetic fields. Two coupled excitations are separated by ~3.5 cm^{-1} in the field range between 0 and 0.5 T. In stronger fields, the Zeeman effect becomes dominant and the LF transition shifts up, while the magnon slowly decreases its energy. Solutions of the following Hamiltonian

$$\widehat{\mathrm{H}} = \begin{bmatrix} \Omega^{*}_{\mathrm{LF}} & \Delta^{*}_{\mathrm{LF-M}} & 0 \\ \Delta^{*}_{\mathrm{LF-M}} & \Omega_{\mathrm{M}} & \Delta_{\mathrm{LF-M}} \\ 0 & \Delta_{\mathrm{LF-M}} & \Omega_{\mathrm{LF}} \end{bmatrix} \tag{7.12}$$

are shown in Figure 7.11(b) with blue curves. The zero-field coupling constant Δ^*_{LF-M} between the higher energy LF and the magnon excitations is estimated to be 2 cm^{-1}. The high-field solutions for uncoupled excitations are shown in Figure 7.11(b) with dashed lines. The possible hysteresis effect was studied for the ramps of magnetic field up to 10 T and back down to zero. Only minute difference in the oscillator strength for the optical

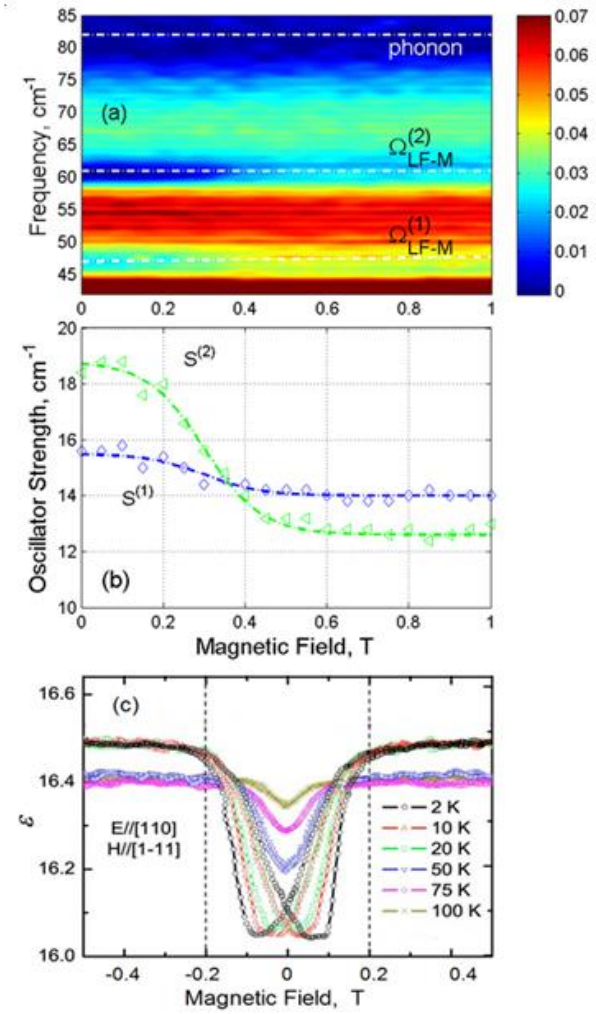

Figure 7.12 (a) Maps of the normalized transmitted intensity *vs.* magnetic field $H \parallel [1\ 1\ 1]$ measured at T = 40 K. The transmission intensity scale is between 0 and 0.07. (b) Results of the fit for the oscillator strengths for two low-frequency hybrid modes: $\Omega^{(1)}_{LF-M}$ and $\Omega^{(2)}_{LF-M}$. Dashed curves guide the eye. (c) Magnetic field dependence of the dielectric constant at various T from Reference [24].

transitions at 69 and 73 cm^{-1} was found, as it is shown in Figure 7.11(a) for several values of magnetic field. The frequency of the corresponding excitations did not depend on the ramping history for magnetic field.

Figure 7.12(a) shows the transmission intensity map measured at 40 K for $H \,||\, [111]$ with increments of 0.05 T. One can see that the optical phonon at 81 cm^{-1} remains unchanged, thus ruling out the possible magnetic-field-dependent contribution of phonons to the magnetodielectric effect. The oscillator strengths [Figure 7.12(b)] for both hybrid modes decrease at the magnetic field of ~0.3 T.

Similar drops for the oscillator strength dependencies have been observed for all measured temperatures between 5 and 70 K and for two directions of the applied magnetic field: [111] and [100]. This result is not expected since the static dielectric constant increases by a few percent in the same range of magnetic field. [24] Figure 7.12(c) shows results from Reference [24] for the change of the static dielectric constant in a weak magnetic field. Although there is a strong nonlinear shift for the LF excitation and a significant modification of the mode oscillator strength, the harmonic oscillator model cannot reproduce the experimental data for the magnetoelectric effect [Figure 7.12(c)]. It is only a speculative assumption that the combined oscillator strength of two hybrid LF-M modes redistributes, therefore the increase of the magnetic part compensates for the decrease of the electric part. The observed variation of the oscillator strength for the hybrid modes can be related to the magnetostriction effect that takes place in exactly the same range of magnetic fields.

7.6 Spectra of the Optical Phonons in $Dy_3Fe_5O_{12}$

Spectra of the optical phonons in *R*-IG were previously studied both theoretically and experimentally. [95] [96] The group theory analysis predicts 17 IR-active optical modes in *R*-IGs at room temperature. [96] Most of the optical phonons have been already observed using transmission spectroscopy in polycrystalline samples. [96] However, due to limitations of the traditional transmission technique, no details are available in literature on the temperature dependence of the phonon frequency, broadening, and oscillator strength for Dy-IG. In this section, presented are the experimental results for the optical phonon spectra obtained with high spectral resolution and small temperature steps around T_C. Modification of the phonon spectra due to rhombohedral distortions for T < 100 K will be discussed. It will be shown that the temperature dependence of $\varepsilon(0,T)$) in Figure 5.1(b) correlates with the oscillator strength of the low-frequency IR-active optical phonons, which also has a peak in the oscillator strength at $T_C = 16$ K.

Figure 7.13 shows experimental data for the real and imaginary parts of the dielectric function ε_1 and ε_2 for 8 K and 300 K obtained using RAE. The spectra of the dielectric function were fitted with a model function consisting of a set of Lorentz oscillators.

$$\varepsilon(\omega) = \sum_{j=1}^{N} \frac{S_j \cdot \omega_{j.0}^2}{\omega^2 - \omega_{j,0}^2 - i\gamma_j\omega} \tag{7.13}$$

where $\omega_{j,0}$ is the phonon frequency, S_j is the oscillator strength, γ_j stands for the phonon broadening, and ε_∞ represents the dielectric constant at frequencies above the optical

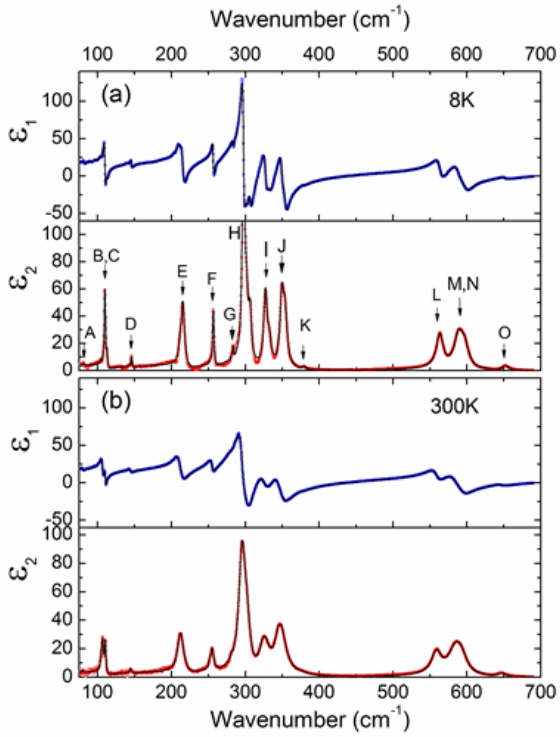

Figure 7.13 Real ε_1 and imaginary ε_2 parts of the dielectric function for Dy-IG with [100] orientation measured with AOI=75°. Experimental results are shown with dots. The results of the fit are shown with solid black curves. (a) T=8 K, (b) T=300 K. The phonon modes are marked with arrows and denoted with letter symbols from A to O in the order of their frequency increase. The maximum value of ε_2 for the H phonon at T=8 K, which is off on the vertical scale, is 195

phonons. Two fitting programs have been consistently used for data analysis: commercial WVASE32 Woollam software and a home-made program based on the 4×4 Berreman's model for anisotropic magneto-electric medium. [97] For the spectra measured at low temperatures, the maximum number of the oscillators used in the fit was N=27. This number does not include the numerous CF and LF transitions below 80 cm^{-1} that were already described in the previous section. Eight weak modes, which correspond to the CF excitations of Dy^{3+}, vanish for the temperatures above ~50 K. To describe the

optical phonon spectrum N=19 oscillators were used for T< 125 K and N=15 oscillators for T> 125 K. The results of the fit are shown in Figure 7.13 (a,b) with solid curves.

A good agreement between the fit and experimental data was obtained after applying a standard data correction for the light focusing on the sample with the numerical aperture *f*/10 used in the experiment. The optical spectra of $\varepsilon_{1,2}(\omega)$ are dominated by several strong IR phonons that are marked in Figure 7.13(a) with the capital letters in the order of their frequency increase. The experimental values of the phonon parameters are summarized in Table 7.1. The phonons labeled A, D, F, G, L, and O are single peaks and their frequencies are close to what have been previously determined from transmission experiments in polycrystalline samples. [96] Other modes, such as E, H, I, and J are closely spaced doublets at T < 125 K, which converge into single peaks at higher temperatures. Two phonon modes B and C are well resolved up to room temperature. The high-frequency phonons M and N are close to each other and their separation at room temperature becomes less than their broadening. The M and N modes are still considered as separate phonons since their splitting is well-defined in the spectra of the frequency derivative of $\partial[\varepsilon_1(\omega)]/\partial\omega$. Note that in the earlier transmission measurements the weak G mode was not detected and the splitting between M and N peaks was not included into consideration and these two phonons were identified as single modes. [96] That explains why only 13 IR phonons were previously reported for *R*-IGs, while 17 phonons are predicted by the group theory analysis.

This chapter has identified 15 phonon modes: from A to O. The possible candidates for the two missing optical phonons at room temperature are probably among the unresolved E, H, I, and J doublets. Note, however, that each of these four modes

could be well-described with single oscillators with some shape distortions due to anharmonic interaction with other optical and acoustic phonons. Future measurements of other *R*-IG compounds should help us to identify the frequencies of the two missing optical phonons.

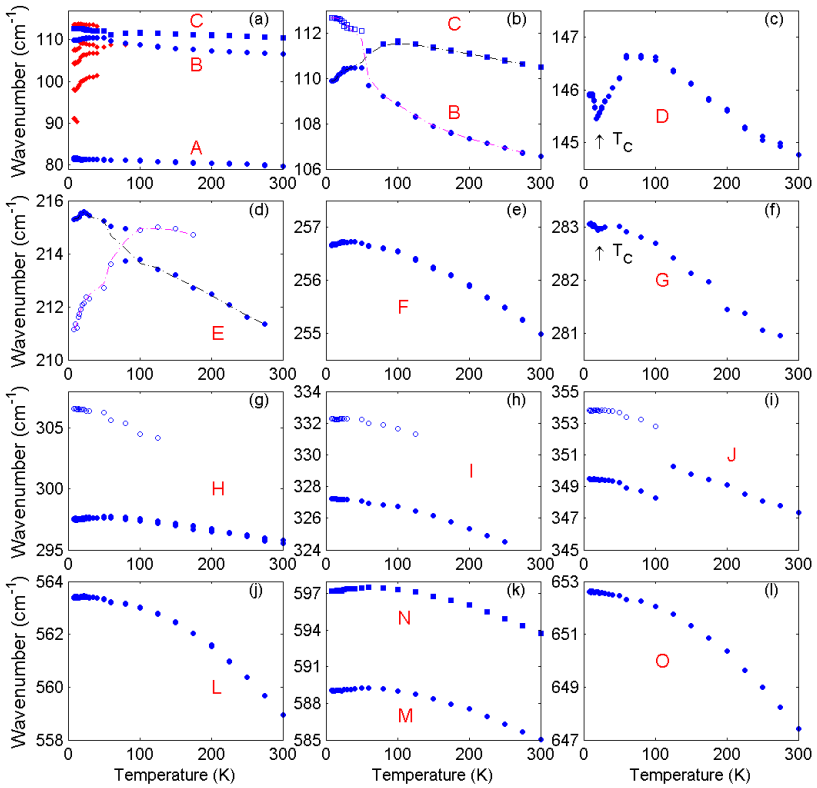

Figure 7.14 Temperature dependence of the frequency for the optical phonons, LF and CF modes. Weak phonon modes are shown with open symbols; strong modes are shown with solid symbols. Letters correspond to the phonon notation in Table I. (a) A, B, and C phonons. Positions of several weak LF and CF peaks at T < 45 K are shown with red diamonds. (b) A closer view at the B and C phonons. The dashed curves guide the eye for the anticrossing between B and C modes at T= 70 K. (c) D phonon, (d) E phonon that splits into two modes below T= 125 K. The dashed curves guide the eye for the anticrossing between two components at T= 70 K. (e) F single phonon. (f) G single phonon. (g) H phonon that splits into two modes at T< 125 K. (h) I phonon that splits into two modes at T< 125 K. (i) J phonon that splits into two modes at T< 125 K. (j) L single phonon. (k) M and N phonons. (l) O single phonon.

Figures 7.14, 7.15, and 7.16 show temperature variation of the phonon frequency, broadening, and oscillator strength. Parameters of the strong modes are shown with solid symbols, while the temperature dependence of the weaker modes is presented with open symbols. The high-frequency phonons, which are associated with vibrations of the lighter ions (oxygen and iron), have a weak frequency dependence at T < 95 K and a typical decrease of their frequency with the linear slope for T >150 K. This natural softening of the optical modes with the temperature increase is caused by the thermal expansion of the lattice and anharmonic phonon–phonon interactions, which become more important as the temperature increases due to the statistical increase of the number of acoustic phonons. In the high-temperature regime, the oscillator strength of the phonons does not change strongly with temperature, while the damping increases quasi-linearly with temperature [see Figure 7.15].

The errors for the phonon parameters in Table 7.1 depend on the type of the mode. For example, the frequencies of the strong single modes, such as D, and F have been determined with uncertainty of about ± 0.1 cm^{-1}. The uncertainty increases, of course, for the frequencies of the broad and weak modes, such as G, L, and O, to about ± 0.3 cm^{-1}. The components of the doublets, such as E, H, I, and J, may have a larger uncertainty for the frequency of the individual components due to instability of the fitting procedure for the overlapping peaks. The errors for the phonon broadenings is about ± 0.2 cm^{-1} for strong single modes and ± 0.5 cm^{-1} for the weak ones. The oscillator strength is the least stable parameter in RAE measurement. For weak modes, the absolute value of the oscillator strength may have an uncertainty exceeding 20% that is

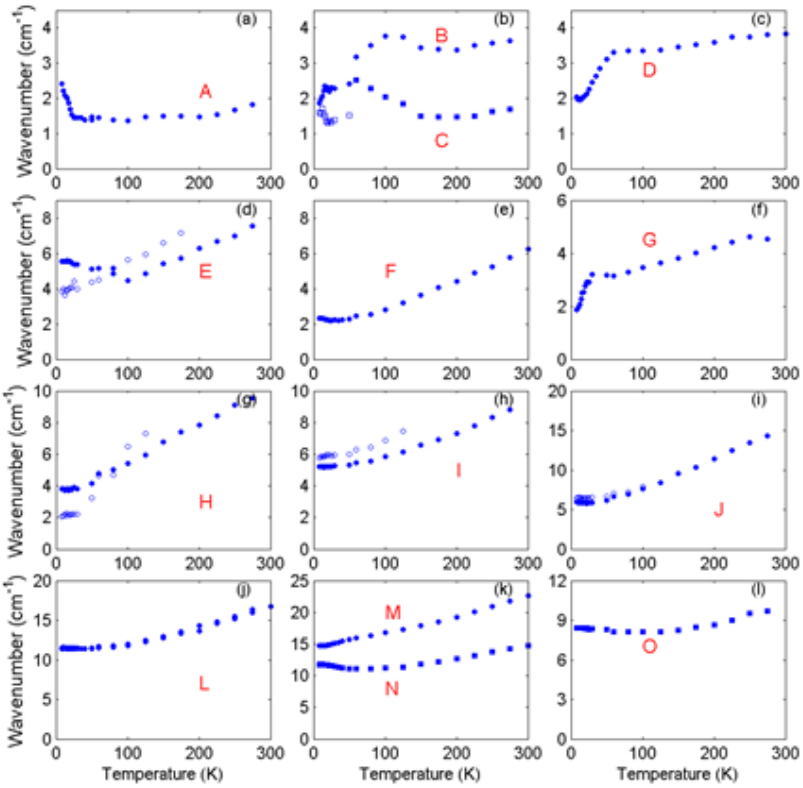

Figure 7.15 Temperature dependence of the optical mode broadening γ. Data for the weak phonon modes are shown with open symbols; strong modes are represented by solid symbols. Letters correspond to the mode notation in Table 7.1. The subplot position is the same as in Figure 7.14

determined by the nature of the nonlinear conversion between the measured ellipsometric angles Ψ, Δ and the dielectric function components: $\{\Psi, \Delta\} \rightarrow \{\varepsilon_1, \varepsilon_2\}$. Even the strong modes may sometimes have a large uncertainty in their oscillator strength due to, for example, the proximity of the experimental values of Δ to 0 or 180°. Note, however, that the relative changes of the oscillator strengths with temperature, as well as the relative temperature-induced shifts of the mode frequencies, which are in the focus of this paper, have been measured more accurately than their absolute values.

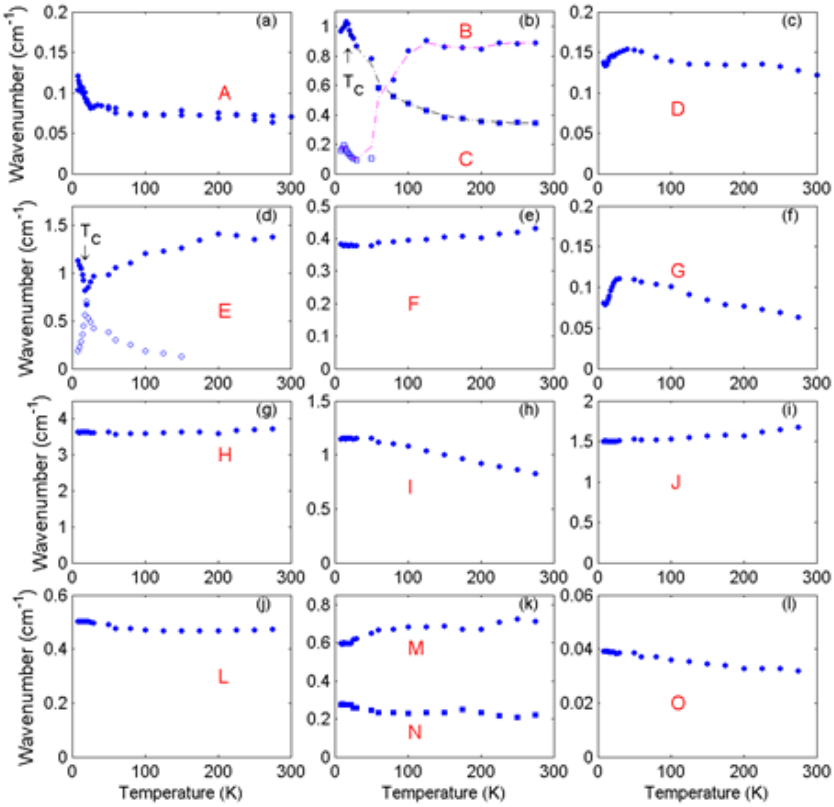

Figure 7.16 Temperature dependence of the oscillator strength *S*. The weak phonon modes are shown with open symbols; strong modes are shown with solid symbols. Letters correspond to the mode notation in Table 7.1. The subplot position is the same as in Figure 7.14 . The dashed curves in (b) guide the eye for the oscillator strength transfer between B and C modes. Subplots (g), (h), and (i) show the average values of *S* for the H, I, and J doublets.

As has already been seen in the previous Section 7.4 of this work, the lowest frequency optical phonon in Dy-IG is at 81 cm^{-1} [peak A in Figure 7.13(a)]. This phonon is related to the Rare-Earth ion motion and is significantly weaker than the IR optical phonons with the frequencies higher than 100 cm^{-1}. The other two low-frequency phonons, B and C, which are also associated with vibrations of the heaviest ion (Dy^{3+}), revealed a fine structure around the primary peaks [Figure 7.14(a)]. At low temperatures the B and C phonons at ~110 and 113 cm^{-1} are surrounded by several weak modes at 98,

104, 107.5, 114, and 119 cm^{-1}. This modeling approach, which can handle the contribution of both electric and magnetic dipoles [see Reference [23] for details], shows that all peaks at 98, 104, 107.5, 114, and 119 cm^{-1} can be attributed to electric-dipole active LF and CF excitations. These excitations have anomalous temperature dependence of their frequency for $T < 45$ K. Above 50 K, when most of the CF peaks vanish due to both the temperature-induced depletion of the ground state and to disappearance of the AFE ordering, the phonons B and C form a doublet with two components of comparable strength that are separated by ~5 cm^{-1}. Note that the frequency and oscillator strength dependencies in Figures 7.14(b) and 7.15(b) suggest an anticrossing between these two modes at T = 70 K.

The E phonon at ~215 cm^{-1} splits into two lines at low temperatures T< 125 K, which in turn experience an anticrossing at T = 70 K as shown in Figures 7.14(d) and 7.17(a). The splitting for the E phonons, as well as that for the H, I, and J phonons in Figure 7.14(g-i) correlates with the rhombohedral distortion of the cubic cell [see Figure 7.17(b)] reported previously for Dy-IG in the same temperature range. [89] Calculations of the temperature dependence of the E phonon frequency has been done using the following equation [98]

$$\omega_0(\mathrm{T}) = \omega_{0|\mathrm{T}=0} \times \exp\left[-3\gamma_{\mathrm{G}} \int_0^{\mathrm{T}} \alpha(\mathrm{T}')\mathrm{dT}'\right] \tag{7.14}$$

where γ_G is a Grüneisen parameter, $\alpha(T)$ is the linear expansion coefficient obtained from Reference [89] [the corresponding experimental data are shown in Figure 7.17(b)] , and $\omega_{0|T=0}$ is the phonon frequency at zero temperature. The results of the calculation using $\gamma_G = 0.7 \pm 0.2$ and $\omega_{0|T=0} = 214$ cm^{-1} are shown in Figure 7.17(a) with a solid

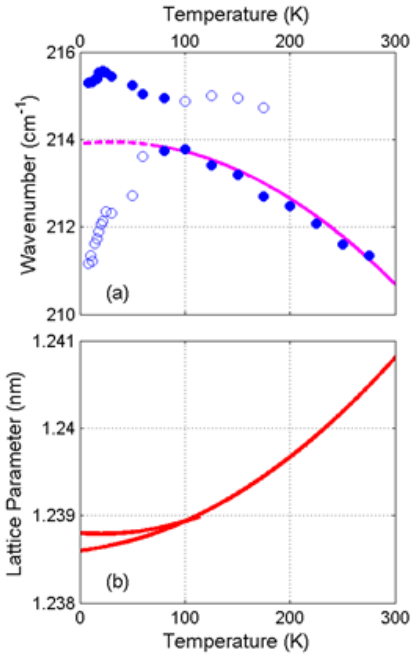

Figure 7.17 (a) Temperature dependence of the frequency for the E phonon. Note the splitting into two components for T < 125 K and the anticrossing at ~ 70 K. The solid curve is a result of the calculations using Eq.(4). The dashed part of the curve also corresponds to Eq.(4) for the temperature range of the rhombohedral distortion using the average value of the thermal expansion coefficient.. (b) Temperature dependence of the lattice parameter for Dy-IG from Reference [89].

curve. While the high temperature regime for $\omega_0(T)$ is well described by Equation 7.14, the same formula cannot be directly applied in the low-temperature range (T< 70 K) for the lattice that is significantly affected by the rhombohedral distortion. Nevertheless, it is noted that both, the thermal expansion of the lattice and anharmonic phonon–phonon interaction, can result only in an increase of the phonon frequency with the temperature decrease. Thus, these two conventional mechanisms cannot explain the softening of the low-frequency component of the E mode below $T \approx 70$ K, which may be an indication that the AFE phase is formed in the sample at low temperatures.

An additional indication of the AFE phase formation can be found in the temperature dependence of the frequency for the D phonon $\omega_{D,0}(T)$ [Figure 7.14(c)]. $\omega_{D,0}(T)$ has a sharp minimum at T_C=16 K, where $\omega_{D,0}(T)$ decreases form ~146.7 cm^{-1} at T=50 K to 145.5 cm^{-1} at T=16 K and recovers back to 146 cm-1 at T=8 K. This trend for $\omega_{D,0}(T)$ contradicts to what is expected from conventional thermal expansion in Equation 7.14 and may also indicate an appearance of electric polarization at low temperatures with the maximum at T_C=16 K. Since the dc measurements did not reveal any measureable macroscopic electric polarization in Dy-IG samples, it can be assumed that the electric polarization in Dy-IG is AFE in origin and the corresponding AFE phase has zero total electric polarization.

The weak G and K modes are phonons in spite of their relatively wean one hand, their oscillator strength is typical for the CF lines, but on the other hand, these peaks are measurable at the temperatures up to 300 K, which is more common for phonons and is not expected for the CF transitions due to re-population of the CF electronic levels at high temperature.

Another weak spectral feature at 442 cm^{-1}, which while observed in the broad temperature range, is not a phonon mode. This spectral anomaly, which is marked LO in Table 7.1, is related to the energy loss in the spectral range where $\varepsilon_1(\omega) \approx 0$. The reason for appearance of this mode is related to the symmetry lowering due to rhombohedral distortion and, thus the small dielectric anisotropy between x, y, and z directions in the measured crystals. By introducing a small anisotropy in ε_∞ and without assigning any

additional oscillator to this spectral range the 4 × 4 Berreman's fitting model was able to reproduce this spectral feature.

TABLE 7.1. Parameters of the fit of the experimental RAE spectra for the optical excitations in Dy-IG between 80 cm^{-1} and 700 cm^{-1} for two temperatures: 8 and 300 K. Results from Reference [96] are shown for comparison. The optical phonon peaks are numbered (left column) and labeled with letters A to O according to the increase of the mode frequency. The type of the modes, such as phonon (Ph) or crystal field (CF), is shown in the right hand column. Phonons that split at low temperature into two modes are marked with Ph(2). The weak modes are marked with stars next to their frequencies.

		ω_0 (cm^{-1}) T=8 K	ω_0 (cm^{-1}) T=300 K	ω_0 (cm^{-1}) T=300 K [a)]	S T=300 K	γ (cm^{-1}) T=300 K	Type
1	A	81	79.7		0.07	1.8	Ph
		98 *					CF
		104 *					CF
		107.5 *					CF
2	B	110	106.5	108	0.90	3.8	Ph
3	C	113	110.5	111	0.38	1.8	Ph
		114 *					CF
		119 *					CF
		123 *					CF
4	D	146	144.8		0.12	3.8	Ph.
		139.8 *					CF
		205 *					CF
5	E	211*					
		215	211	215	1.43	7	Ph (2)
6	F	256.7	255	255	0.43	6	Ph
7	G	283 *	281		0.05	5	Ph
8	H	298	296	309	3.8	9	Ph (2)
		307*					
9	I	327	324	330	0.80	10	Ph (2)
		332*					
10	J	349	347	365	1.7	15	Ph (2)
		354*					
11	K	379*	377.5*	380	0.03	5	Ph
		442*					LO
12	L	563	559	562	0.48	17	Ph
13	M	589	585		0.75	23	Ph
14	N	597	594	597	0.20	15	Ph
15	O	653	645	647	0.03	10	Ph

Source: [96]

The relation between the temperature-induced peak in $\varepsilon(0,T)$ with the experimentally determined parameters of the phonon spectra is sought in the section. Figure 7.1(b) shows that the temperature dependence of $\varepsilon(0,T)$ has a major contribution from the combined oscillator strength of all optical modes in the frequency range between 81 and 660 cm^{-1}, which was determined from the fit of the RAE spectra. The average total oscillator strength of the optical phonons at low temperatures is close to $\sum_{j}^{N} S_j \approx 11.2$, which accounts for more than 2/3 of the average static value of the dielectric constant [$\varepsilon(0) \approx 16.5$ in Figure 5.1(b)] through the LST relation: $\varepsilon(0) = \varepsilon_\infty + \sum_{j}^{N} S_j$. The difference between $\varepsilon(0)$ and $\sum_{j}^{N} S_j$ is about 5.3, which is due to

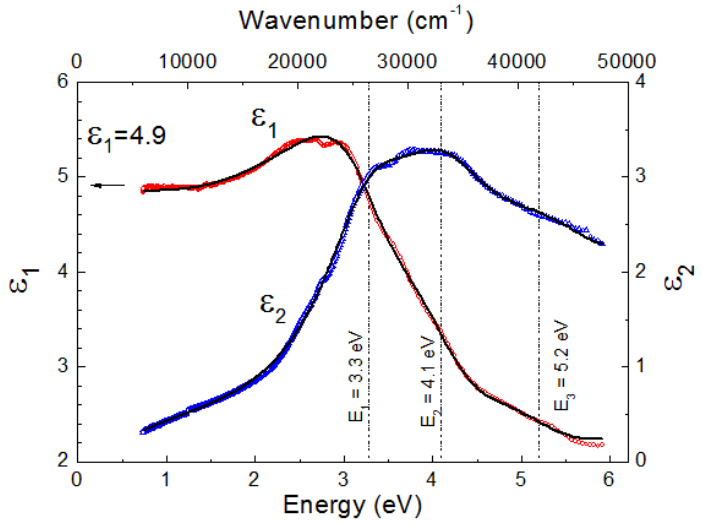

Figure 7.18 Real and imaginary parts of the dielectric function ε_1 (red circles) and ε_2 (blue triangles) for a Dy-IG measured with AOI=75° at T=300 K. The extrapolated low-energy value of ε_1 is 4.9. The results of the fit to the dielectric function model that consists of three electronic transitions at 3.3 eV, 4.1 eV, and 5.2 eV and a Penn gap at 7.7 eV (above the measured spectral range) are shown with black solid curves.

the contribution from the high energy electronic transitions. Unfortunately, the accuracy of in ellipsometry measurements above the highest phonon frequency (~700 cm^{-1}) was not high enough and ε_∞ had to be treated as a temperature-independent fitting parameter in the whole temperature range $\varepsilon_\infty = 5$. To confirm that this value of $\varepsilon_\infty = 5$ is of the right order of magnitude, additional RAE measurements of the same sample were carried out at room temperature in the energy range between 0.75 eV and 5.9 eV. The results of the measurements for the real and imaginary parts of the dielectric function, ε_1 and ε_2 are shown in Figure 7.18. The fit to the dielectric function model that consists of three electronic transitions at 3.3 eV, 4.1 eV, 5.2 eV and a Penn gap at 7.7 eV (above the measured spectral range) is shown with black solid curves. In the low-energy limit, the experimental value of ε_1 is close to 4.9 while ε_2 approaches zero. Thus it can be confirmed that the fitting parameter ε_∞ = 5 that has been used for the phonon frequency range is reasonably close to the room temperature value for $\varepsilon(6000\ cm^{-1}) = 4.9$.

Figures 5.1(b) and 7.16(b) show a substantial correlation between the small change of the static dielectric constant of $\Delta\varepsilon(0,T) \approx 0.15$ around $T_C = 16\,K$ and the temperature dependent oscillator strength of the optical phonons. As seen in Figure 7.18(b), the temperature anomaly in $\sum_j^N S_j$ is determined primarily by the contribution of the B and C phonons. In spite of this obvious correlation between $\Delta\varepsilon(0,T) \approx 0.15$ and $\sum_j^N S_j \approx 0.2$ for the B and C phonons at $T_C = 16K$, it cannot be completely excluded that other possible contributions to the temperature-induced peak in the static dielectric function, such as from crystal defects and high-energy electronic transitions around and above 4 eV. Additional dc measurements of $\varepsilon(0,T)$ at variable frequencies and UV-

ellipsometry experiments at variable temperatures around $T_C = 16\,K$ could clarify this question.

7.7 Conclusions

The LF and KK exchange excitations have been studied in the far-IR transmission spectra of Dy-IG. Their temperature dependencies allowed us to estimate the ratio between the Fe–Dy and Dy–Dy exchange constants to be $\lambda_{Dy-Dy} / \lambda_{Fe-Dy} = 0.13$. The FM phase for Dy-Dy spin interaction was observed for $T < 16$ K and $H < 3.5$ kOe. It has been shown that the combined oscillator strength of the low-frequency KK excitations at 43, 51, and 59.5 cm^{-1} contributes mostly to the static values of magnetic susceptibility $\chi(0,H)$. Since no obvious correlation between the oscillator strength of the KK and LF modes and the magnetic field dependence of the static value of the dielectric constant $\varepsilon(0,H)$ was found, also concluded is that the small increase in $\varepsilon(0,H)$ near H=1 kOe is not related to the KK and LF excitations. The oscillator strength of the optical phonons, which were measured using RAE at zero magnetic field, correlates with the temperature variation of the static dielectric constant $\varepsilon(0,T)$ around $T_C = 16$ K. The oscillator strength for the low-frequency optical phonons (marked B and C) at 110 and 113 cm^{-1} matches this peak in $\varepsilon(0,T)$ through the LST relation: $\Delta\varepsilon(0,T) \approx \Delta S_B(T) + \Delta S_C(T)$.

A strong hybridization has been observed between the magnon and LF transitions. This effect occurs when the corresponding excitations have comparable frequencies. The magnon in Tb-IG is confined between two LF transitions: it couples to the higher-energy one at low temperatures and weak fields, while it comes to a resonance with the low-energy transition at higher temperatures of about 60 K. The corresponding coupling

energies are 2 and 6 cm^{-1}. Redistribution of the oscillator strength between these IR excitations is a consequence of their strong hybridization. The temperature-induced variation of the static dielectric constant seems to correlate well with the softening and the oscillator strength variation of the hybrid modes. The possible role of the rhombohedral distortions in this compound is in a reduction of symmetry on the Tb^{3+} ion that results in the forced electric dipole activity of the LF optical transitions. More detailed theoretical studies are required to confirm a possible connection between the hybrid modes and the magnetodielectric effect in Tb-IG.

CHAPTER 8

MAGNON AND CRYSTAL-FIELD TRANSITIONS IN HEXAGONAL RARE-EARTH MANGANITES $R\mathrm{MnO_3}$ (R= Er, Tm, Yb, Lu)

Far-infrared optical transmission spectra of the antiferromagnetic resonances, or magnons, and crystal field transitions have been studied in hexagonal $R\mathrm{MnO_3}$ (R = Er, Tm, Yb, Lu) single crystals. The magnon and CF frequencies, their oscillator strengths, and effective g-factors have been measured using external magnetic fields up to 9 T in the temperature range between 1.5 K and 100 K. The magnon frequency increases systematically with a decrease of the rare earth ion radius. The magnetic ordering of rare earth ions (R=Er, Tm, Yb) was observed at low temperatures T<3.5 K and in strong external magnetic fields. The observed effects are analyzed taking into account main magnetic interactions in the system including exchange of the Mn^{3+} spins with RE^{3+} paramagnetic moments.

Portions of this work have been published in:

- E. C. Standard, T. Stanislavchuk, A. A. Sirenko, N. Lee, and S. -W. Cheong "Magnons and Crystal-Field Transitions in Hexagonal $R\mathrm{MnO_3}$ (R = Er, Tm, Yb, Lu) Single Crystals" Physical Review B 85 144422 (2012).

8.1 Introduction

Rare-earth manganites $R\mathrm{MnO_3}$ attracted recently a lot of attention due to their intriguing structural, magnetic, and multiferroic properties. The compounds, grown at ambient pressure, usually have either orthorhombic (R=La, ... Dy) or hexagonal structure (R= Ho, …Lu, and Sc, Y), where the choice of the structure is determined by the R^{3+} ionic radius r_i. [99] [32] Recently, multiferroic effects, such as the coupling between the ferroelectric

and magnetic orders, have been found in both hexagonal and orthorhombic RMnO$_3$ compounds, as well as in materials with both non- magnetic R ions, such as in YMnO$_3$ and LuMnO$_3$, and magnetic R ions with the incomplete 4f shell. [100] [101] [37] [102] The difference between the major mechanisms of multiferroicity in orthorhombic and hexagonal manganites is in the focus of modern theoretical and experimental work. [103] [104] [105] [106] [107] [108] Great progress in understanding multiferroicity in orthorhombic system was achieved via far-infrared (IR) optical studies of electromagnons. [109] [110] [111] [112] [113] [114] In contrast, far-IR optical excitations in hexagonal manganites are less understood. The recent studies have been mostly limited to YMnO$_3$ and HoMnO$_3$. [115] [116] This chapter presents spectra of magnons and crystal field (CF) excitations for a number of hexagonal manganites with (R= Er, Tm, Yb, and Lu). The experimental data will be discussed in comparison with the previously published far-IR results for one of the most studied hexagonal compound, HoMnO$_3$. [116]

Both far-IR optical and neutron scattering experiments provide valuable information about spectra of magnons and crystal field (CF) transitions and help to develop an accurate theoretical model for the magnon modes in hexagonal manganites. [103] [117] [118] [119] [120] The 120° spin structure for Mn^{3+} allows for several magnon modes in hexagonal RMnO$_3$. [120] One of them is acoustic and cannot be observed in the optical transmission experiments. Another magnon mode, which is optical with the frequency Ω_M at $\vec{q}=0$, is doubly degenerate. Two components of this magnon mode are circularly polarized in the plane perpendicular to the c-axis. The degeneracy of the Ω_M mode can be lifted up by external magnetic fields applied along

the c-axis. The number of the optical magnon modes in the 120° spin structure can increase further if one takes into account the in-plane spin anisotropy in addition to the conventional uniaxial anisotropy. The frequency of the corresponding single mode Ω_1 would be independent of magnetic field and should be polarized along the c-axis thus being optically inactive for the transmission experiments presented in this chapter. The Ω_1 mode is expected to have a very low frequency, which falls below the frequency cut off in conventional optical experiments. [120] The frequency ratio for these two optical magnon frequencies at $\vec{q} = 0$ is predicted to be $\Omega_1/\Omega_M = \sqrt{6D_2/D}$, where D_2 is the in-plane anisotropy and D is uniaxial anisotropy. Since the Ω_1 mode was not observed in $YMnO_3$ even in the proper polarization configuration for transmission measurements, a conclusion about small in-plane anisotropy $D_2 \ll D$ was made in Reference [120]. In the recent optical transmission measurements in $HoMnO_3$, Talbaev et al. [116] demonstrated the magnon frequency Ω_M renormalization and enhancement of the magnon splitting in the external magnetic field and related these effects to superexchange interaction between Ho^{3+} and Mn^{3+} spins. The effective spin Hamiltonian for the Ho ion ground state was also determined.

Inelastic neutron scattering confirmed the existence of three magnon branches in $YMnO_3$, one of them is acoustic and the other two are degenerate at the center of the Brillouin zone and have frequency near 40 cm^{-1} at $\vec{q} = 0$. Recent polarized inelastic neutron scattering studies revealed that the excitation seen at 1.5 K near 40 cm^{-1} has a hybrid character of magnetic spin wave and a lattice vibration. [121] The authors proposed to explain this mode hybridization by DM interaction.

Below, the focus is on hexagonal manganites with *R*= Er, Tm, Yb, and Lu and particularly on the relationship between their far-IR optical excitations, such as magnons and CF excitations, and the magnetic phase transitions at low temperatures and in high magnetic fields. In this chapter, only the Ω_M magnon modes will be discussed.

8.2 Samples and Experimental Techniques

The high-temperature flux growth technique was utilized to produce bulk crystals of $R\mathrm{MnO_3}$. Single crystal platelets with the hexagonal c-axis perpendicular to the surface and a cross section area of about 4×4 mm^2 and the thickness of about 0.1 mm were used for transmission measurements. The opposite sides of the sample were not wedged, resulting in relatively strong thickness interference fringes in the measured optical spectra. Some crystals had terraces at the surface that resulted to an effective thickness variation across the light beam and irregularities in the thickness fringes in transmission spectra. This chapter presents the experimental results obtained for the samples which had pristine, or as-grown, surfaces. Conventional mechanical polishing was not implemented for any of the samples because it results in significant degradation of their optical properties, such as the broadening of the optical phonon peaks and the appearance of additional broad absorption lines in the optical spectra. The latter is possibly caused by mechanical strains and oxygen reduction at the polished surfaces. It might be possible to recover the optical quality of the samples by annealing in the oxygen atmosphere, but this discussion is beyond the scope of the chapter.

The transmission experiments were carried out at the National Synchrotron Light Source, Brookhaven National Laboratory, at the U4IR beamline equipped with a Bruker

IR spectrometer and a LHe-pumped (~1.6 K) bolometer. Far-IR transmission spectra were measured using linearly polarized synchrotron radiation with the resolution of 0.3 cm^{-1} in the spectral range between 8 and 125 cm^{-1}. Polarization of the transmitted light was not analyzed because of in-plane isotropic nature of the hexagonal samples. An external magnetic field of up to 9 T was applied in the Faraday configuration, such that the directions of the light propagation and the field coincided with the c-axis of the crystals. Correspondingly, the electric and magnetic fields of light were always in the hexagonal plane perpendicular to the c-axis. The raw data of transmitted intensity were normalized to transmission through an empty aperture with the size equal to that of the sample. In some figures for thin samples with strong thickness interference fringes, the transmitted intensity was re-normalized for that measured at high temperature or high magnetic field.

8.3 Spectra of Magnon and Crystal Field Excitations in Zero Magnetic Field

Figure 8.1(a,b,c,d) shows transmission spectra measured at T = 4.5 K in four $RMnO_3$ samples with R=Er, Tm, Yb, and Lu. The absorption minima, which correspond to the IR-active modes, such as magnons (AFM resonances) and CF transitions are marked with arrows. The absorption lines in Figure 8.1(a,b,c) are quite weak and, correspondingly, the shape of the transmission spectra is strongly affected by the broad interference fringes with the period of ~12 cm^{-1} for $LuMnO_3$ and $YbMnO_3$ and ~25 cm^{-1} for $TmMnO_3$. In contrast, a strong absorption background due to the CF transitions in $ErMnO_3$ suppresses the interference fringes, which are visible only in the narrow spectral range around 30 cm^{-1}. In the following section, the corrected transmission intensity data for $LuMnO_3$ and

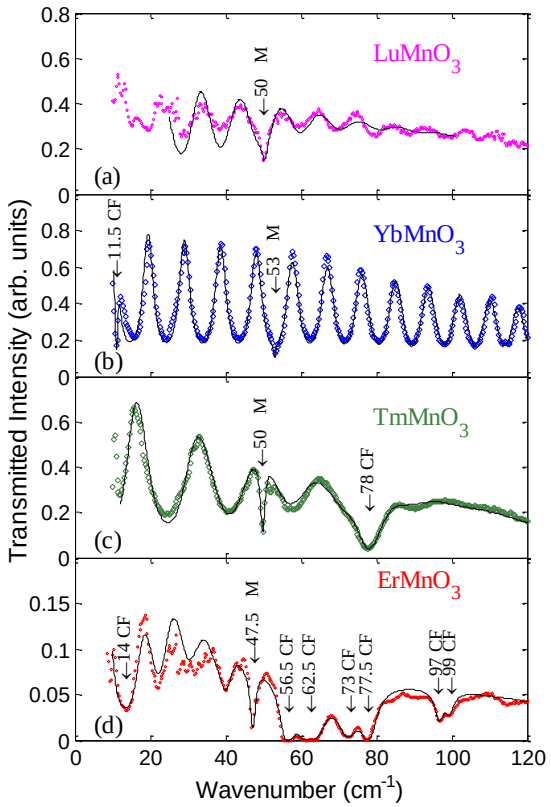

Figure. 8.1 Transmission spectra of RMnO$_3$ samples measured for the light propagation along the c-axis at $T \approx 4.5$ K and at zero magnetic field. The magnon absorption lines are marked with M. The crystal field transitions are marked with CF. Black solid curves represent the fit results using the multi-oscillator dielectric model [see Equation 8.1]. The magnon and CF frequencies are rounded up to 0.5 cm^{-1}.

YbMnO$_3$ will be presented, where the interference fringes will be removed for clarity. Note that using the far-IR ellipsometry setup, it was confirmed that the lowest frequency $a-b$ plane polarized IR-active optical phonon in hexagonal RMnO$_3$ is at ~160 cm^{-1}, which is well above the spectral range shown in Figure 8.1.

LuMnO$_3$: The transmission spectrum of LuMnO$_3$ shown in Figure 8.1(a) has only one magnon peak positioned at 50.1 cm^{-1}. Since Lu^{3+} $\left({}^1S_0\right)$ has a complete $4f^{14}$ shell and zero spin, its compounds should not have any Lu-related crystal field electronic

transitions in the far-IR spectral range. $LuMnO_3$ can be considered as a reference case for other *R* hexagonal manganites where the optical properties in the far-IR spectral range are determined by Mn^{3+} only. One can also expect that the IR optical properties of $LuMnO_3$ should be similar to that of the other hexagonal manganites without 4*f* electrons, such as $YMnO_3$. [120]

$YbMnO_3$: The transmission spectrum of $YbMnO_3$ shown in Figure 8.1(b) has a magnon peak positioned at 53.1 cm^{-1}. Since Yb^{3+} $\left({}^2F_{7/2}\right)$ has incomplete $4f^{13}$ shell, a number of CF transitions can be expected. One CF peak related to the splitting of the ground level is at 11.5 cm^{-1}.

$TmMnO_3$: The transmission spectrum of $TmMnO_3$ shown in Figure. 8.1(c) has a magnon peak positioned at 49.8 cm^{-1}. Tm^{3+} $\left({}^3H_6\right)$ has incomplete $4f^{12}$ shell. The first CF transition is at 73.7 cm^{-1}. A spectral anomaly, which was detected at ~13 cm^{-1} [not labeled in Figure. 8.1(c)], does not show any strong temperature or magnetic field dependences. This feature at ~13cm^{-1} is attributed to the interference effects inside the sample, but additional studies of the samples with different thickness and larger in-plane cross section may be needed to confirm this assumption.

$ErMnO_3$: The transmission spectrum of $ErMnO_3$ shown in Figure. 8.1(d) has a magnon peak positioned at 47.5 cm^{-1}. Er^{3+} $\left({}^4I_{15/2}\right)$ has incomplete $4f^{11}$ shell. Since three *f* electrons are missing, the number of the CF transitions increases compared to that in other $RMnO_3$ compounds. The transmission spectrum has several CF transitions: at 14 cm^{-1} (CF1), and three closely spaced doublets at: 56.7 and 62.3 cm^{-1} (CF2), 72 and 77.4 cm^{-1} (CF3), 97 and 99 cm^{-1} (CF4). In addition to that, one can identify two weaker

spectral features at 22 and 40 cm^{-1}, which do not show any changes correlating with temperature or magnetic field. This allows us to attribute them to trivial thickness fringes.

To determine magnon and CF frequencies Ω_j, adjusted oscillator strengths A_j, and broadening γ_j parameters, the transmission spectra were fitted using a multi-oscillator dielectric model. The results of the fit are shown in Figure 8.1 with solid black curves. An effective transmittivity function $T[\varepsilon(\omega)\cdot\mu(\omega)]$ was used for the fit. The corresponding electric and magnetic responses $\varepsilon(\omega)$ and $\mu(\omega)$ can be presented as a set of Lorentz oscillators

$$\varepsilon(\omega) = \varepsilon_\infty + \sum_{j=1}^{N} \frac{A_{J,e}\cdot\Omega_{j,0}^2}{\Omega_{j,0}^2 - \omega^2 - i\gamma_j\omega} \tag{8.1}$$

$$\mu(\omega) = \mu_\infty + \sum_{j=1}^{N} \frac{A_{J,m}\cdot\Omega_{j,0}^2}{\Omega_{j,0}^2 - \omega^2 - i\gamma_j\omega} \tag{8.2}$$

where A_e is the oscillator strength for an electric dipole and A_m is that for a magnetic dipole, and the off-resonance values of μ_∞ is assumed to be close to 1 [see Reference [122] for more details about transmission spectra analysis]. As determined from the fit, the experimental values of ε_∞ are close to 16.5, which was also confirmed with these ellipsometry measurements. The magnon parameters, calculated in the assumption that the sharp magnon peaks contribute only to $\mu(\omega)$ only are summarized in Table 8.1. Note that the corresponding values of A_m for $LuMnO_3$ and $YbMnO_3$ are smaller than that for $ErMnO_3$ and $TmMnO_3$. This difference can be due to the interaction between the magnons and the neighboring CF transitions and the difference in *R* ion magnetization at low temperatures.

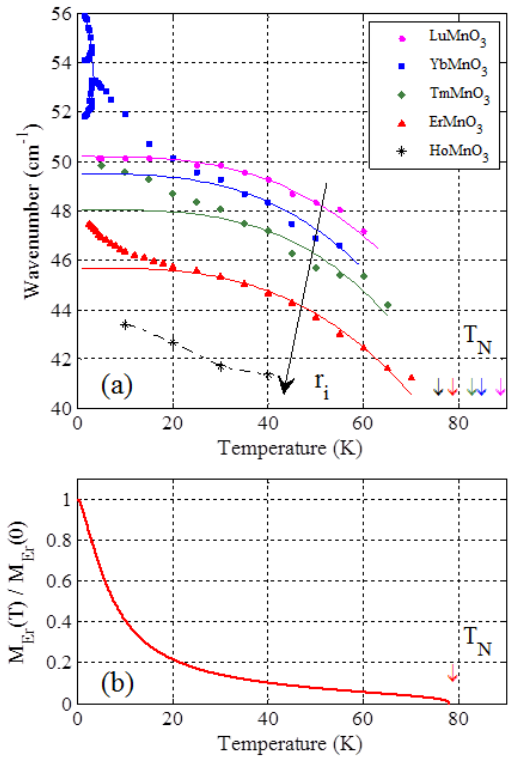

Figure 8.2 (a) Temperature dependence of the magnon frequency for five RMnO$_3$ samples at zero magnetic field. Black stars correspond to HoMnO$_3$ (courtesy of D. Talbayev). At low temperatures, a single magnon in YbMnO$_3$ splits into several distinct absorption lines due to ordering of Yb spins at $T_{Yb} = 3.3K$. Solid curves for Lu, Yb, Tm, and Er samples show the fit results using $\Omega_M(0) - \Omega_M(T) \sim T^3$. Dashed curve for HoMnO$_3$ guide the eye. The AFM transition temperatures T_N for Mn^{3+} are sown with arrows. The arrow labeled r_i indicates the increase of the R ionic radius and the corresponding decrease of both, magnon frequency and T_N. (b) Calculation for the relative change of paramagnetic magnetization of Er^3.

The temperature dependence for the magnon frequency Ω_M is shown in Figure 8.2(a) for five RMnO$_3$ samples. The corresponding literature values of T_N are shown with vertical arrows and are also listed in Table 8.1. As expected, $\Omega_M(T)$ in LuMnO$_3$ demonstrates saturation for $T < 30$ K. When T is approaching the AFM transition at $T_N \cong 87$ K, the magnon peak becomes weaker and its frequency decreases to ~45 cm^{-1}. Since a complete softening of Ω_M even close to T_N was not observed, $\Omega_M(T)$ cannot be

used to confirm the exact value of T_N. The experimental data for $\Omega_M(T)$ in $LuMnO_3$ were fitted using an empirical formula $\Omega_M(T) - \Omega_M(0) \sim T^{\alpha}$, where $\alpha = 3 \pm 0.5$. This temperature dependence of $\Omega_M(T)$ is similar to that for $YMnO_3$, where $\alpha = 3.5 \pm 0.5$. [120] The general trend for decreasing magnon frequency with temperature is also valid for the other four compounds with an incomplete *f*-shell, or $S_R \neq 0$. Comparing the magnon frequency $\Omega_M(T = Const)$ for all five samples at a fixed temperature for $T \approx 25$ K, one can observe that the magnon frequency decreases systematically with the increase of r_i from Lu to Ho. At lower temperatures, however, the expected trend is violated and one can see a sudden increase of the magnon frequency upon cooling in *R* compounds with an incomplete *f* shell. For example, for $T < 20$ K, the $\Omega_M(T)$ curve for $YbMnO_3$ is above that for $LuMnO_3$: $\Omega_M^{Yb} > \Omega_M^{Lu}$. This effect is related to the increasing interaction between Mn^{3+} and PM-ordered R^{3+} spins for $T < 25$, which will be discussed in the next sections. For temperatures above ~ 20 K, the magnon frequency in $ErMnO_3$ fits well with the same function $\Omega_M^{Er}(T) - \Omega_M^{Er}(0) \sim T^{\alpha}$ as that for $LuMnO_3$. However, below T_{SR} one can see a clear deviation from this classical behavior. One of the four measured $RMnO_3$ samples, $YbMnO_3$, shows an unusual dependence of the magnon spectrum below $T < T_R(Yb) = 3.3$ K , where a single magnon line splits into several distinct lines centered around 53 cm^{-1}. In the next section, it will be shown that this effect is attributed to the AFM ordering of Yb spins for $T < T_R(Yb)$. [45]

The temperature dependence of the CF transitions in Er and Tm compounds is rather flat. As shown in Figure 8.3(a, b), the CF peaks become weaker and broader with the temperature increase up to T=100 K due to the interaction of *f* electrons with acoustic phonons and thermal depopulation of the ground state.

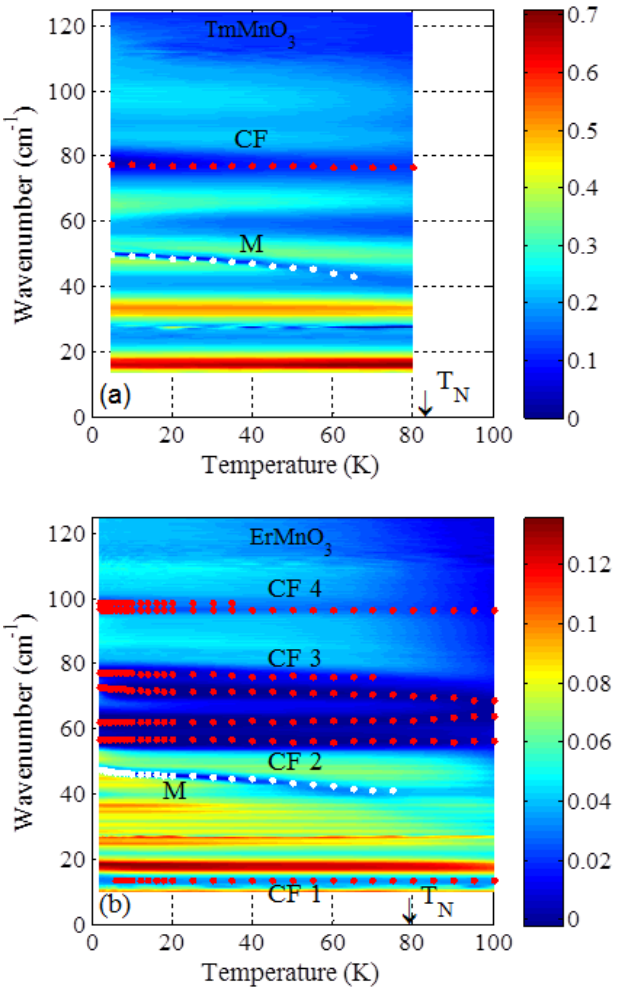

Figure 8.3 Transmission maps *vs.* temperature and light frequency for $TmMnO_3$ (a) and $ErMnO_3$ (b). The blue (dark) color corresponds to stronger absorption and red (light) color indicates high transmission. The transmission intensity scale is shown with the vertical bars. Black arrows indicate the AFM transition temperatures T_N. Frequencies of the CF transitions are shown with red dots and the magnon frequencies are shown with white dots. Noise in the map (a) at ~ 27 cm^{-1} is an artifact of the experimental setup.

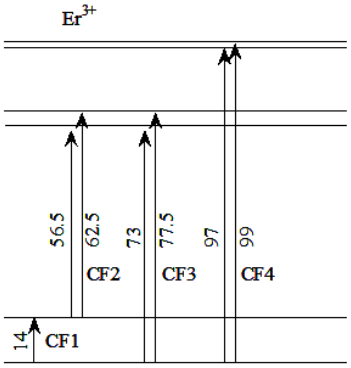

Figure 8.4 Reconstruction of the CF transitions in Er^{3+} in $ErMnO_3$, which is based on the corresponding transmission spectra in Figure. 1(d) and Figure. 3(b). The corresponding transition frequencies in cm^{-1} are shown next to the vertical arrows rounded up to 0.5 cm^{-1}.

One of the possible schematics of the CF transitions in $ErMnO_3$ that was derived from the corresponding transmission data in Figure 8.3(b) is shown in Figure 8.4. Note, however, that the possibility that the CF levels is not the same for Er ions in two sites of the lattice was not taken into account. Thus, CF2, CF3, and CF4 splitting could be due to this difference.

Table 8.1 Magnon frequency, oscillator strength in units of μ_B and broadening: Ω_M, A_M, and γ. The low-field and high field values of the effective magnon *g* and *g'* factors are measured at T = 4.5K for H ‖ c. The magnon frequency Ω_M(T= 25K) has been used to determine the J·D product.

	T_N [A] (K)	Ω_M (cm^{-1})	A_M $\times 10^{-3}$	γ (cm^{-1})	*g* ($H<H_C$)	*g'* ($H>H_C$)	Ω_M T=25K (cm^{-1})	J·D T=25K (cm^{-2})
$LuMnO_3$	88	50.2	1.0	1.1	2.15±0.1	2.05±0.05	49.8	68.9
$YbMnO_3$	84	53.0	1.0	0.6	5.8±0.6	2.65±0.15	49.6	68.3
$TmMnO_3$	82	49.9	2.5	1.0	3.3±0.1	2.1±0.05	48.4	65.1
$ErMnO_3$	78	47.0	4.0	1.1	4.4±0.3	2.5±0.2	45.6	57.8
$HoMnO_3$	75	43.4 [B]			~4 [B]	~2.4 [B]	41.7 [B]	44.4 [C] J=19.7 cm^{-1} D=2.3 cm^{-1}
$YMnO_3$ [D]	76	43			1.9±0.1			

A - Magnetization data from Reference [32]
B - IR transmission data from Reference [116]
C - Neutron data from Reference [119]
D - IR transmission data from Reference [120]

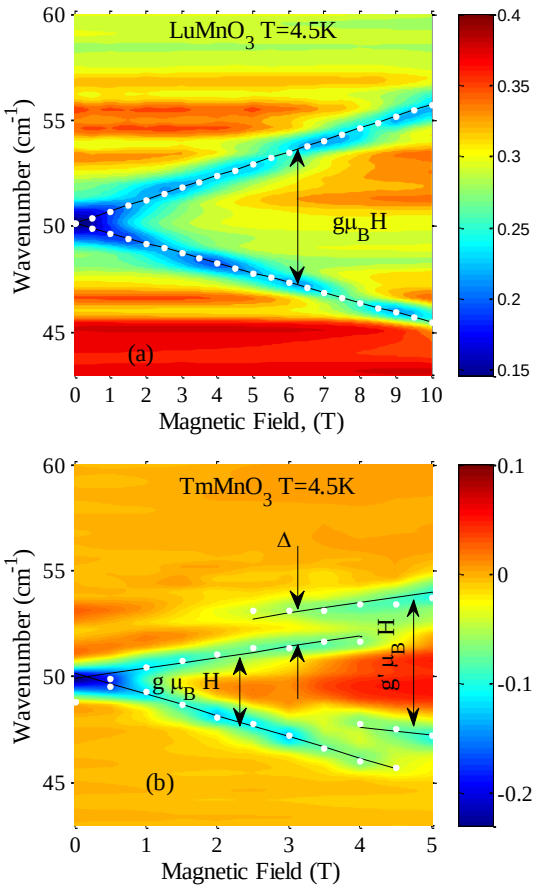

Figure 8.5 Normalized transmission map *vs.* magnetic field and light frequency for $LuMnO_3$ (a) and $TmMnO_3$ (b). The blue (dark) color corresponds to stronger absorption and red (light) color indicates high transmission. The normalized transmission intensity scale is shown with the vertical bars. The white dots represent the fit results for the magnon doublet splitting in external magnetic field [see Equation (8.2)].

8.4 Spectra of the AFM Resonances and CF Excitations in Magnetic Field

In external magnetic field H directed along the c-axis, the doubly-degenerate magnon splits into two branches according to its effective *g*-factors. Figure 8.5(a) shows such dependence of the magnon frequency for $LuMnO_3$ vs. magnetic field: $\Omega_M^{\pm}(H) = \Omega_M(0) \pm \frac{1}{2} g \mu_B H$, where μ_B is the Bohr magneton ($\mu_B \approx 0.4669$ cm^{-1}/T) . As expected for Lu^{3+} compounds with $S_R = 0$, the magnon *g*-factor is determined by Mn^{3+}–Mn^{3+} interaction only. From the linear fit of the magnon doublet frequencies, the

experimental value of the g-factor to be 2.15 ± 0.1has been determined, which is close to the theoretical value of the Mn^{3+} g-factor: g_{Mn} = 2. If one fits the high-magnetic field data points for the magnon doublet for $H > 2T$, where the double splitting is much better defined, then the experimental value for the magnon g-factor becomes even closer to the theoretical expectation: g = 2.05±0.05. The temperature dependence of the magnon splitting in $LuMnO_3$ is negligible up to T=30 K. At higher temperatures the magnon line becomes broader, but still no substantial temperature dependence of the g-factor can be observed within the accuracy of these measurements.

In external magnetic field, the magnon lines in RMnO$_3$ compounds with non-zero spin S_R behave differently compared to that for $LuMnO_3$. First, the splitting $\pm\frac{1}{2}g\mu_B H$ is enhanced corresponding to increases in the effective g-factor well above $g_{Mn} = 2$. The magnon g–factor values for all compounds, which have been determined in relatively weak magnetic fields ($H < 3$ T), are listed in Table 8.1. One can see that g-factors vary non-systematically between 3.3 and 5.7 for different R hexagonal manganites. In contrast to the temperature-independent g-factor for $LuMnO_3$, the low-field values of the magnon g-factor in $YbMnO_3$, $TmMnO_3$, and $ErMnO_3$ strongly depend on temperature as shown in Figure 8.6. For example, the low-temperature value in $YbMnO_3$ is $g = 5.7$, while at higher temperatures $T > 30$ K, the magnon g-factor decreases by a factor of approximately three, approaching the same value as was observed in $LuMnO_3$: $g(T) \rightarrow 2$. For $T > 40$ K the magnetic splitting vanishes and the broad magnon peak shows a rather weak quadratic increase of its frequency between 45 cm^{-1} at zero field up to ~47 cm^{-1} for $H = 2$ T. This behavior allows us to conclude that the interaction between AFM ordered Mn^{3+} spins with R^{3+} spins quickly vanishes with the temperature increase.

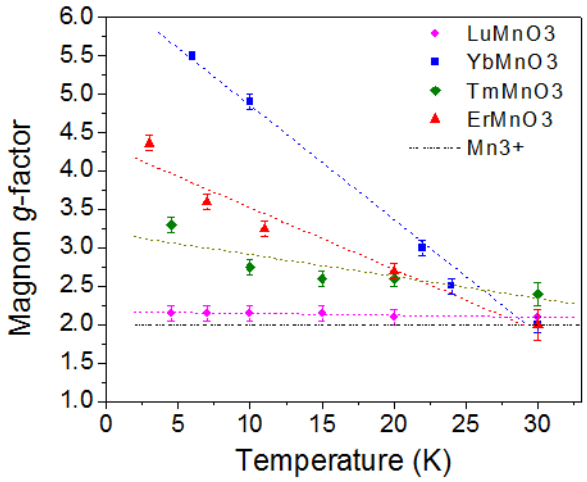

Figure 8.6 Temperature dependence of the magnon g-factor for RMnO$_3$ (R=Lu, Yb, Tm, and Er). Dashed lines guide the eye. The horizontal line corresponds to the theoretical expectation for g-factor of Mn^{3+}:$g_{Mn} = 2$. At higher temperatures above $T \approx 32 \pm 5$ K, the magnon g-factors approach $g_{Mn} = 2$ in all RMnO$_3$.

Another interesting feature that can be observed in all compounds with a non-zero spin of R^{3+} ions is a sudden increase of the magnon doublet frequencies Δ that occurs at a certain value of a critical field $H_C \approx 4$ T. This increase is shown in Figure 8.5(b) for TmMnO$_3$ and can be described as follows:

$\Omega^{\pm}{}_M(H) = \Omega_M(0) \pm \frac{1}{2} g\mu_B H$	$H > H_C \approx 4T$	(8.2)
$\Omega^{+}{}_M(H) = \Omega_M(0) + \Delta + \frac{1}{2} g'\mu_B H$ $\Omega^{-}{}_M(H) = \Omega_M(0) + \Delta - \frac{1}{2} g'\mu_B H$	$H > H_C \approx 4T$	

The high field values of g' are listed in Table 8.1 for all samples. Typical values of Δ are about 2 cm^{-1}. Taking into account the experimentally determined value for the effective magnon g-factor (see Table 8.1), Δ can be attributed to the appearance of an internal magnetic field $B_{int} = 2\Delta/(g\mu_B)$, which is about 3.5 T in TmMnO$_3$. It is also important to note that the high-field values of the effective g-factors for the magnon peaks

measured separately for $H > H_C$ are significantly lower than that determined at the low fields (see Table 8.1). The g' values for $H > H_C$ in RMnO$_3$ (R=Yb, Tm, Er) vary between 2.1 and 2.6 (much closer to $g_{Mn} = 2$), while the low-field values, which were discussed above, are significantly larger. The following section discusses this effect in more detail and will attribute it to magnetic-field induced saturation for R^{3+} magnetization for $H > H_C$.

In the previous section [see Figure 8.3], it mentions that in YbMnO$_3$, the magnon splits into several peaks at low temperatures. A closer view at this effect is presented in Figure 8.7(a,b,c). Note that this effect was not observed in other measured RMnO$_3$ samples probably due to lower values of T_R. Temperature dependence of the transmission intensity in YbMnO$_3$ measured at zero magnetic field is shown in Figure 8.7(a). At higher temperatures [left-hand side of Figure 8.7(a)] one can see a single magnon at ~53 cm^{-1}, but for $T < T_R$ =3.3K [right-hand side of Figure 8.7(a)] this magnon splits into three weaker lines. The gaps between these three lines, which increase with the temperature decrease, are marked as Δ_{13} and Δ_{23}. The maximum value of Δ_{13} is about 4 cm^{-1}, while the splitting of the upper magnon branch Δ_{23} reaches only about 2 cm^{-1} at low temperatures. A much smaller splitting of the lower magnon branch at T≈3 K is difficult to analyze due to insufficient spectral resolution. Both gaps, Δ_{13} and Δ_{23}, may be attributed to the AFM alignment of Yb^{3+} spins and the corresponding changes in the internal magnetic fields B_{13} and B_{23} that affect Mn^{3+} spins. To estimate the internal field values $B(T) = \Delta(T)/(g''\mu_B)$, one needs to know the effective magnon g-factors, which are not necessarily the same as that measured in YbMnO$_3$ at $T > T_R$.

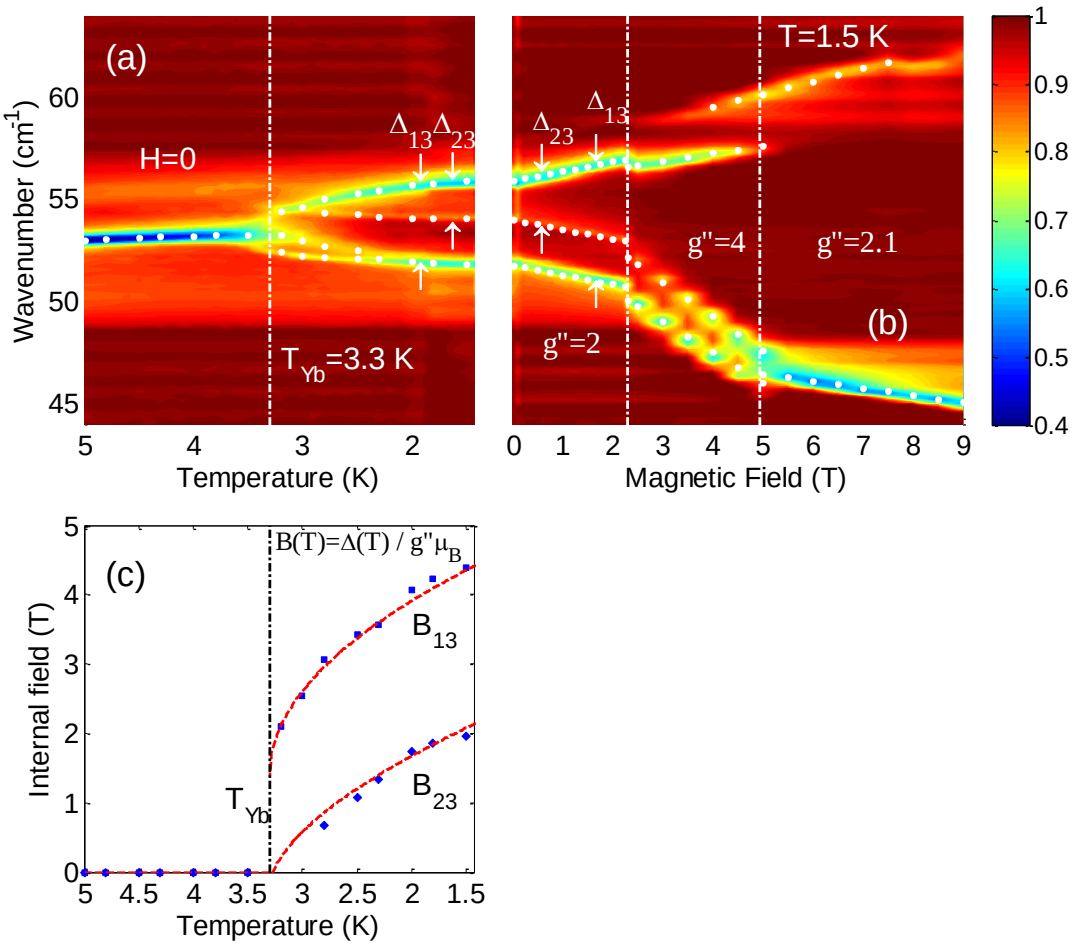

Figure 8.7 (a) Temperature dependence of the transmission intensity in $YbMnO_3$ measured at zero magnetic field. The magnon lines are marked with white dots. Below T_{Yb} = 3.3 K the major splitting of the magnon is marked with Δ_{13}. Two additional weak absorption lines can be seen with a smaller splitting Δ_{23} between top two modes. (b) Magnetic field dependence of the transmission intensity measured at T=1.45K, which corresponds to the right edge of the map in (a). The vertical frequency scale and the intensity scale are the same for the maps in (a) and (b). Below H = 2.3 T, the major magnon doublet splits in external field as $\Delta_{13}(T,H) = g''\mu_B[B_{13}(T) + H]$ with $g'' = 2$. Between H = 2.3 T and H = 5 T, the magnon g-factor is $g'' = 4$. $g'' = 2.1$ for H > 5 T. (c) Temperature dependence of the two internal fields B_{13} and B_{23}, which correspond to Δ_{13} and Δ_{23} splittings in (a) calculated as $B(T) = \Delta(T)/(g''\mu_B)$ with $g'' = 2$. Note that the reversed scale for temperature in (c) matches that in (a).

Indeed, the magnetic field measurements demonstrated that the effective magnon g-factor reduces from 5.8 to 2 for T < T_R. Figure 8.7(b) shows the magnetic field dependence of the transmission intensity measured at $T = 1.45$ K, which corresponds to the right edge of the transmission intensity map in Figure 8.7(a). At low field, all three major magnon branches experience linear shifts with H as follows: $\Delta_{13}(T,H) = g''\mu_B[B_{13}(T) + H]$ and $\Delta_{23}(T,H) = g''\mu_B[B_{23}(T) + H]$. The experimental values of $g'' = 2.0 \pm 0.1$ are the same for both gaps and coincide with g_{Mn} within the accuracy of these measurements. The estimated values for B_{13} and B_{23} are plotted in Figure 8.7(c). Their maximum values are about 4.5 T and 2 T, respectively. It is interesting to mention that the external magnetic field $H \approx B_{23}$ and $H \approx B_{13}$ results in two drastic changes in the magnon g-factor value. Figure 8.7(b) shows a sudden change in both $\Delta_{13}(H)$ and $\Delta_{13}(H)$ dependencies. Between H=2.3T and H=5T, the magnon g-factor is $g'' = 4$, while for H > 5 T the g-factor value reduces back to $g'' \approx 2.1$.

The CF peaks in Yb, Tm, and Er compounds show strong magnetic field dependencies as shown in the corresponding 2D transmission intensity maps in Figure 8.8(a, b, c). The common behavior for all three compounds reveals itself in a linear increase of the lowest CF frequencies in a magnetic field and in the change in the slopes for the magnetic field above H_C.

In Figure 8.8(a), one can see a 2D transmission intensity map for $YbMnO_3$. For $H < H_C \approx 4$ T, a linear increase of the CF transition can be described as $\Omega_{CF}(H) = \Omega_{CF}(0) + g_{Yb}\mu_B H$ with $g_{Yb} = 2.8$. Similarly to that for magnons, the CF frequency for $H > H_C$ has a jump and a reduced slope, which can be described by $\Omega_{CF}(H) = \Omega_{CF}(0) + \delta + g'_{Yb}\mu_B H$ with $g'_{Yb} \approx 2$ and $\delta \approx 5$ cm^{-1}. The single CF line in

$TmMnO_3$ seems to be unchanged for $H < H_C \approx 3.5$ T and it shifts up linearly with field for $H > H_C$.

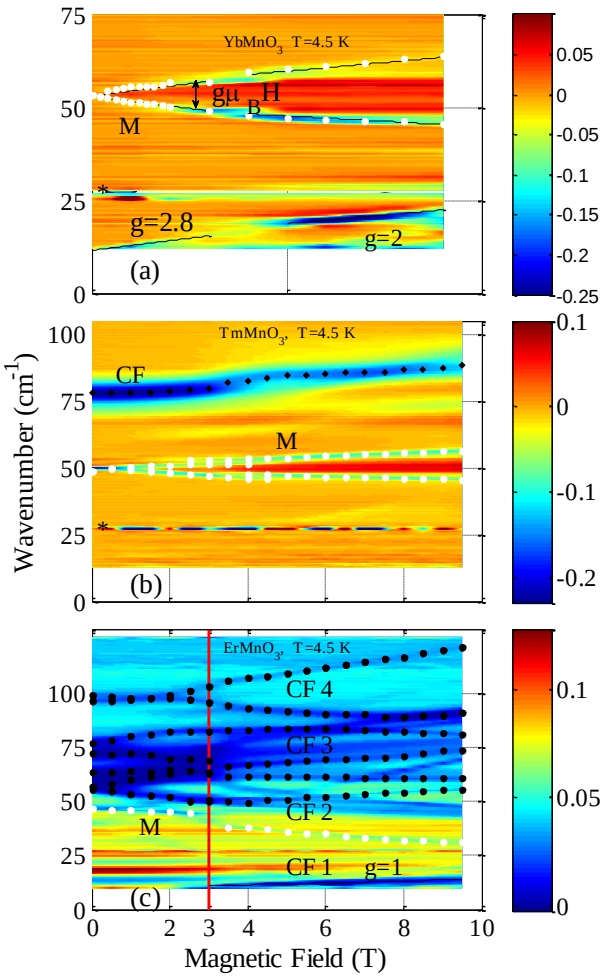

Figure 8.8 Normalized transmission maps *vs.* magnetic field and light frequency for $YbMnO_3$ in (a), $TmMnO_3$ in (b), and $ErMnO_3$ in(c) measured at $T = 4.5$ K. The blue (dark) color corresponds to stronger absorption and red (light) color indicates high transmission. The transmission intensity scale is shown with the vertical bars. The black dots represent the fit results for the CF transitions. The magnons M are shown with white circles. Note the changes of the magnon *g*-factor for $YbMnO_3$ at the critical field $H_C \approx 4$ T in (a). The critical field for $ErMnO_3$, $H_C = 2.8$ T, is marked with the vertical red line. Noise in (a) and (b) maps at ~ 27 cm^{-1}, which is marked with (*) is an artifact of the experimental setup.

The most obvious magnetic-field-induced changes in the spectra of the CF transitions have been observed in $ErMnO_3$. The 2D transmission map is shown in Figure 8.8(c). One can see a linear variation of the CF lines at low magnetic field according to their effective g-factors. The CF2 and CF 3 doublets split in magnetic field $H > H_C$ with g-factors of about $g_{Er(CF2,CF3)} = \pm 4.5$. Above a certain value of the critical field H_C, which turns out to be temperature-dependent, most of the CF lines experience either a frequency jump or a sudden strong splitting, like the CF4 doublet at 98 cm^{-1}. The higher frequency doublet C4 and the lower frequency level CF1 do not show any action at weak magnetic fields ($g_{Er(CF1,CF4)} \approx 0$). For $H > H_C$, the high frequency doublet CF4 splits with the same g-factor $g'_{Er(CF4)} = \pm 4.5$ and CF1 increases its frequency with $g'_{Er(CF1)} = 1.5$. Figure 8.9 shows an increase of H_C that varies between ~1.7 T for $T = 3.5$ K and ~8 T at $T = 35$ K. In the next section, it will be discussed that the magnetic field- and temperature-induced changes in the frequencies of magnons and CF transitions and their g-factors for several $R$$MnO_3$ compounds with and without R spins.

8.5 Theoretical Discussion

In the temperature range $T \geq 25$ K, the magnon frequency in all measured samples appears to follow the empirical trend $\Omega_M(T) - \Omega_M(0) \sim T^{\alpha}$, which is determined by the interactions between Mn spins only. The corresponding values of the magnon frequencies $\Omega_M(T = 25K)$are summarized in Table 8.1. The temperature $T = 25$ K is chosen in the following analysis for its optimum value: the Mn-R interaction is already negligibly weak and the temperature is not high enough to affect the Mn-Mn spin interaction. In this narrow temperature range, the changes of the magnon frequency with r_i may be related

to the corresponding variation of the primary antiferromagnetic exchange constant J and anisotropy D for Mn spins. The corresponding Hamiltonian can be written as follows [119]

$$\widehat{H} = J\sum_{i,j}\overrightarrow{S_i}\cdot\overrightarrow{S_j} + D\sum_{i}(S_i^z)^2 \tag{8.3}$$

where the sum is taken over nearest-neighbor in-plane spin pairs. The magnon frequency can be expressed in terms of J and D constants: $\Omega_M = 3S_{Mn}\sqrt{J\cdot D}$, where $S_{Mn} = 2$ is the spin of Mn. [116] The empirical values for the $J\cdot D$ product are shown in Table 8.1 demonstrating a systematic decrease of $J\cdot D$ with increase of r_i. As will be shown in the following, the measurement of the magnon frequency at the zone center cannot always separate the J and D constants, even if the empirical magnetic-field dependence $\Omega^{\pm}{}_M(H)$ is considered.

The Hamiltonian for Mn spin interaction in external magnetic field H directed along c-axis includes another term:

$$\widehat{H} = J\sum_{i,j}\overrightarrow{S_i}\cdot\overrightarrow{S_j} + D\sum_{i}(S_i^z)^2 - \mu H\sum_{i}S_i^z \tag{8.4}$$

Correspondingly, in the approximation of weak H, the quasi-linear splitting of the magnon branches $\Omega_M^{\pm}(H)$ can be written as follows: [116] [120] [123]

$$\Delta\Omega^{\pm}{}_M(H) = \frac{g_{Mn}J}{J + {}^{2D}/_{9}}\mu_B H = g\mu_B H \tag{8.5}$$

Note, however, that Equation 8.5 is a weak field approximation for a more general molecular field solution of the 120° spin structure. [123] Although Eq.(5) ignores nonlinear terms in the $\Omega^{\pm}{}_M(H)$ dependencies and is only valid for weak H, it turns out that the condition of a weak field can be easily satisfied in hexagonal RMnO$_3$ if $H <$

$S_{Mn}J \approx 30$ T. Such a high value of the "weak" field is due to a relatively strong exchange constant $J \approx 20$ cm^{-1} in RMnO$_3$ compared to other hexagonal materials. [119] [123] The applicability of the weak field approximation to the experimental data measured with $H \leq 9$ T has been additionally confirmed by the observation of symmetric and linear-in-field splitting of the magnon in LuMnO$_3$ shown in Figure 8.5(a). In other materials, with a similar 120° spin structure but much smaller values of J, such as CsCuCl$_3$, the "strong" field effects can be observed starting at about 5 T. [123] In such case, the exact equations for $\Omega^{\pm}{}_M(H)$, which can be found in References [116] [123], are required.

For positive J and D constants, Equation 8.5 allows only solutions with the effective magnon g-factors of $g \leq g_{Mn} = 2$. When the D/J ratio is less than 0.2, the calculated g-factor asymptotically approaches $g_{Mn} = 2$ from below and the fit for the magnon splitting becomes insensitive to the individual values of J and D. Within the accuracy of these measurements, the empirical values of the magnon g-factor are larger than 2 for $T \geq 25$K [see Figure 8.6]. Thus, one cannot measure the D/J ratio regardless of whether Equation 8.5 is used or more sophisticated equations for $\Omega^{\pm}{}_M(H)$ from Reference [123]. This experimental results can only determine the $J \cdot D$ product from the magnon frequency, which is listed in Table 8.1. Neutron scattering measurements of the magnon dispersion may help to determine J and D constants, as it has been done for HoMnO$_3$ in Reference [119] (see Table 8.1 for the experimental values of J, D, and $D/J = 0.12$). The corresponding value of the magnon g-factor calculated with Equation 8.5 would be $g = 1.95$, which is practically indistinguishable from $g_{Mn} = 2$ within the accuracy of these measurements. Another hypothetical possibility to determine $J$and D

constants in RMnO$_3$ is to measure $\Omega^{\pm}{}_M(H)$ in strong magnetic fields up to $H \approx S_{Mn}J \approx$ 30 T, when the nonlinear dependencies $\Omega^{\pm}{}_M(H)$ become sensitive to the D/J ratio.

The observed magnon frequency deviation from $\Omega_M(T) - \Omega_M(0) \sim T^{\alpha}$ with the temperature decrease below $T < 25$ K [Figure 8.2(a)] is a strong indication of the Mn-R spin interaction. The simplest way to describe the effect of R^{3+} ions is to consider an exchange interaction between Mn spins and the temperature-average spins of R^{3+}. Magnetization of R ions can be estimated as $M_R = g_R J_R \mu_B B_J(x)$, where the argument of the Brillouin function $B_J(x)$ $x = g_R \mu_B J_R B_{INT}/k_B T$ depends on the internal field B_{INT}. Figure 2(b) shows calculations for a relative change of magnetization $M_{Er}(T)/M_{Er}(0)$ for Er^{3+} using parameters $J_R = 15/2$, $g_{Er} = 1.2$. The value of internal field and $B_{INT} = 2$ T is chosen to fit the experimental data for Er^{3+} magnetization from Reference [47]. The increase of the empirical values of the magnon frequency above the level shown with the red solid line $\Omega_M(T) - \Omega_M(0) \sim T^{\alpha}$ in Figure 8.2(a) for ErMnO$_3$ correlates well with the calculated dependence for $M_{Er}(T)/M_{Er}(0)$ in Figure 8.2(b).

The decrease of the magnon g-factor for the temperature increase in the range $T < 32$ K can be also related to the PM contribution of R^{3+} ions. At about 32±5 K the g-factor values of the magnons for three RMnO$_3$ (R=Er, Tm, Yb) compounds approach $g_{Mn} = 2$. The temperature dependence of $g(T)$ cannot be related to any phase transitions at 32±5 K, but rather to the strong temperature variation of the R magnetization $M^z{}_R$, as it is shown in Figure 2(b) for Er^{3+} where $M^z{}_{Er}(T)$ is strong for $T < 32$ K and quickly disappears above ~32 K: $M^z{}_{Er}(T) \ll M_{Mn}(T)$. The accuracy of the measurements does not allow for the determination of the exact functional relationship between $g(T)$ and $M^z{}_R(T)$. Thus used is the simplest linear approximation

for $g(T)$ shown with dashed lines that guide the eye in Figure 8.6. To help with qualitative understanding of the connection between $g(T)$ and $M^z{}_{Er}(T)$ it can be assumed that a ferromagnetic coupling between Mn and R spins exists. Then the magnetization component $M^z{}_R$ along the external magnetic field $(H \parallel c)$ is equivalent to an additional magnetic field $B_R \sim M^z{}_R(H,T) \sim H$ that influences the Mn spins and results in an increase of the effective magnon g-factor above 2: $[g(T) - g_{Mn}] \sim M^z{}_R(H,T)$ [see Figure 8.6]. In the weak magnetic fields and $T < 32$ K, $M^z{}_R(H,T) \sim H/T$, while above 32 K, $M^z{}_R(H,T)$ approaches zero.

In all hexagonal compounds, it was found that above a critical external field H_C, which is between 2.5 T and 4 T for different compounds at $T \approx 5$ K, the effective g-factor decreases suddenly to approximately 2. This effect can be qualitatively understood taking into consideration two R sublattices: below H_C two sublattices of R which are AFM-coupled to each other, but above H_C there is a complete reorientation of the R spins along the magnetic field. In this case, the AFM interaction between R spins changes to FM and the paramagnetic $M^z{}_R(H)$ reaches saturation and cannot contribute to the effective magnon g-factor, which becomes $g \approx g_{Mn}$.

Figure 8.9 shows the critical external field H_C as a function of temperature for $ErMnO_3$. At low temperatures, H_C increases linearly with T: $3\mu_B H_C \approx k_B T$. This behavior corresponds to the formal requirement to keep the PM magnetization constant $M^z{}_R(H,T) \sim H/T \approx Const$. At low external fields, the crystal field that includes the Mn-R interaction dominates over the external perturbation. Two CF levels, CF1 and CF4 have zero g-factors along c-axis, while g-factors of CF2 and CF3 doublets are

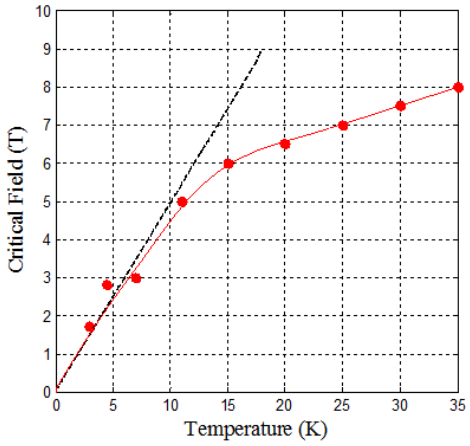

Figure 8.9 Temperature dependence of the critical external magnetic field H_C in $ErMnO_3$. Experimental points were determined from the 2D transmission intensity maps measured at different temperatures [similar to that is shown in Figure 8(c)]. Straight dotted line corresponds to $g_{Er}\mu_B H_C = k_B T$ calculated with $g_{Er} = 3$. Red curve guides the eye.

$g_{Er(CF2,CF3)} = \pm 4.5$. At high external fields, Er^{3+} ions re-orient their magnetization along the c-axis that is reflected in the sudden change of $g_{Er(CF4)}$ from zero to ± 4.5.

PM to AFM transition for Yb^{3+} can explain the magnon behavior in $YbMnO_3$ for $T < 3.3$ K shown in Figure 8.7(a,b). The PM contribution to the effective magnon g-factor $(g - g_{Mn}) \approx 3.8 \pm 0.6$ suddenly decreases due to the transition between the PM and AFM ordering of Yb spins, $M^z{}_{Yb}$ reaches saturation for $T < 3.3$ K, and the magnon g-factor becomes $g \approx g_{Mn}$. In the high field $H > 5$ T, the complete saturation of the R sublattice is achieved along the c-axis and $g(H > 5\,T) \approx g_{Mn}$. To find the exact magnetic structure for $\{T < 3.3\,K, 2.3\,T < H < 5\,T\}$ and to explain why the effective magnon g-factor is equal to 4 in this range, one needs to perform precise theoretical calculations for the interaction between the Mn and Yb spin sublattices. The transmission data for $YbMnO_3$ suggest that an interesting $T - H$ diagram can exist with several low-temperature phases. Figure 7(a,b) shows just two cross sections of this diagram: the PM

to AFM border line at about $T_{Yb} = 3.3$ K and two critical fields: $H_{C1} = 2.3$ T and $H_{C2} = 5$ T. It suggests that these two critical fields correspond to consecutive orientation of Yb^{3+} spins along the magnetic field. Two values of H_{C1} and H_{C2} probably correspond to two non-equivalent Yb^{3+} spin sublattices. It is very probable that T_{Yb} depends on external magnetic field, while H_{C1} and H_{C2} are functions of temperature. Note, however, that measurements of a complete $T - H$ diagram using far-IR optical transmission would require a significant amount of additional efforts. Behind each point on such diagram should be a spectrum, not a single parameter, as in, for example, magnetization measurements.

8.6 Conclusions

The experimental results for the magnon and CF transmission spectra in several single crystal *R*MnO_3 hexagonal manganites has been presented. The observed magnon frequencies increase systematically with the famous decrease of the *R* ionic radius r_i between Ho and Lu. The measured magnon frequencies allow to determine the product of $J \cdot D$, but do not permit their separation due to the condition $J \gg D$ and high internal exchange fields between Mn spins. At low temperatures below ~30 K the Mn-*R* interaction changes both the magnon *g*-factors and the magnon frequencies. Both trends are explained qualitatively by the changes of *R* magnetization with temperature and magnetic field, where : $M_{RE}^{z}(H,T) \sim H/T$. In $YbMnO_3$, it was observed that the AFM ordering of Yb spins below $T_{RE} = 3.3$ K. In other compounds ($TmMnO_3$ and $ErMnO_3$), this effect was not seen probably due to even lower ordering temperatures for *R* spins. The parameters of the magnon and CF spectra can be useful for precise theoretical

models for *R*-Mn interaction in hexagonal manganites and for better understanding of the interplay between the AFM and FE effects in these compounds.

CHAPTER 9

SUMMARY

After a review of background materials in Chapters 1-5, the following defendable statements were shown in Chapters 6-8.

- Pairs of rotatable retarders which are not commercially available have been manufactured and tested for a far-IR spectroscopic ellipsometer.

- Using materials, such as silicon and KRS5, with multiple bounce designs a broadband range of approximately 20 to 4000 cm^{-1} can be covered for full-Mueller matrix ellipsometric experiments.

- In $Tb_3Fe_5O_{12}$, a strong hybridization occurred between magnon and LF transitions. The magnon in $Tb_3Fe_5O_{12}$ is confined between two LF transitions: it couples to the higher energy one at low temperatures and weak fields while it comes to resonance with low-energy transition at higher temperatures ~60 K.

- It was estimated that the ratio of Fe-Dy and Dy-Dy exchange constants to be 0.13.

Based on the experimental results for the magnon and crystal field transmission spectra in several single crystal Rare Earth hexagonal manganites $R\mathrm{MnO_3}$ (R= Er, Tm, Yb, Lu) the following is summarized.

- In $R\mathrm{MnO_3}$, the observed magnon frequencies increase systematically with the decrease of the Rare Earth ionic radius from Ho to Lu.

- At low temperature, the Mn-R exchange interaction changes causes both the magnon g-factors and the magnon frequencies to increase. Both trends have been explained qualitatively by the changes of rare earth magnetization with temperature and magnetic field, where : $M_{RE}^{z}(H,T) \sim H/T$.

- The measured magnon frequencies allow to determine the product of $J \cdot D$, but do not permit their separation due to the condition $J \gg D$ and high internal exchange fields between Mn spins. The parameters of the magnon and CF spectra have been tabulated in the text.

- In $YbMnO_3$, it was observed the AFM ordering of Yb spins below $T_{RE} = 3.3$ K.

As NSLS I is closing in the upcoming year, the ellipsometer project will need to be moved to NSLS II. The move will require some changes since NSLS II will have a only one ring which is designed to produce x-rays 10,000 times brighter than NSLS I. The development of a new user friendly computer interface for Mueller matrix analysis would be beneficial. This program should have the ability to view all 16 matrix elements and fit any resonances seen. The next step in the research of $RMnO_3$ would be to take a closer look at the phonons in these materials. .

REFERENCES

[1] D. J. Griffiths, *Introduction to Electrodynamics 3rd Ed*. (Prentice Hall, Upper Saddle River, NJ, 1999).

[2] J. D. Jackson, *Classical Electrodynamics, 3rd Ed.* (Wiley, Hoboken, NJ, 1999).

[3] G. R. Fowles, *Introduction to Modern Optics (*Dover, Mineola, NY, 1975).

[4] V. G. Veselago, Sov. Phys. Usp. **10**, 509 (1968).

[5] H. Fujiwara, *Spectroscopic Ellipsometry: Principles and Applications* (Wiley, Tokyo, Japan, 2007).

[6] L. Landau and E. M. Lifshitz, *Electrodynamics of Continuous Media* (Pergamon, Oxford, England, 1960).

[7] I.E. Dzyaloshinskii, Sov. Phys. JETP **10**, 628 (1959).

[8] D.W. Berreman, J. Opt. Soc. Am. **62**, 502 (1972).

[9] W. Eerenstein, N.D. Mathur, J.F. Scott, Nature **442**, 759(2006).

[10] W. Swindell (ed.), *Polarized Light* (Dowden, Hutchinson & Ross Inc., Stroudsburg, PA, 1975).

[11] T. Yoshizawa (ed.), *Handbook of Optical Metrology: Principles and Applications* (CRC Press, Boca Raton, FL, 2009)

[12] "Fresnel Rhomb Retarders," [Online]. Available: http://www.thorlabs.com/NewGroupPage9.cfm?ObjectGroup_ID=154. [Accessed 8 12 2012].

[13] T. Stanislavchuk, T. Kang, E. C. Rodgers, R. Basistyy, A. M. Kotelyanskii, G. Nita, T. Zhou, G. L. Carr, M. Kotelyanskii and A. A. Sirenko, Rev. Sci. Instr. **84**, 023901 (2013).

[14] G. L. Carr, P. Dumas, C. J. Hirschmugl and G. P. Williams, Il Nuovo Cimento **20 D**, 4 (1998).

[15] J. Kircher, R. Henn, M. Cardona, P. L. Richards and G. P. Williams, J. Opt. Soc. Am. B **14**, 705 (1997).

[16] C. Bernhard, R. Henn, A. Wittlin, M. Klaser, G. Muller-Vogt, C. T. Lin and M. Cardona, Phys. Rev. Lett **80**, 1762 (1998).

[17] A. A. Sirenko, C. Bernhard, A. Golnik, A. M. Clark, J. Hao, W. Si and X. X. Xi, Nature (London) **404**, 6776 (2000).

[18] C. Bernhard, D. Munzar, A. Wittlin, W. Konig, A. Golnik, C. T. Lin, M. Klasser, T. Wolf, G. Muller-Vogr and M. Cardona, Phys. Rev. B **59**, 10 (1999).

[19] C. Bernhard, T. Holden, J. Humlick, D. Munzar, M. Cardona and B. Keimer, Solid State Commun. **121**, 93 (2002).

[20] C. J. Hirschmugl and G. P. Williams, Sychrotron Radiat. News **8**, 10 (1995).

[21] J. Kircher, R. Henn, M. Cardona, P. L. Richards and G. P. Williams, J. Opt. Soc. Am. B **14**, 705 (1997).

[22] N.A. Spaldin, S.-W. Cheong, R. Ramesh, Physics Today **63**, 38 (2010).

[23] F. Sayetat, J. of Mag. and Mag. Mat. **58**, 334 (1986).

[24] F. Sayetat, J. X. Boucherle, and F. Tcheou, J. Magn. Magn. Mater. **46**, 219 (1984).

[25] R. Hock, H. Fuess, T. Vogt, and M. Bonnet, J. of Solid State Chem. **84**, 39 (1990).

[26] F. Sayetat, J. of Mag. and Mag. Mat. **58**, 334 (1986).

[27] P. Rogers, Y. J. Choi, E. C. Standard, T. D. Kang, K. H. Ahn, A. Dubroka, P. Marsik, C. Wang, C. Berhard, S. Park, S. W. Cheong and A. A. Sirenko, Phys. Rev. B **83**, 174407 (2011).

[28] N. Hur, S. Park, S. Guha, A. Borissov, V. Kiryukhin and S.-W. Cheong, Appl. Phys. Lett **87**, 042901 (2005).

[29] M. Lahoubi, W. Younsi, M. L. Soltani, J. Voiron, and D. Schmitt, J. Phys.: Conf. Ser. **150**, 042108 (2009).

[30] M. Lahoubi, W. Younsi, M.-L. Soltani, and B. Ouladdiaf, J. Phys.: Conf. Ser. **200**, 082018 (2010).

[31] D. Talbayev, A. D. LaForge, S. A. Trugman, N. Hur, A. J. Taylor, R. D. Averitt and D. N. Basov, Phys. Rev. Lett. **101**, 247601 (2008).

[32] S. C. Abrahams, Acta. Crystallogr. Sect. B **57**, 485 (2001).

[33] V. Goiana, S. Kamba, C. Kadleca, D. Nuzhnyya, P. Kuzela, J. Agostinho Moreirab, A. Almeidab and P. B. Tavares, Phase Transitions **83**, 931 (2010).

[34] M. N. Iliev, H. -G. Lee, V. N. Popov, M. V. Abrashev, A. Hamed, R. L. Meng and C. W. Chu, Phys. Rev. B **56**, (1997).

[35] B. B. V. Aken, T. T. M. Palstra, A. Flippetti and N. A. Spaldin, Nat. Mater. **3**, 164 (2004).

[36] J. -S. Zhou, J. B. Goodenough, J. M. Gallardo-Amores, E. Moran, M. A. Alario-Franco and R. Caudillo, Phys. Rev. B **56**, 2623 (1997).

[37] I. Munawar and S. H. Curnoe, J. Phys.: Condens. Matter **18**, 9575 (2006).

[38] E. F. Bertaut and M. Mercier, Phys. Lett. **5**, 27 (1963).

[39] P. A. Sharma, J. S. Ahn, N. Hur, S. Park, S. Baek Kim, S. Lee, J.-G. Park, S. Guha and S.-W. Cheong, Phys. Rev. Lett., **93**, 177202 (2004).

[40] S. G. Condran and M. L. Plumer, J. Phys.: Condens. Matter **22**, 162201 (2010).

[41] B. G. Ueland, J. W. Lynn, M. Laver, Y. J. Choi and S.-W. Cheong, Phys. Rev. Lett. **104**, 147204 (2010).

[42] B. Lorenz, F. Yen, M. M. Gospodinov and C. W. Chu, Phys. Rev. B **71**, 014438 (2005).

[43] A. Munoz, J. A. Alonso, M. J. Martinez-Lope, M. T. Casais, J. L. Martinez and M. T. Fernandez-Diaz, Chem. Mater. **13**, 1497 (2001).

[44] T. Lonkai, D. Hohlwein, J. Ihringer and W. Prandl, Appl. Phys. A **74**, S843 (2002).

[45] M. Fiebig, D. Frohlich, K. Kohn, S. Leute, T. Lottermoser, V. V. Pavlov and R. V. Pisarev, Phys. Rev. Lett. **84**, 5620 (2000).

[46] M. Fiebig, D. Frohlich, T. Lottermoser and K. Kohn, Appl. Phys. Lett. **77**, 4401 (2000).

[47] M. Fiebig, C. Degenhardt and R. V. Pisarev, J. Appl. Phys. **91**, 8867 (2002).

[48] M. Friebig, D. Frohlich, T. Lottermoser and M. Maat, Phys. Rev. B **66**, 144102 (2002).

[49] X. Fabreges, I. Mirebeau, P. Bonville, S. Petit, G. Lebras-Jasmin, A. Forget, G. Andre and S. Pailhes, Phys. Rev. B **78**, 214422 (2008).

[50] H. A. Salama and G. A. Stewart, J. Phys. Condens. Matter **21**, 386001 (2009).

[51] Y. Geng, N. Lee, Y. J. Choi, S.-W. Cheong and W. Wu Nano Lett. **12**, 6055 (2012).

[52] I. E. Dzyaloshinskii, Sov. Phys. JETP **10**, 628 (1960).

[53] T. Moriya, Phys. Rev. **120**, 91 (1960).

[54] A. D. Martino, E. Carcia-Caurel, B. Laude and B. Drevillon, Thin Solid Films **455-456**, 112 (2004).

[55] R. M. A. Azzam and N. M. Bashara, *Ellipsometry and Polarized Light* (Elsevier Science, New York, NY, 1987).

[56] M. Born and E. Wolf, Principles of Optics 7th Ed. (Cambridge University Press, Oxford, England, 1999..

[57] J. D. Boer, *Spectroscopic Infrared Ellipsometry: Components, Calibration, and Application* (Eindhoven University of Technology, Eindhoven, Netherlands, 1995).

[58] N. N. Nagib and S. A. Khodier, Applied Optics **34**, 2927 (1995).

[59] R. H. Muller, Surf. Sci. **16**, 14 (1969).

[60] P. S. Hauge, J. Opt. Soc. Am. **68**, 1519 (1978).

[61] H. G. Tompkins, and E. A. Irene, *Handbook of Ellipsometry*, (William Andrew Publishing, Inc., Norwich, NY, 2005).

[62] R. M. A. Azzam, J. Opt. Soc. Am. A **17**, 2105 (2000).

[63] M. Luttemann, J.-L. Stehle, C. Defranoux, and J.-P. Piel, Thin Solid Films **313-314**, 631 (1998).

[64] K. P. Belov and V. I. Sokolov, Usp. Fiz. Nauk **121**, 285 (1977) [Sov. Phys. Usp. **20**, 149 (1977)].

[65] D. Louca, K. Kamazawa, and T. Proffen, Phys. Rev. B **80**, 214406 (2009).

[66] T. D. Kang, E. Standard, K. H. Ahn, and A. A. Sirenko, G. L. Carr, S. Park, Y. J. Choi, M. Ramazanoglu, V. Kiryukhin, and S-W. Cheong, Phys. Rev. B **82**, 014414 (2010).

[67] N. Hur, S. Park, P. A. Sharma, J. S. Ahn, S. Guha, and S.-W. Cheong, Nature (London) **429**, 392 (2004).

[68] T. Kimura, T. Goto, H. Shintani, K. Ishizaka, T. Arima, and T. Tokura, Nature (London) **426**, 55 (2003).

[69] S.-W. Cheong and M. Mostovoy, Nature Mater. **6**, 13 (2007).

[70] B. Lorenz, A. P. Litvinchuk, M. M. Gospodinov, and C. W. Chu, Phys. Rev. Lett. **92**, 087204 (2004).

[71] T. Lottermoser and M. Fiebig, Phys. Rev. B **70**, 220407(R) (2004).

[72] A. Pimenov, A. A. Mukhin, V. Yu. Ivanov, V. D. Travkin, A. M. Balbashov, and A. Loidl, Nat. Phys. **2**, 97 (2006).

[73] D. J. Lockwood and M. G. Cottam, J. Appl. Phys. **64**, 5876 (1988).

[74] K. Wakamura and T. Arai, J. Appl. Phys. **63**, 5824 (1988).

[75] A. B. Sushkov, O. Tchernyshyov, W. Ratcliff II, S. W. Cheong, and H. D. Drew, Phys. Rev. Lett. **94**, 137202 (2005).

[76] A. B. Sushkov, R. V. Aguilar, S. Park, S.-W. Cheong, and H. D. Drew, Phys. Rev. Lett. **98**, 027202 (2007).

[77] T. Rudolf, Ch. Kant, F. Mayr, and A. Loidl, Phys. Rev. B **77**, 024421 (2008).

[78] Ch. Kant, T. Rudolf, F. Schrettle, F. Mayr, J. Deisenhofer, P. Lunkenheimer, M. V. Eremin, and A. Loidl, Phys. Rev. B **78**, 245103 (2008).

[79] R. Schleck, R. L. Moreira, H. Sakata, and R. P. S. M. Lobo, Phys. Rev. B **82**, 144309 (2010).

[80] R. Schleck, Y. Nahas, R. P. S. M. Lobo, J. Varignon, M. B. Lepetit, C. S. Nelson, and R. L. Moreira , Phys. Rev. B **82**, 054412 (2010).

[81] J. Kaplan and C. Kittel, J. Chem. Phys. **21**, 760 (1953).

[82] R. V. Aguilar1, M. Mostovoy, A. B. Sushkov, C. L. Zhang, Y. J. Choi, S-W. Cheong, and H. D. Drew, Phys. Rev Lett. **102**, 047203 (2009).

[83] Y. Takahashi, N. Kida, Y. Yamasaki, J. Fujioka, T. Arima, R. Shimano, S. Miyahara, M. Mochizuki, N. Furukawa and Y. Tokura, Phys. Rev. Lett **101**, 187201 (2008).

[84] A. A. Sirenko, S. M. O'Malley, K. H. Ahn, S. Park, G. L. Carr and S. -W. Cheong, Phys. Rev. B **78**, 174405 (2008).

[85] C. Bernhard, J. Humlíček , and B. Keimer, Thin Solid Films **455 – 456**, 143 (2004).

[86] A. J. Sievers and M. Tinkham, Phys. Rev. **129**, 1995–2004 (1963).

[87] M. Tinkham, Phys. Rev. **124**, 311 (1961).

[88] J. Yamamoto, B. T. Smith, and E. E. Bell, J. Opt. Soc. Am. **64**, 880 (1974).

[89] G. H. Dieke, *Spectra and Energy Levels of Rare Earth Ions in Crystals* (Wiley, New York, NY, 1968).

[90] P. Grunberg, S. Hufner, E. Orlich, and J. Schmitt, Phys. Rev. **184**, 285 (1969).

[91] F. Sayetat, J. of Magn. and Magn. Mat. **58**, 334 (1986).

[92] N. T. McDevit, J. Opt. Soc. Am. **57**, 834, (1967).

[93] R. M. A. Azzam, K. A. Giardina and A. G. Lopez, Opt. Eng. **30**, 1583 (1991).

[94] M. G. Cottam and D. J. Lockwood, *Light Scattering in Magnetic Solids* (Wiley, New York, NY, 1986)

[95] I. Veltrusky and V. Nekvasil, J. Phys. C **13**, 1685 (1980).

[96] J. F. Dillon, Phys. Rev. **105**, 759 (1957).

[97] P. Grunberg and J. A. Koningsten, J. Opt. Soc. Am. **61**, 1613 (1971).

[98] N. T. McDevitt, J. Opt. Soc. Am. **59**, 1240 (1969).

[99] P. D. Rogers, T. D. Kang, T. Zhou, M. Kotelyanskii, and A. A. Sirenko, Thin Solid Films **519**, 2668 (2011).

[100] J. Ménéndez and M. Cardona , Phys. Rev. B **29**, 2051 (1984).

[101] J. A. Alonso, M. J. Martinez-Lope, M. T. Casais, and M. T. Fernandez-Diaz, Inorg. Chem. **39**, 917 (2000).

[102] Z. J. Huang, Y. Cao, Y. Y. Sun, Y. Y. Xue, and C. W. Chu, Phys. Rev. B **56**, 2623 (1997).

[103] J. C. Lemyre, M. Poirier, L. Pinsard-Gaudart, and A. Revcolevschi, Phys. Rev. B **79**, 094423 (2009).

[104] T. Goto, T. Kimura, G. Lawes, A. P. Ramirez, and Y. Tokura, Phys. Rev. Lett. **92**, 257201 (2004).

[105] S. Petit, F. Moussa, M. Hennion, S. Pailhès, L. Pinsard-Gaudart, and A. Ivanov, Phys. Rev. Lett. **99**, 266604 (2007).

[106] H. Katsura, N. Nagaosa, A. V. Balatsky, Phys. Rev. Lett. **95**, 057205 (2005).

[107] I. A. Sergienko and E. Dagotto, Phys. Rev. B **73**, 094434 (2006).

[108] M. Mostovoy, Phys. Rev. Lett. **96**, 067601 (2006).

[109] S.-W. Cheong and M. Mostovoy, Nature Materials **6**, 13 (2007).

[110] Y. Tokura, , J. Mag. Mag. Mat. **310**, 1145 (2007).

[111] A. Pimenov, A.A. Mukhin, V.Yu. Ivanov, V.D. Travkin, A.M. Balbashov, and A. Loidl, Nature Physics **2**, 97 (2006).

[112] A. Pimenov, A. M. Shuvaev, A. A. Mukhin, A. Loidl, J. Phys.: Condens.Matter **20**, 434209 (2008).

[113] D. Senff, N. Aliouane, D. N. Argyriou, A. Hiess, L. P. Regnault, P. Link, K. Hradil, Y. Sidis, M. Braden, J. Phys.: Condens. Matter **20**, 434212 (2008).

[114] N. Kida, Y. Takahashi, J. S. Lee, R. Shimano, Y. Yamasaki, Y. Kaneko, S. Miyahara, N. Furukawa, T. Arima, Y. Tokura, J. Opt. Soc. Am. B **26**, A35 (2009).

[115] A. Pimenov, A. Shuvaev, A. Loidl, F. Schrettle, A. A. Mukhin, V. D. Travkin, V. Yu. Ivanov, and A. M. Balbashov, Phys. Rev. Let. **102**, 107203 (2009).

[116] A. M. Shuvaev, V. D. Travkin, V. Yu. Ivanov, A.A. Mukhin, and A. Pimenov, , Phys. Rev. Lett. **104**, 097202 (2010).

[117] C. Kadlec, V. Goian, K. Z. Rushchanskii, P. Kuzel, M. Lezaic, K. Kohn, R. V. Pisarev, and S. Kamba, Phys. Rev. B **84**, 174120 (2011).

[118] D. Talbayev, A. D. LaForge, S. A. Trugman, N. Hur, A. J. Taylor, R. D. Averitt, D. N. Basov, Phys. Rev. Lett. **101**, 247601 (2008).

[119] T. Chatterji, S. Ghosh, A. Singh, L.P. Regnault, and M. Rheinstadter, Phys. Rev. B, **76,** 144406 (2007).

[120] T. J. Sato, S.-H. Lee, T. Katsufuji, M. Masaki, S. Park, J.R.D. Copley, and H. Takagi, Phys. Rev. B **68,** 014432 (2003).

[121] O. P. Vajk, M. Kenzelmann, J.W. Lynn, S. B. Kim, and S.-W. Cheong, Phys. Rev. Lett. **94**, 087601 (2005).

[122] T Penney, P. Berger, and K. Kritiyakirana, J. Appl. Phys. **40**, 1234 (1969).

[123] S. Pailhes, X. Fabreges, L.P. Regnault, L. Pinsard-Godart, I. Mirebeau, F. Moussa, M. Hennion, and S. Petit, Phys. Rev. B **79**, 134409 (2009).

[124] P. D. Rogers, Y. J. Choi, E. C. Standard, T. D. Kang, K. H. Ahn, A. Dubroka, P. Marsik, C. Wang, C. Bernhard, S. Park, S-W. Cheong, M. Kotelyanskii, and A. A. Sirenko, Phys. Rev. B **83**, 174407 (2011).

[125] W. Palme, F. Mertens, O. Born, B. Luthi, and U. Schotte, Solid State Commun. **76**, 873 (1990).

[126] "Poincare Sphere," [Online]. Available: http://en.wikipedia.org/wiki/File:Poincare_sphere.png. [Accessed 8 12 2012].

[127] M. Lahoubi, M. Guillot, A. Marchand, F. Tcheou and E. Roudaut,, IEEE Trans. Magn. **20**, 1518 (1984).

[128] S. Blundell, *Magnetism in Condensed Matter*, (Oxford University Press, Oxford, England, 2011).

[129] "Magentic Resonance," [Online]. Available: http://www.larsenglish.com/magneticresonance. [Accessed 13 12 2012].